

This electronic thesis or dissertation has been downloaded from the King's Research Portal at <https://kclpure.kcl.ac.uk/portal/>



Multiscale modelling of metallic nanoparticles structural and catalytic properties

Rossi, Kevin

Awarding institution:
King's College London

The copyright of this thesis rests with the author and no quotation from it or information derived from it may be published without proper acknowledgement.

END USER LICENCE AGREEMENT



Unless another licence is stated on the immediately following page this work is licensed

under a Creative Commons Attribution-NonCommercial-NoDerivatives 4.0 International

licence. <https://creativecommons.org/licenses/by-nc-nd/4.0/>

You are free to copy, distribute and transmit the work

Under the following conditions:

- Attribution: You must attribute the work in the manner specified by the author (but not in any way that suggests that they endorse you or your use of the work).
- Non Commercial: You may not use this work for commercial purposes.
- No Derivative Works - You may not alter, transform, or build upon this work.

Any of these conditions can be waived if you receive permission from the author. Your fair dealings and other rights are in no way affected by the above.

Take down policy

If you believe that this document breaches copyright please contact librarypure@kcl.ac.uk providing details, and we will remove access to the work immediately and investigate your claim.

Multiscale modelling of metallic nanoparticles structural and catalytic properties



Kevin Rossi

Department of Physics
King's College London

This dissertation is submitted for the degree of
Doctor of Philosophy

King's College

October 2019

*La lutte elle-même vers les sommets suffit à remplir un cœur d'homme;
il faut imaginer Sisyphe heureux - Albert Camus*

*Anche la lotta verso la cima basta a riempire il cuore di un uomo;
Bisogna immaginare Sisifo felice. - Albert Camus*

*The fight itself towards the summits suffices to fill a heart of man;
it is necessary to imagine Sisyphus happy. - Albert Camus*

Declaration

This thesis describes work carried out between September 2014 and September 2018 at the Physics Department of King's College London, under the supervision of Dr. Francesca Baletto.

During the course of my PhD I have contributed to the following publications:

- Universal signature in the melting of metallic nanoparticles - K. Rossi, R. Pinto-Miles, F. Baletto - in preparation
- Nanogenomics suggests structural diversity to enhance ORR - G.G. Asara, K. Rossi, F. Baletto - in preparation
- A genomic characterization of metallic nanoparticles - K. Rossi, G.G. Asara, F. Baletto - Physical Chemistry Chemical Physics 21 (9), 4888-4898, 2019
- Building machine learning force fields for nanoclusters - C. Zeni, K. Rossi, A. Glielmo, Á. Fekete, N. Gaston, F. Baletto, A. De Vita, The Journal of Chemical Physics 148 (24), 241739, 2, 2018
- The effect of size and composition on structural transitions in monometallic nanoparticles - K. Rossi, L. Pavan, Y.Y. Soon, F. Baletto, The European Physical Journal B 91 (2), 33, 3, 2018
- Thermodynamics of CuPt nanoalloys - K. Rossi, L. Bartok-Pártay, G. Csanyi, F. Baletto, Scientific reports 8, 2018
- Melting of large Pt@ MgO (1 0 0) icosahedra - K. Rossi, T. Ellaby, L.O. Paz-Borbón, I. Atanasov, L. Pavan, F. Baletto, Journal of Physics: Condensed Matter 29 (14), 145402, 10, 2017

- The effect of chemical ordering and lattice mismatch on structural transitions in phase segregating nanoalloys - K. Rossi, F. Baletto, *Physical Chemistry Chemical Physics* 19 (18), 11057-11063, 5, 2017 - Themed collections: 2017 PCCP HOT articles
- Controlling Structural Transitions in AuAg Nanoparticles through Precise Compositional Design - A.L. Gould, K. Rossi, C.R.A. Catlow, F. Baletto, A.J. Logsdail, *The Journal of Physical Chemistry Letters* 7 (21), 4414-4419, 7, 2016
- Metallic nanoparticles meet metadynamics - L. Pavan, K. Rossi, F. Baletto, *The Journal of Chemical Physics* 143 (18), 184304, 10 2015

I hereby declare that, except where specific reference is made to the work of others, the contents of this dissertation are original and have not been submitted in whole or in part for consideration for any other degree or qualification in this, or any other university. This dissertation is my own work and contains nothing which is the outcome of work done in collaboration with others, except as specified in the text.

Kevin Rossi
October 2019

Acknowledgements

To the ones that made my London journey rich and intense.

To my mentors and collaborators - Dr. Nicola Gaston, Dr. Oliver Paz-Borbon, Dr. Luca Pavan, Dr. Andy Logsdail, Dr. Livia Bartok-Partay, Prof. Carla Molteni, Prof. Alessandro De Vita - your actions and teachings have been of great inspiration. And in particular, to my supervisor, Dr. Francesca Baletto - your time, patience, and guidance have been of unique worth in my personal and professional development.

To my family, your support and understanding is all one could have asked for.

To my friends - Andrea, Valeria, Gian Giacomo, Pier Paolo, Giacomo, Francesco, Claudio - your company and time has been a gift. And in particular to, my flatmates - Giuseppe, Michele, Riccardo, Sara, Francesca, Laura, Pier Maria, Aldo, Karim - you have been a blessed and joyful shelter.

To Alessia, you give meaning to my days.

Abstract

Nanoparticles are characterized by their small and finite-size. Indeed they are made of tens to thousands of atoms, corresponding to a size of 1 to tens nanometers. Nanoparticles' finite-size entails three significant implications: internal transitional symmetry breaking occurs, electronic confinement effects are relevant, and nanoparticle's surface to volume ratio is not negligible. In turn, at the nanoscale, we witness: the occurrence of many peculiar structures, the arising of unique optical, magnetic, and catalytic properties (different from the one of the single atom and of its bulk counterpart) and characterized by peculiar structure-property relationships, the failure of bulk thermodynamics modeling in the prediction of the nanoparticle structural stability, also for the case of relatively large systems. Indeed size- and shape-effects are known to non-trivially affect the (meta)stability of a nanoparticle against melting and pre-melting.

Borrowing the words spelt by Richard Feynman during his famous talk 'There is plenty of Room at the bottom': *"When we get to the very, very small world ... we have a lot of new things that would happen that represent completely new opportunities for design."*[1] Tailoring the nanoparticles architecture - i.e. size, shape, chemical composition and ordering - at will, one could harness their full potential in technological devices which will trigger a revolution in many fields, ranging from biomedicine to catalysis and optics. The identification of optimal nanoparticle architectures for target purposes is, from here on, mentioned under the name of rational design. The complexity inherent to this practice represents a long-standing high-reward challenge as it hinges on the understanding of how each structural feature contributes towards the nanoparticle global chemophysical property.

Moreover, the rational design of nanoparticles for target application should encompass the in depth study of the (meta)stability of the chosen bespoke nanoarchitecture. Indeed, coming back again to Feynman's notorious contribution to nanoscience, he mentioned that *"... [he was] not afraid to consider the final question as to whether, ultimately – in the great future – we can arrange the atoms the way we want; the very atoms, all the way down! ... (within reason, of course; you can't put them so that they are chemically unstable, for example)"*. A degree of atomistic control of the nanoparticle components is currently at reach during both colloidal and physical growth methods. Thus, it is of fundamental importance

to assess whether the so synthesized nanoparticles present a satisfactory structural stability, or if their inherent (meta)stability manifests and determines too dramatic changes in the nanoparticles chemophysical properties, and thus in the performance of the device which exploits them.

This thesis will contain a discussion of the application of state-of-the-art sampling techniques to probe the complexity of the conformational and energetic landscape of noble and quasi-noble metal nanoparticles of 100-1000 atoms. Conversely, a thorough characterization of the mechanisms driving melting and pre-melting will be sought and rationalized in terms of size, shape, and composition effects. As a final case study, the structural properties of Pt nanoparticles will be carefully assessed to predict their performance for Oxygen reduction reaction, identifying design criteria towards the synthesis of nanoarchitectures with enhanced catalytic properties.

Chapter I will introduce the state-of-the-art of metallic nanoparticles characterization, synthesis, theoretical modelling, and application as nanocatalyst. Chapter II will present the numerical techniques employed to study the melting and pre-melting of metallic (group X and XI) nanoparticles and the prediction of their catalytic properties. Chapter III and IV will follow with a thorough investigation of solid-solid transitions in mono- and bi-metallic nanoparticles. Structural rearrangements will be discussed with a focus on size and composition effects determining whether they are concerted or diffusion driven. Chapter V will tackle a discussion on how to disentangle univocally kinetic and thermodynamic contributions determining phase changes in metallic nanoparticles as well as to discriminate faithfully solid and liquid structures. Finally, Chapter VI will detail the application of a method based upon a geometrical descriptor to determine design criteria towards the synthesis of Pt nanoparticles highly active towards oxygen reduction reaction.

Contents

List of Figures	15
List of Tables	27
Nomenclature	29
1 Introduction	31
1.1 Nanoparticles structures	31
1.2 Nanoalloys chemical ordering	34
1.3 Nanoparticles synthesis	35
1.4 Nanoparticles characterization	36
1.5 Nanoparticles energetic landscapes	37
1.5.1 Structural crossovers at the nanoscale	37
1.5.2 Solid-solid transitions at the nanoscale	38
1.5.3 Phase changes at the nanoscale	39
1.6 Nanoparticles as catalysts	41
2 Numerical Methods	47
2.1 Molecular dynamics	48
2.2 Interatomic potentials	49
2.2.1 Second-moment approximation tight-binding potentials	49
2.2.2 Non-parametric metal-metal interaction potentials	50
2.2.3 Implicit metal-support interaction potential	51
2.2.4 Implicit metal-environment interactions potential	53
2.3 Energetic characterization	54
2.4 Structural characterization	54
2.4.1 Nanocluster giant Icosahedron mapping	54
2.4.2 Pair distance distribution function	55
2.4.3 Radial distribution function	61

2.5	Coordination distributions	63
2.5.1	Nominal coordination number	63
2.5.2	Common neighbour signatures distributions	65
2.6	Nanogenomics and nanoparticles catalytic properties	65
2.6.1	Nanogenome of ideal closed-shell structures	67
2.6.2	Towards in operando conditions	76
2.7	Nanogenomics hydrogen evolution model	78
2.8	Rearrangements characterization	80
2.9	Sampling Techniques in LoDiS	81
2.9.1	Metadynamics	82
2.9.2	Metadynamics collective variables	83
2.9.3	Iterative temperature molecular dynamics	84
2.9.4	Other sampling tools employed for comparison	85
3	On concerted rearrangements in monometallic nanoparticles	89
3.1	Concerted rearrangement in gas phase nanoparticles	89
3.1.1	Computational set-up and analysis method	90
3.1.2	Size and shape effects	91
3.2	Concerted rearrangement in supported nanoparticles	96
3.2.1	Computational set-up and analysis method	97
3.2.2	Support effects	97
3.3	Summary	98
4	On concerted rearrangements in bimetallic nanoparticles	107
4.1	Computational set-up and analysis method	107
4.2	Mismatch effects	108
4.3	Chemical ordering effects	111
4.4	Chemical reordering	113
4.5	Summary	114
5	On phase changes in metallic nanoparticles	119
5.1	Kinetic effects on nanoparticle phase change	119
5.1.1	Computational set-up and analysis method	120
5.1.2	Kinetics driven melting/freezing hysteresis	121
5.2	On the structure of melted and solid nanoparticles	125
5.2.1	Computational set-up and analysis method	125
5.2.2	PDF analysis to characterize melted and solid structures	126

5.2.3	Size-dependent melting phase change temperatures	129
5.2.4	Environment effects on nanoparticle melting	129
5.3	Summary	130
6	On the ideal shape and size of Pt nanoparticles for oxygen reduction	141
6.1	Nanogenomics CHE model for ORR	141
6.2	Static ideal nanoparticles	142
6.3	Structurally rearranging nanoparticles	145
6.3.1	Oxide supported nanoparticles subject to heating	145
6.3.2	Implementing structural disorder via fast annealing	145
6.4	Summary	147
7	Conclusion	153
	Bibliography	155
	Appendix A Building Machine Learning Force fields for nanoclusters	165
	Appendix B PDF KL analysis robustness	175

List of Figures

1.1	Oh (top), To (mid), and Co (bottom) nanoparticles presenting respectively (from left to right, top to bottom) 146 ($n_{edge} = 7$, $n_{cut} = 0$), 344 ($n_{edge} = 8$, $n_{cut} = 0$), 489 ($n_{edge} = 9$, $n_{cut} = 0$), 891 ($n_{edge} = 10$, $n_{cut} = 0$), 201 ($n_{edge} = 7$, $n_{cut} = 2$), 405 ($n_{edge} = 9$, $n_{cut} = 3$), 586 ($n_{edge} = 10$, $n_{cut} = 3$), 976 ($n_{edge} = 13$, $n_{cut} = 4$), 147 ($n_{edge} = 7$, $n_{cut} = 3$), 309 ($n_{edge} = 9$, $n_{cut} = 4$), 561 ($n_{edge} = 11$, $n_{cut} = 5$), 923 ($n_{edge} = 13$, $n_{cut} = 6$), atoms	43
1.2	5-fold twinned decahedra of 278 ($m=1$, $n=2$, $p=4$), 400 ($m=1$, $n=4$, $p=4$), 686 ($m=5$, $n=5$, $p=2$), 561 ($m=5$, $n=5$, $p=1$). atoms	44
1.3	Icosahedra of 147 ($n_{shell} = 3$), 309 ($n_{shell} = 4$), 561 ($n_{shell} = 5$), 923 ($n_{shell} = 6$). atoms	45
1.4	Common chemical arrangements in nanoalloys: Random, Ordered, Multi-Shell, Core-Shell, Off-Centered, Ball+Cup, Janus. Different grey tonalities represent the different A and B chemical species in the nanoalloy.	46
2.1	Lattice corrugation implicit in Equations 2.9 (top-left), 2.10 (top-right), 2.11 (bottom-left), 2.12 (bottom-right), to calculate the b_{ij} coefficients (Equation 2.8).	52

2.2	(A) Visual mapping of a 309 atoms closed-shell polyhedra into a 37995-atoms giant Ih. Though the solid angles are inherently different from the exact values of the ones in a perfect polyhedron, a smaller icosahedron can be readily placed in the innermost shells of a larger one; a decahedron can be formed from a section of an icosahedron along one 5-fold symmetry axis; a crystalline structure from the close-packed tetrahedral space between the gIh five-fold boundaries. (B) 2D-projection of the g-Ih where the coloured regions label the three morphological families where a nanoparticle, represented by a circle, can be placed. Circles might overlap, as in the pink, orange, and green regions. The classification is however univocal, as the position of the center of circle lies in well distinguished regions. The centre of Dh falls in the red rectangle, the Cp's one in the yellow circle, and the Ih's centre within the blue star. (C) Example of low-symmetry nanoparticles where atoms belonging to a five-fold axis are in blue, icosahedral centre in red, and otherwise in white. (D) Nanoparticles in (C) representation onto the 2D-gIh map. Reproduced under CC BY license from Thermodynamics of CuPt nanoalloys - K. Rossi, L. Bartok-Pártay, G. Csanyi, F. Baletto, Scientific reports 8, 2018.	56
2.3	Histograms for the pair distribution functions of Pt nanoparticles of 147 atoms at 300K presenting an Ih morphology for different bin width, reported in the top right corner of each subfigure. Colour coding is also used to discriminate the different PDFs.	59
2.4	Histograms for the pair distribution function of Ag nanoparticles of 147 atoms at 300K presenting a Co (in red), Dh (in green), or Ih (in yellow) morphology.	60
2.5	Atoms accounted for when calculating the nominal coordination of the central atom in dark shadowing. First nearest neighbour shell is delimited by a black circle.	64
2.6	Examples of atoms pairs presenting (5,5,5), (4,2,2), or (4,2,1) common neighbour analysis signatures. The reference nearest neighbour pair is shown in red, their common neighbours are depicted in yellow.	66

- 2.7 Visual representation of the atoms accounted for calculating the generalized coordination of a set of atoms atom in dark red shadowing. First nearest neighbour shells of the dark red atoms are delimited by red circles. Outer neighbour shells atoms determining the GCN of the dark red shaded atoms are inscribed in green circles. Reproduced from Ref. A genomic characterization of metallic nanoparticles - K. Rossi, G.G. Asara, F. Baletto - Physical Chemistry Chemical Physics 21 (9), 4888-4898, 2019 with permission from the PCCP Owner Societies. 68
- 2.8 Nanoparticle GCN fingerprint size evolution in the seven structures under investigation (a snapshot of each is reported along side the graph), for atop (left) and bridge (right) adsorption. The three size regimes where the fingerprint is mobile (pink), incomplete (cyan), or fixed (yellow) are colour coded. Reproduced from Ref. A genomic characterization of metallic nanoparticles - K. Rossi, G.G. Asara, F. Baletto - Physical Chemistry Chemical Physics 21 (9), 4888-4898, 2019 with permission from the PCCP Owner Societies. . . . 69
- 2.9 A visual resume of the non equivalent active sites for atop adsorption in an Octahedron. For each case we report polynomial expressions that allow to estimate each NEAS occurrence as a function of the number of atoms, nl , at the Oh edge. Reproduced from Ref. A genomic characterization of metallic nanoparticles - K. Rossi, G.G. Asara, F. Baletto - Physical Chemistry Chemical Physics 21 (9), 4888-4898, 2019 with permission from the PCCP Owner Societies. 70
- 2.10 A visual resume of the non equivalent active sites for bridge adsorption in an Octahedron. For each case we report polynomial expressions that allow to estimate each NEAS occurrence as a function of the number of atoms, nl , at the Oh edge. Reproduced from Ref. A genomic characterization of metallic nanoparticles - K. Rossi, G.G. Asara, F. Baletto - Physical Chemistry Chemical Physics 21 (9), 4888-4898, 2019 with permission from the PCCP Owner Societies. 71

- 2.11 A visual representation of the genome for Oh morphologies of different size(top left label of each plot). As expected from a geometric argument the relative occurrence of (111) sites, i.e. $GCN(atop)=7.5$, inceases quadratically with cluster size and determines their more frequent occurrence with respect to other NEAS in Oh nanoparticles with more than ~ 3000 atoms.Reproduced from Ref. A genomic characterization of metallic nanoparticles - K. Rossi, G.G. Asara, F. Baletto - Physical Chemistry Chemical Physics 21 (9), 4888-4898, 2019 with permission from the PCCP Owner Societies. 72
- 2.12 Circos plot to represent the relationships between NEAS, labelled according to their GCN value, and the nanoarchitectures they are observed in. Bands of different colour connect NEAS (left portion of the circle) and the nanoarchitecture (right portion of the circle) they belong to. For each architecture we report the relative (outer circle) and nominal (inner circle) occurrence of each non equivalent active site. For each NEAS we report their relative (outer circle) and nominal (inner circle) distribution in the different nanoparticles under consideration. Reproduced from Ref. A genomic characterization of metallic nanoparticles - K. Rossi, G.G. Asara, F. Baletto - Physical Chemistry Chemical Physics 21 (9), 4888-4898, 2019 with permission from the PCCP Owner Societies. 74
- 2.13 Representation of the spherical sector exclusion zone of active sites from the genome for the case of nanoparticles supported on a substrate. Atoms in grey are excluded from the genome, the others are colour coded according to their generalized coordination (blue = low coordinated, hot = highly coordinated). Atoms in grey contribute to the coordination of their neighbours even if excluded from the genome. 77
- 2.14 $GCN(atop)$ nanogenome of an Icosahedral nanoparticle of 561 atoms in the gas phase (left) and supported on an MgO substrate (red) where the exclusion principle discussed above diminishes each NEAS occurrence. 78
- 2.15 Top panel shows an Icosahedral nanoparticles of 561 atoms where atoms are colour coded according to their generalized coordination, from light tones (green = lower coordinated) to hot ones (orange = highest coordinated). The ligated atom is highlighted in blue and its Tolman cone is represented by a grey shadowing. Lower panel displays the $GCN(atop)$ nanogenomes of the nanoparticle in the gas phase (top left), and according to Model 1 (top right), Model 2 (bottom left), and Model 3 (bottom right). 87

- 3.1 Initial, "saddle", and final configurations during a DSD rearrangement of an Ih into Dh (top) and Co (bottom). Multicolored atoms delimit a facet in the original Ih. Rotation along the depicted axis is of 36° for the Dh and of 60° for the Co. Note that the axis of rotation lies along a five-fold axis in the Dh case, so to always preserve it during the rearrangement. The rotation axis instead lies along two (111) facets centers for the Co case. "Reproduced from Metallic nanoparticles meet metadynamics - L. Pavan, K. Rossi, F. Baletto, The Journal of Chemical Physics 143 (18), 184304, 10 2015, with the permission of AIP Publishing." 100
- 3.2 Example snapshots describing how surface peeling of a Decahedral nanostructure may proceed. Colour coding reflects atoms coordination: vertexes and adatoms are black, edges coloured are dark-red, atoms in (100) and (111) facets are red and orange respectively, atoms in re-entrances (coordination larger than 9) are yellow, bulk-like atoms are in grey. 101
- 3.3 Structure and rearrangement characterization for a Dh to Ih transition in Ag55 sampled by itMD. The top panel displays snapshots of representative structures observed during the simulation and the corresponding time at which they are first formed. Lower panels show the evolution of the (555) and (200) CNA signature percentages, H and C , respectively the collectivity and concertedness indexes, and coordination number distributions during the course of the simulation. Reproduced from The effect of size and composition on structural transitions in monometallic nanoparticles - K. Rossi, L. Pavan, Y.Y. Soon, F. Baletto, The European Physical Journal B 91 (2), 33, 3, 2018 under Creative Commons Attribution 4.0 International License. 102
- 3.4 Structure and rearrangement characterization for a Dh to defected Dh transition in Ag561 sampled by itMD. Panel ordering follows what described in Figure 3.3. Reproduced from The effect of size and composition on structural transitions in monometallic nanoparticles - K. Rossi, L. Pavan, Y.Y. Soon, F. Baletto, The European Physical Journal B 91 (2), 33, 3, 2018 under Creative Commons Attribution 4.0 International License. 103
- 3.5 Structure and rearrangement characterization for a Dh to Ih transition in Cu309 sampled by itMD. Panel ordering follows what described in Figure 3.3. The transition happens after just few tens of ps from the start of the sampling. 103

- 3.6 Resume of the largest sizes at which rearrangements via DSD mechanism are observed, depending on the nanoparticle composition and interaction stickyness. 104
- 3.7 Top panel reports the caloric curve for the melting of a Pt₅₆₁ nanoparticle on MgO(100). Colour coding reports the nanoparticle (555) CNA signatures percentage (hot colours for 5-fold twinned structures, dark for crystalline ones). Mid panel shows snapshots of the system during its dynamical evolution. Pt atoms are in grey, Mg in green and O in red. The thin lines show the binning in height-distribution function. Lower panel displays the evolution of the number of atoms in each layer, layer 1 being the lowermost. Reproduced with Permission from Melting of large Pt@ MgO (1 0 0) icosahedra - K. Rossi, T. Ellaby, L.O. Paz-Borbón, I. Atanasov, L. Pavan, F. Baletto, Journal of Physics: Condensed Matter 29 (14), 145402, 10, 2017. 105
- 4.1 (422) CNA signature, in %, of the whole nanoparticle (top) and the 55-atoms core (bottom) for Au₅₅@Ag₉₂ (left) and Pt₅₅@Ag₉₂ (right) during the course of MetaD runs at 300K. Reference values for ideal Ih, Dh, and Co geometries are shown via a straight gold, green and red line. When Ih, Dh and Co geometries are sampled, the plot is highlighted in yellow, dark-green or pink. A representative snapshot for each of the above mentioned geometries is reported. Au atoms are in gold, Ag atoms are in silver, Pt atoms are in blue. Left Panel image is partially editated from Controlling Structural Transitions in AuAg Nanoparticles through Precise Compositional Design - A.L. Gould, K. Rossi, C.R.A. Catlow, F. Baletto, A.J. Logsdail, The Journal of Physical Chemistry Letters 7 (21), 4414-4419, 7, 2016 <<https://pubs.acs.org/doi/10.1021/acs.jpclett.6b02181>>, further permissions related to the material excerpted should be directed to ACS. Right panel image is reproduced from Ref. The effect of chemical ordering and lattice mismatch on structural transitions in phase segregating nanoalloys - K. Rossi, F. Baletto, Physical Chemistry Chemical Physics 19 (18), 11057-11063, 5, 2017 - Themed collections: 2017 PCCP HOT articles with permission from the PCCP Owner Societies. 109

- 4.2 (422) CNA signature, in %, of the whole nanoparticle (top) and the 55-atoms core (bottom) for $\text{Cu}_{55}@\text{Ag}_{92}$ during the course of MetaD runs at 300K. Reference values for ideal Ih, Dh, and Co geometries are shown via a straight gold, green and red line. When Ih, Dh, and Co geometries are sampled, the plot is highlighted in yellow, dark-green, and pink. A representative snapshot for each of the above mentioned geometries is reported. Cu atoms are in copper, Ag atoms are in silver. Image is reproduced from Ref. The effect of chemical ordering and lattice mismatch on structural transitions in phase segregating nanoalloys - K. Rossi, F. Baletto, Physical Chemistry Chemical Physics 19 (18), 11057-11063, 5, 2017 - Themed collections: 2017 PCCP HOT articles with permission from the PCCP Owner Societies. 110
- 4.3 (422) CNA signature %, in Cu|Ag nanoparticles during the course of itMD runs. Note the two different timescales reported (0.5 ns for the Co→Ih transition, and 4 ns for the Dh→Ih case.) Reference values for ideal Ih, Dh, and Co geometries are shown via a straight gold, green and red line. When Ih, Ih|Dh, Dh and Co geometries are sampled, the plot is highlighted in yellow, light-green, dark-green or pink. A representative snapshot for each of the above mentioned geometries is reported. Cu atoms are in copper, Ag atoms are in silver. Image is reproduced from Ref. The effect of chemical ordering and lattice mismatch on structural transitions in phase segregating nanoalloys - K. Rossi, F. Baletto, Physical Chemistry Chemical Physics 19 (18), 11057-11063, 5, 2017 - Themed collections: 2017 PCCP HOT articles with permission from the PCCP Owner Societies. 112

- 4.4 The upper panel shows the comparison between the energetic landscape sampled during MetaD simulations at 300K for $\text{Au}_{55}@\text{Ag}_{92}$ and $\text{Ag}_{55}@\text{Au}_{92}$. Landmarks are signalled with letters. The corresponding structure and its potential energy are also reported for comparison. Note how energetically favourable low symmetry Ih-like motifs are sampled only for the case of $\text{Ag}_{55}@\text{Au}_{92}$. The lower panel displays the transition pathways for $\text{Co} \leftrightarrow \text{Ih}$ in $\text{Ag}_{55}@\text{Au}_{92}$ (and $\text{Ag}_{55}@\text{Au}_{80}@\text{Ag}_{12}$ for the descriptive purpose of comparing with another Au-outer-layer rich system). A vertical dashed line in each plot indicates where the transition from/to CO-like to/from Ih-like motifs occurs. The star symbol indicates the lowest energy rosette-Ih minima encountered, a rosette-defected Ih structure. image is partially editated from Controlling Structural Transitions in AuAg Nanoparticles through Precise Compositional Design - A.L. Gould, K. Rossi, C.R.A. Catlow, F. Baletto, A.J. Logsdail, The Journal of Physical Chemistry Letters 7 (21), 4414-4419, 7, 2016 <<https://pubs.acs.org/doi/10.1021/acs.jpclett.6b02181>>, further permissions related to the material excerpted should be directed to ACS. 115
- 4.5 Typical snapshots during an itMD dynamics of a $\text{Ag}_{85}\text{Cu}_{62}$ Dh up to the melting. Five regions are found, shadowed by different colours, in correspondence of changes in the (4,2,2) %. The first 4 ns correspond to the one reported in Figure 4.3 right panel. μ and G^α show that the initial Janus ordering is altered only after the formation of a Ih. A core@shell ordering is completely formed only after 600 K, very close if not after the melting point. From the evolution of the R^α and H^α parameters, Ag (grey dots) is initially more mobile than Cu (orange). Ag starts to move clearly after 450 K with the formation of a defected Ih in the silver half, while the latter only above 550 K. Image is reproduced from Ref. The effect of chemical ordering and lattice mismatch on structural transitions in phase segregating nanoalloys - K. Rossi, F. Baletto, Physical Chemistry Chemical Physics 19 (18), 11057-11063, 5, 2017 - Themed collections: 2017 PCCP HOT articles with permission from the PCCP Owner Societies. 116

- 4.6 Evolution of the chemical radius of gyration (G^α) and of the segregation parameter (μ) for Ag (silver) and Pt (blue), during a HeCN driven MetaD at 300K starting from an Ih Pt₅₅@Ag₉₂ architecture. Image is reproduced from Ref. The effect of chemical ordering and lattice mismatch on structural transitions in phase segregating nanoalloys - K. Rossi, F. Baletto, Physical Chemistry Chemical Physics 19 (18), 11057-11063, 5, 2017 - Themed collections: 2017 PCCP HOT articles with permission from the PCCP Owner Societies. 117
- 5.1 Caloric curves for the freezing of a Cu₁₆₂Pt₁₄₇ liquid droplet: scattered points and filled circles refer to the itMD data averaged as discussed in the text, lines are guides to the eye only. Colours refer to λ , where a lighter blue tone corresponds to faster rate. NS results are shown by black and white dashed lines, and they should be considered as quasi-thermodynamic limit for that system. Reproduced under CC BY license from Thermodynamics of CuPt nanoalloys - K. Rossi, L. Bartok-Pártay, G. Csanyi, F. Baletto, Scientific reports 8, 2018. 121
- 5.2 Top panel shows the melting caloric curves of the previously solidified Cu₁₆₂Pt₁₄₇ by itMD, scattered points and filled circles as in Fig. 5.1. Colours refer to λ , where a lighter red tone corresponds to faster rate. NS results (black and white dashed lines) are reported as reference point. The inset displays the temperature-width, between the highest temperature at which the nanoparticle is always solid during heating, T_m , and T_f , the lowest temperature at which nanoalloys are liquid during cooling, against λ . Reproduced under CC BY license from Thermodynamics of CuPt nanoalloys - K. Rossi, L. Bartok-Pártay, G. Csanyi, F. Baletto, Scientific reports 8, 2018. 123
- 5.3 Radial distribution of atoms around the centre-of-mass as a function of temperature. The top two panel shows an example itMD run with a $\lambda = 10^9$ K/s for melting and freezing, respectively, while the bottom panel shows the results from NS calculations. The left hand side panels show the overall distribution of atoms, while the right hand side figures show the relative occurrence of Cu atoms within the nanoparticle. The estimated phase change temperatures are marked by arrows for reference. Reproduced under CC BY license from Thermodynamics of CuPt nanoalloys - K. Rossi, L. Bartok-Pártay, G. Csanyi, F. Baletto, Scientific reports 8, 2018. 124

5.4	Average pair distance distribution function of Pt nanoparticles of different shapes and sizes (146 - 147 - 192 - 201) at 900 K and 1500 K. The top right corner of each subfigure shows the solid structure and an example snapshot of structures observed at 1500 K in the same system.	131
5.5	Average pair distance distribution function of Pt nanoparticles of different shapes and sizes (309 - 344 - 389 - 405) at 900 K and 1500 K. The top right corner of each subfigure shows the solid structure and an example snapshot of structures observed at 1500 K in the same system.	132
5.6	Average pair distance distribution function of Pt nanoparticles of different shapes and sizes (434 - 489 - 561 - 586) at 900 K and 1500 K. The top right corner of each subfigure shows the solid structure and an example snapshot of structures observed at 1500 K in the same system.	133
5.7	Average pair distance distribution function of Pt nanoparticles of different shapes and sizes (686 - 891 - 923 - 976) at 900 K and 1500 K. The top right corner of each subfigure shows the solid structure and an example snapshot of structures observed at 1500 K in the same system.	134
5.8	Temperature dependent average pair distance distribution function of a Pt ₂₀₁ nanoparticle. The second neighbour peak of the PDF is absent for temperatures above 1160 K while a shoulder persists at 1130 K.	135
5.9	Excess energy and KL(h c) temperature dependence in Pt nanoparticles of different sizes (see label on bottom right corner). A quasi first order transition, simultaneous in both order parameters, signals nanoparticle melting. Results for different temperature bins averaging are in quantitative agreement. . . .	136
5.10	Excess energy and KL(h c) temperature dependence in Pt nanoparticles of different sizes (see label on bottom right corner). A quasi first order transition, simultaneous in both order parameters, signals nanoparticle melting. Results for different temperature bins averaging are in quantitative agreement. . . .	137
5.11	Size-dependent melting temperatures of Ag (top-left), Au (top-right), Pt (bottom-left), and Cu (bottom-right) nanoparticles. Fitted curves follow the equation $T_{melt} = b + a/N^3$	138

- 5.12 Excess energy and KL(h|c) temperature dependence in a Pt nanoparticle of 201 atoms immersed in an implicit strongly interacting environment modelled according to Equation 2.13 ($\rho=2$, $\epsilon=0.04\text{eV}$). A quasi first order transition in the KL(h|c) signals the nanoparticle melting, yet this is less evident from the caloric curves. Pink, red, purple, and violet data points report the excess energy per temperature observed in each independent run, dark yellow points show their average according to what discussed in subsection 5.2.1. The KL(h|c) data are reported in blue. 139
- 6.1 Left panel: GCN-genomes for seven Pt-geometries (listed in the y-axis labels), at 1.5, 3.5, 5.5 and 7.5 nm diameter. A complete GCN fingerprint appears above 3.5 nm, while the occurrence of (111) and (100) sites become predominant only above 5.5 nm. Right panel: Corresponding theoretical I-V curves calculated at room temperature. 148
- 6.2 Size-dependent mass activity in several re-entrant decahedra, presenting m in the 1-3 range, p between 2 to 6 atoms, and n in the 2-11 range. Sets of pentagonal bypyramids cuts are colour coded according to their p and labelled by different symbols according to their m . Conversely 10 points, corresponding to the 2-11 n values, are reported per each set. The diameter label corresponds to the longest axis in the nanoparticle, calculated according to Equation 1.4. 149
- 6.3 Size dependent mass activity of seven different Pt nanoparticles morphologies (labelled in the bottom right corner of each subfigure). 150
- 6.4 Example genome (greyscale) and η_1 (orange) evolution for an Ih_{561} soft-landed upon a pristine MgO undergoing thermally driven structural rearrangement. Reference η_1 value for Pt(111) extended surface is reported in green. Snapshot to depict the structural evolution of the nanoparticle are also reported. Mg atoms are in green, O atoms are in red, Pt nanoparticle atoms are in grey if not counted in the genome, or colour coded according to their generalized coordination (aqua (hot) tones for low (high) coordinated atoms). 151
- 6.5 Left panel: Example genomes and η_1 evolutions for a Pt_{561} nanoparticle undergoing a liquid-to-solid transition. Notwithstanding the two different structures observed, a similar η_1 is predicted. Right panel: Pt nanoparticles resulting from the freezing of a liquid droplets, atoms are colour coded according to their generalized coordination (aqua tones for low coordinated atoms, hot tones for highly coordinated ones). 152

- B.1 Pt 201 nanoparticle KL(h|c) temperature dependent evolution for the choice of different cold reference structures. When choosing cold structures after the melting point, no jump in the KL(h|c) versus Temperature curve is observed. 176
- B.2 Pt 201 nanoparticle KL(h|c) temperature dependent evolution for the choice of 10 PDF binning width, from 0.1 Å to 1 Å. The choice of a distance bin larger than more than half of the distance between first and second nearest neighbours peaks yields a profile in the KL(h|C) versus temperature plot not presenting a clear jump at the phase change. An increase in the bin width corresponds to a decrease in the KL(h|c) values observed. 177
- B.3 The temperature evolution of the KL(h|c) of the whole (left) or limited to the bulk lattice parameter distance (right) PDF of a 146 (top) and 344 (bottom) atoms Cu nanoparticles with an initial Oh morphology is shown by green points linked by a line which acts a guide to the eye. CNA signatures relative occurrence is reported in shades of blue (navy = (5,5,5), blue = (4,2,2), cyan = (4,2,1)). 178

List of Tables

2.1	Resume' of the Rosato-Guillope-Legrande potentials parametrizations used in the systems investigated in this work.	50
3.1	Recap of data gathered for rearrangement of an initial Dh structure. Per each system (leftmost column) we report $\rightarrow Ih$ %, the $\overline{C_{\rightarrow Ih}^{max}}$ and $\overline{T_{\rightarrow Ih}}$, or, $\overline{C_{T \rightarrow dDh}^{max}}$ and $\overline{T_{\rightarrow dDh}}$, for simulations ending respectively in the Ih or defected-Dh (dDh) funnel as found via itMD. $\overline{T_{\rightarrow Ih}}$ and $\overline{T_{\rightarrow dDh}}$ are normalized over the corresponding nanoparticle melting temperature. The error on $\overline{C_{\rightarrow Ih}^{max}}$, $\overline{C_{\rightarrow dDH}^{max}}$, $\overline{T_{\rightarrow Ih}}$, and $\overline{T_{\rightarrow dDh}}$ is taken as the maximum deviation of their estimate, from each single independent run, with respect to the corresponding average value. It is around 0.1 for the concertedness index and of 0.03 for the characteristic transition temperatures. Rightmost column reports $\overline{\Delta F_{\rightarrow Ih}}$, and $\overline{\Delta F_{\rightarrow Dh}}$ in bracket if observed. Error on $\overline{\Delta F}$ as found from simulations sampling both basins can heuristically considered as the height of one deposited Gaussian. In the other cases the reported value represents an overestimate, and thus an upper bound of the true free energy barrier.	93

- 3.2 Recap of data gathered for rearrangement of an initial Dh structure. Per each system (leftmost column) we report $\rightarrow\text{Ih}$ %, the $\overline{C_{\rightarrow\text{Ih}}^{\text{max}}}$ and $\overline{T_{\rightarrow\text{Ih}}}$, or, $\overline{C_{T_{\rightarrow\text{dFCC}}}^{\text{max}}}$ and $\overline{T_{\rightarrow\text{dFCC}}}$, for simulations ending respectively in the Ih or defected FCC funnel. $\overline{T_{\rightarrow\text{Ih}}}$ and $\overline{T_{\rightarrow\text{dDh}}}$ are normalized over the corresponding nanoparticle melting temperature. The error on $\overline{C_{\rightarrow\text{Ih}}^{\text{max}}}$, $\overline{C_{\rightarrow\text{dFCC}}^{\text{max}}}$, $\overline{T_{\rightarrow\text{Ih}}}$, and $\overline{T_{\rightarrow\text{dFCC}}}$ is taken as the maximum deviation of their estimate, from each single independent run, with respect to the corresponding average value. It is around 0.1 for the concertedness index and of 0.03 for the characteristic transition temperatures. Rightmost column reports $\overline{\Delta F_{\rightarrow\text{Ih}}}$, and $\overline{\Delta F_{\rightarrow\text{FCC}}}$ in bracket if observed. Error on $\overline{\Delta F}$ as found from simulations sampling both basins can heuristically considered as the height of one deposited Gaussian. In the other cases the reported value represents an overestimate, and thus an upper bound of the true free energy barrier. 94
- 5.1 Percentages of the three morphological families as found in itMD freezing simulations at different λ and NS, taken just below T_{pc} . The itMD occurrence corresponds to temperatures at 700 K, below which no morphological changes are observed, and they are averaged over all the 25 independent runs. The nested sampling percentages are reported for the two runs exploring all basins. 122
- 5.2 Infinite size limit temperature predicted for nanoparticles of Pt, Cu, Ag, Au, and their corresponding bulk melting temperature. 129

Nomenclature

Other Symbols

\leftrightarrow Transition between

\rightarrow Transition to

Acronyms / Abbreviations

CHE Computational Hydrogen Evolution

CNA Common Neighbour Analysis

Co Cuboctahedron

CV Collective Variable

DSD Diamond-Square-Diamond

EXAFS Extended X-ray adsorption fine structure

fcc Face centered cubic

GD Geometrical Descriptor

IDh Ico-Decahedron

g-Ih Giant Icosahedron

Ih Icosahedron

itMD iterative temperature Molecular Dynamics

KL Kullback Leibler Divergence

LoDiS Low Dimensional System software

MDh Marks Decahedron

MetaD Metadynamics

MPDN Maximum Pair Distance Number

NEAS Non equivalent adsorption sites

NS Nested Sampling

NVE Microcanonical ensemble

NVT Canonical ensemble with fixed Temperature

Oh Octahedron

ORR Oxygen Reduction Reaction

PDF Pair Distribution Function

RDF Radial Distribution Function

SFN Stacking Fault Number

STEM Scanning Tunneling Electron Microscope

To Truncated Octahedron

XANES X-ray adsorption near edge

XAS X-ray adsorption spectroscopy

Chapter 1

Introduction

This chapter aims at introducing a framework to characterize nanoparticles architectures, to briefly present nanoparticle synthesis and characterization techniques, to detail the features of nanoparticles energetic landscapes, and to discuss nanoparticles applications in catalysis. Here, and in the rest of the thesis, the term nanoparticle is used to refer to finite-size systems of noble and quasi noble metal (group X and XI metals) atoms, whose size ranges from the 100 to the 1000 units.

1.1 Nanoparticles structures

Finite-size effects imply that many isomers - i.e. configurations with the same number of atoms which arranged in different fashions - are energetically competitive. The two most prominent paradigms driving stabilization in a nanoparticle are electronic and geometric shell closure. The latter is of particular relevance in determining the stability of a given nanoparticle geometry for sizes above the many tens of atoms and consists in the formation of complete outer shells, with the same symmetry of the inner ones, with no low-coordinated atoms or defected facets. A facile categorization of common closed-shell geometrical motifs observed *in vitro* discriminates structures depending on whether they present a crystalline arrangement or twinning(s). Motif dependent magic numbers series for both crystalline and twinned nanoparticles have been thus found analytically in the past to readily identify the nuclearities - i.e. the number of atoms - for which geometric shell-closure takes place.

Single-crystal nanoparticles According to an energy minimization argument, and assuming that the strain contributions to the total energy are minimized by the internal crystalline structure, one can argue that a nanoparticle, where the number of atoms at the edge and vertices is negligible, will be terminated by the lowest surface energy facet(s). In particular the Wulff construction states that:[2] *the normal vector length from the center of the nanoparticle to any of its facets is proportional to the surface free energy of the facets themselves.*

For the case of group X and XI metals, surface energies for low Miller index surfaces rank as $\gamma(111) > \gamma(100) > \gamma(110) > \gamma(\text{higher index})$. Depending on the ratio $\gamma(111)$ over $\gamma(100)$ the Octahedron, or one of its truncations, result as the energetically favourable morphology. The magic number series to enumerate the atoms in an Octahedron (Oh) is:[3]

$$N_{atoms} = \frac{2n_{edge}^3 + n_{edge}}{3}, \quad (1.1)$$

where n_{edge} is the number of atoms on its edge. By introducing the free parameter n_{cut} to describe the number of atoms removed through a cut parallel to a square (100) plane crossing the Octahedra, one can further enumerate the atoms in any closed-shell cut of an Octahedron:

$$N_{atoms} = \frac{2n_{edge}^3 + n_{edge}}{3} - 2n_{cut}^3 - 3n_{cut}^2 - n_{cut} \quad (1.2)$$

A regular truncated Octahedra (To), presenting regular hexagonal (111) facets and square (100) facets, is found for $n_{edge} = 3n_{cut} + 1$, while a cubo-octahedron (Co), displaying alternating triangular (111) and square (100) facets, is obtained when $n_{edge} = 2n_{cut} + 1$. [3]

Figure 1.1 shows example nanoparticles with an Oh, a To, or a Co morphology and highlights the relation between the Oh size, the length of its edge n_{edge} , and the nuclearity of its truncations, dictated by the parameter n_{cut} . We note that other cuts of a fcc crystal can enable to expose only (100) facets, resulting in a cubic structure, or other arrangements of (111) and (100), e.g. Rhombic Dodecahedra. These structures are however not discussed here because of their relatively low energetic stability with respect to the Oh, To, Co fcc cuts in the size regime investigated in this thesis.

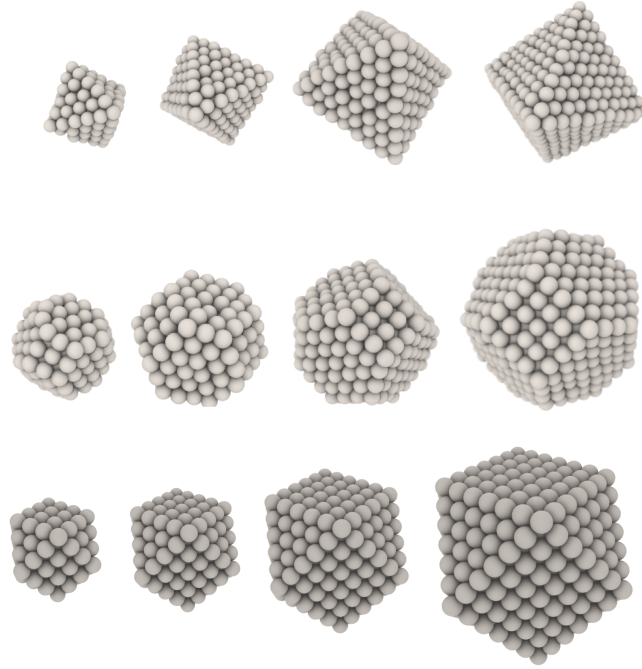


Figure 1.1 Oh (top), To (mid), and Co (bottom) nanoparticles presenting respectively (from left to right, top to bottom) 146 ($n_{edge} = 7$, $n_{cut} = 0$), 344 ($n_{edge} = 8$, $n_{cut} = 0$), 489 ($n_{edge} = 9$, $n_{cut} = 0$), 891 ($n_{edge} = 10$, $n_{cut} = 0$), 201 ($n_{edge} = 7$, $n_{cut} = 2$), 405 ($n_{edge} = 9$, $n_{cut} = 3$), 586 ($n_{edge} = 10$, $n_{cut} = 3$), 976 ($n_{edge} = 13$, $n_{cut} = 4$), 147 ($n_{edge} = 7$, $n_{cut} = 3$), 309 ($n_{edge} = 9$, $n_{cut} = 4$), 561 ($n_{edge} = 11$, $n_{cut} = 5$), 923 ($n_{edge} = 13$, $n_{cut} = 6$), atoms

Multiply-Twinned Nanoparticles A further development on the initial work by Wulff, first presented by Marks, consisted in accounting for and rationalising the presence of multiple twin boundaries in a nanoparticle.[4] Among multiply twinned nanoparticle, cuts of a pentagonal by-pyramid, either parallel or propagating to its 5-fold symmetry axis, present a significant structural stability. The number of atoms in these architectures is determined by the following equation:[3]

$$N_{dh} = \frac{1}{6}[30p^3 - 135p^2 - 207p - 102 + [5m^3 + (30p^2 - 45)m^2 + (60(p^2 - 3p) + 136)m] + n[15m^2 + (60p^2 - 75)m + 3(10p^2 - 30p) + 66]] - 1 \quad , \quad (1.3)$$

with m , n , and p labelling respectively the number of atoms along the edge parallel to the 5-fold axis and belonging to the (100) facets arising from the cuts, the number of atoms along the edge of the 5-fold hats delimited by (111) facets, and the number of atoms along the re-entrances.

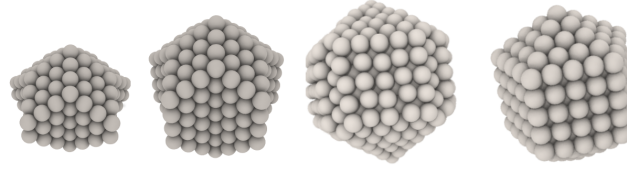


Figure 1.2 5-fold twinned decahedra of 278 ($m=1, n=2, p=4$), 400 ($m=1, n=4, p=4$), 686 ($m=5, n=5, p=2$), 561 ($m=5, n=5, p=1$) atoms

In turn the height, h of the decahedron (i.e. the number of atoms lying along the 5-fold twin) results equal to:[3]

$$h = m + n + 2p - 3 \quad . \quad (1.4)$$

If no re-entrances are present in the nanoparticle, $p = 1$, we will refer to the structure as an Ino-Decahedron (Idh), and as a Marks-Decahedron (Mdh) otherwise. Figure 1.2 gathers few examples of nanoparticle morphologies for different choices of m , n , and p .

Icosahedral structures are also prominent among multiply twinned nanoparticles. This motif consists of 20 strained tetrahedra which meet at the center of the nanoparticle. The contributions due to the strain resulting from the many twins in the structure are counter-balanced by the optimization of the number of bonds among the atoms in the system. The equation describing the Ih magic sizes is: [3]

$$N_{atoms} = \frac{10}{3}n_{shell}^3 - 5n_{shell}^2 + \frac{11}{3}n_{shell} - 1 \quad (1.5)$$

where n_{shell} is the number of atomic shells surrounding the central atom. Figure 1.3 shows a set of nanoparticles presenting an Ih morphology and different number of shells.

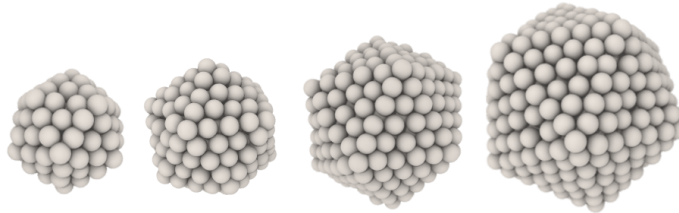


Figure 1.3 Icosahedra of 147 ($n_{shell} = 3$), 309 ($n_{shell} = 4$), 561 ($n_{shell} = 5$), 923 ($n_{shell} = 6$) atoms

1.2 Nanoalloys chemical ordering

The presence of two chemical species in a metallic nanoparticle introduces a further degree of complexity, but also an additional parameter that enables the tuning of the nanoparticle chemophysical properties. Beyond the nanoparticle structure, the stoichiometry and ordering of the two species in fact deliver significant contributions in determining the nanoparticle chemophysical properties. Common chemical patterns of metallic nanoalloys are shown in Figure 1.4.

Core-Shell and Janus display a high degree of segregation. In the latter, the two chemical species share a planar interface, in the former a quasi-spherical one. Between the two we find the Ball+Cup arrangement, where one of the two chemical species is partially exposed, and the Off-centre Core-Shell, where spherical symmetry breaking is caused by strain minimization. Multi-Shell, Ordered, and Random arrangements instead correspond to more mixed chemical orderings. When atoms of a certain chemical species are energetically favourable in subsurface positions, a Multi-shell pattern is likely to be formed. In nanoalloys of magnetic species which display ordered arrangements in the bulk it is often possible to observe such order also at the nanoscale. Random arrangements are instead formed by chemical species which present a strong tendency to alloy and mix. Factors which may lead to the preference of a chemical arrangements with respect to another are: [5, 6]

- According to an energy minimization argument, the number of strongest bonds tends to be maximized. In turn, if hetero bonds are the most energetically favourable, mixing will take place, otherwise, the species with the strongest homonuclear bonds will preferentially occupy the core of the nanoparticle.
- According to an energy minimization argument, atoms with the lower energy surface tend to occupy the external shell.
- According to a stress/strain minimization argument, symmetry breaking in the presence of two chemical species with large mismatch can take place, with larger atomic radius chemical species generally displaying a tendency towards segregation in the outer shells of the nanoalloy.
- More complex aspects, e.g., charge transfer and magnetic ordering effects, or extrinsic factors such as solvation, ligand or support affinity (see e.g. [7–9]).

In the rest of the thesis the following notation will be employed to identify the chemical ordering of the nanoalloy under consideration and, if possible, the specific location of atoms of a given chemical species therein: given two chemical species A and B, A@B characterizes core-shell architectures, A@B@A multi-shells, A||B Janus.

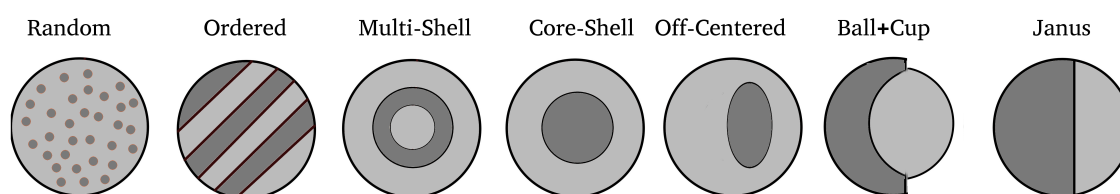


Figure 1.4 Common chemical arrangements in nanoalloys: Random, Ordered, Multi-Shell, Core-Shell, Off-Centered, Ball+Cap, Janus. Different grey tonalities represent the different A and B chemical species in the nanoalloy.

1.3 Nanoparticles synthesis

Nanoparticle synthesis can take place via many different techniques, which can be differentiated in two broad categories: colloidal methods and aggregation sources methods. Although based upon completely different premises, as detailed in the next paragraphs, both present at their final stage, a bottom-up step where metallic atoms gather to form nanoclusters (few to ~ 100 atoms) which then grow into nanoparticles. The kinetic effects influencing the final nanoparticles structure are key in determining the synthesis of morphological polydisperse samples which may encompass many different metastable motifs. The investigations presented in this work are not explicitly geared toward the study of formation processes, however they are intimately related to the implications inherent to the kinetic effects determining the synthesis of metastable structures. It is thus advantageous to briefly discuss the features of the most prominent synthesis techniques.

Colloidal Methods In colloidal chemistry, metallic precursors react in a solvent to nucleate and grow a nanoparticle. This practice represents a successful route to produce highly size and shape monodisperse samples. This is an essential step towards univocally establishing the significance of the size, shape, and chemical composition interplay which determines the chemophysical properties of a nanoparticle. A strong control on the final nanoparticle morphology is obtained by the modification of the surface energetics through the presence of surfactants which enable the stabilization of target surface(s) against others. Being kinetically driven, this approach also allows to stabilize metastable geometries. It is however debated how to systematically fine-tune solvent composition, precursors composition, and temperature to achieve programmable synthesis routes. [7, 8, 10, 11] Numerical methods that encompass the complexity of growth and nucleation in solutions have been only recently developed, yielding very promising insights for specific case studies.[12, 13, 11]

Aggregation Sources Methods In aggregation sources, metallic atoms collide to form a liquid droplet or to favour the growth of a solid-seed. Coalescence among seeds may also take place. Different techniques can be employed to drive the collisions between metallic atoms and control their aggregation:

- in inert gas aggregation sources, a vapour of atoms is supersaturated via a cold inert gas and condensed so to form a nanoparticle. [14]
- in laser ablation, the nanoparticle material feedstock is pulsed with a high energy laser which extracts atoms which are successively gathered by an injection of a cooling carrier gas to drive aggregation. [15]
- in matrix assembled cluster sources, metallic atoms are embedded in an inert gas matrix which is then bombarded by argon ions of few keV of energy to promote the formation of nanoparticles. [16, 17]

Control on the final nanoparticle architecture, beyond technique-specific parameters, is obtained by fine tuning metallic atoms density and kinetic energy. While nanoparticle architecture control may result less trivial than in colloidal methods, a high yield of nanoparticle grams per hours has been recently demonstrated in matrix assembly cluster sources.[16–18] Many numerical studies, especially for the case of inert gas sources greatly helped in establishing the contribution of kinetic, energetic, and thermodynamic effects on the structures of nanoparticles after synthesis.[19–21]

1.4 Nanoparticles characterization

The characterization of nanoparticles structures is pivotal towards understanding their chemical-physical properties because of the structure-property relationship inherent to these systems. The great advancements witnessed in the past 50 years in experimental measurement techniques largely benefited cluster science and the potential application of nanoparticles in technological devices. Among the several techniques available, we will briefly discuss here two of the most prominent, High Resolution Tunnelling Electron Microscopy (HRTEM) and X-ray Absorption Spectroscopy (XAS). The resolution accessible to these methods has been fundamental in determining accurately nanoparticles structure, and, conversely establishing an understanding of their (meta)stability, as discussed in Subsection 1.5.2.

HRTEM An high resolution Tunnelling Electron Microscopy image is taken by registering the interference in the image plane of an electron wave with itself. Correcting for aberration errors enables measurements to obtain a sub-angstrom resolution. For the case of high angle annular dark field images (HAADF), data are recorded from the fore-scattered electrons impinging an annular detector outside the path of the direct beam. The received intensity is thus proportional to the atomic number, with heavy atom bright, but light atoms difficult to be observed.[22]

XAS X-ray Absorption Spectroscopy consists in recording, as a function of the incident x-ray energy and transmitted intensities. When the binding energy of an electron of an atom within the sample is matched by one of the incident x-rays, the adsorbed intensity peaks, while the transmitted signal diminishes greatly. This results in each element presenting a set of unique absorption fingerprints corresponding to the different binding energies of its electrons. XAS yields information on both Extended X-Ray Absorption Fine Structure (EXAFS) and X-ray Absorption Near Edge Structure (XANES). XANES corresponds to x-rays absorptions which are determined by core transitions to quasi bound states, i.e. multiple scattering resonances in the 10-150 eV kinetic energy regime (above the chemical potential).[23] Measurements in this regime can be utilized also to probe the coordination of atoms, as the latter strongly affects the features in the spectra.[24] For higher kinetic energies EXAFS (Extended X-ray Absorption Fine Structure) information is dominant, this regime being characterized by single scattering events.[23]

1.5 Nanoparticles energetic landscapes

The formalism of energetic landscapes is highly suited in discussing in a comprehensive and coherent fashion the complexity inherent to energetic, thermodynamic and kinetic contributions [25, 26] to nanoparticles structural stability as a function of size, composition, and temperature. The term energy landscape is here understood as a mapping of the nanoparticle conformations according to their energy. Local minima will lie on valleys, and transition states will occupy the top of the hills dividing the basins.[27, 28]

1.5.1 Structural crossovers at the nanoscale

During experimental synthesis through physical growth methods, it was observed that at sizes above few nanometers nanoparticles present more often fcc cut motifs, while 5-fold symmetric twins and icosahedral morphologies were more common for smaller nanoparticles.

This suggested a systematic change in the energetic landscape of nanoparticles of different sizes, where crystalline structure appeared more and more favourable at increasingly larger nuclearities. In the past, these trends were rationalized numerically by systematically investigating the energies of magic size crystalline (Oh, To, Co), 5-fold twinned (Idh, Mdh), and Icosahedral (Ih) morphologies in the 100-10000 atoms range, where interatomic interactions were modelled within the framework of a second moment tight binding approximation.[29] Icosahedra resulted favourable in the 100-1000 range, followed by 5-fold twinned decahedra up to 1000-10000 atoms, after which fcc crystal truncations prevail. Intriguingly, the metal-dependent structural crossover sizes can be rationalized in terms of the "stickyness" of the potential, i.e. a measure of the interatomic potential stiffness or softness. [3] Accounting for entropic contributions at finite temperature showed that multiply twinned nanoparticles, with Ih more than Dh, are favoured at high temperatures. [30] Recent calculations also included non magic-size architectures in the systematic comparison of energetic rankings among nanoparticles with different morphologies and sites. These studies offered a novel perspective on the additional complexity associated to low-symmetry systems. While confirming the earlier presented picture, an alternance between different morphological archetypes was observed within a given favourable-structure region. This behaviour was rationalized in terms of size by size geometry dependent favourable strain relief mechanisms. [31, 32]

1.5.2 Solid-solid transitions at the nanoscale

The energetic landscape of a nanoparticle of fixed size and composition is often rough and multi-funnelled. In turn, the system presents an immanent metastability at finite temperature. Owing to thermal motion, structural rearrangements can take place among basins connected by pathways presenting energetic barriers not too large with respect to the temperature of the system. Forecasting the accessible structural fluctuations in a nanoparticle is thus fundamental to capture and possibly control through specific synthesis routes, the structural polydispersivity of a sample and, in turn, its properties. Nanoparticle architecture and chemophysical properties are indeed intimately connected through structure-property relationship.

Recently, electron beam irradiation has been employed to demonstrate a methodology which enables to obtain: i) stable populations of isomers from an array of initially metastable structures for the case of relatively large systems (Au923),[33] ii) fluctuating structures in smaller ones (Au55).[34] Ex-situ annealing experiments also allowed for the detection of structural transformations in small and medium size nanoparticles of gold.[35] The evolution of these studies enabled to determine the proportion of isomers belonging to Ih or Dh archetypes in a wide range of temperatures for the case of Au923.[36]

Numerical simulations can aid and parallel experimental imaging. Indeed they potentially yield precise and accurate information on the energetic landscape of the system and allow to single out the effects of different parameters (e.g. temperature, size, composition) on the rearrangement mechanisms driving structural transitions. Parallel to the complexity inherent to nanoparticle taxonomy, the characterization of structural rearrangements in nanoparticles is however non-trivial. Two broad families of rearrangement mechanisms can be evoked to this end. We characterize a structural rearrangement depending on whether it comprises: (A) single-atom diffusion, collective but not concerted diffusions, jumps, and exchanges steps;[37, 38] (B) diffusionless collective and concerted rearrangements, e.g., screw-dislocation motions.[39–41] This choice enables to establish a parallelism with bulk systems, with the (A) mechanisms falling into the category of diffusion-driven rearrangements or surface peeling mechanisms and (B) ones instead being the nanoscale counterpart of bulk martensitic transformations.

The extent through which collective mechanism are favourable in nanoparticles of different size and composition will be discussed in Chapters 3 and 4 for the case of mono- and bi-metallic nanoparticles respectively.

1.5.3 Phase changes at the nanoscale

Nanoparticles' surface to volume ratio is large, therefore the prediction of their stability according to thermodynamics principles must address the significant contribution of the surface terms.[42, 43] Many analytic models have been thus proposed to predict the melting temperature of nanoparticles. The first attempt is dated to the XX century, when Pawlow suggested an inverse relation between the melting temperature of a finite-size object and its size.[44] His model is based on the assumption that the chemical potential of liquid and solid nanoparticles - approximated as spheres of the same radius - will be the same. From these premises, the melting point was found to be proportional to $1/d_{np}$ where d_{np} is the nanoparticle diameter, with the bulk melting point thus recovered for systems of infinite size.

Thereafter experimental, theoretical and numerical investigations succeeded one another to further capture the complexity inherent to the melting of a nanoscale object.[42–52] Among the theories developed, the liquid nucleation and growth model is one of the most accredited. It states that melting initiates at the surface of the nanoparticle, and that the liquid layer then expands inwards.[45] Therefore, accounting for the free energy balance between the melted and the solid layers is key towards the prediction of the nanoparticle melting point. The $1/d_{np}$ dependence of the melting point is recovered also in this model, within the assumption of solid and liquid nanoparticles having the same radii. By the same token a

process peculiar of the nanoscale such as surface melting can be elegantly rationalized by accounting for the cost of nucleating a solid-liquid interface in the nanoparticle.[46]

Recently, the possible melting modes in a nanoparticle have been assessed, with size dependent melting mechanisms observed.[47] By the same token, the presence or absence of surface melting was connected to the presence of an hysteresis between the melting and the freezing point of a nanoparticle. The hysteresis appears either because of kinetic effects leading to superheated/supercooled states or due to differences inherent to the mechanisms through which solid-liquid and liquid-solid phase changes take place.[53, 52, 54] In Chapter 5 Section 5.1 we will analyse and discuss the presence of a kinetically driven hysteresis loop between the melting and freezing caloric curves for the paradigmatic case of $\text{Cu}_{162}\text{Pt}_{147}$.

Characterizing melted and solid nanoparticles Phase change temperatures for size-selected systems can be determined via numerical methods. These can thus benchmark the validity and inform the development of accurate analytic models. By the same token the atomistic detail in the characterization of melting and freezing processes, together with the strong control on the tunable parameters of interest (heating rate, system size and composition) make numerical methods a suitable tool to parallel experiments.

The identification of a phase change in small finite-size systems is however far from trivial, also for the case of *in silico* studies. On one hand the analysis of the caloric (*in silico*) and heat capacity (*in vitro* as well as *in silico*) curves is a traditional tool to quantitatively infer when a phase change takes place. [48, 51, 53, 52] While this practice is robust for systems with non degenerate solid and liquid phases energies, it may result less effective in more complex cases where, e.g., because of the presence of a strongly interacting environment surrounding the nanoparticle, features in the caloric and heat capacity curves are difficult to interpret because of the quasi-degenerate energies of solid and molten nanoparticles. [55]

Beyond looking at the system energetics, an orthogonal approach instead consists in the structural characterization of the nanoparticle architecture at different temperatures to single out changes in order parameters of interest. Heuristically, the structures of solid and liquid nanoparticles are different, however it has been challenging so far to recast this intuition into the formal definition of an order parameter (or collection of those) discriminating melted and solid structures regardless of system size and composition. The comparison of the relative abundances of atoms displaying a specific symmetry in their neighbourhood [56, 57] at different temperatures has been a common but not robust practice in numerical investigations: especially close to melting, nanoparticles display low symmetry morphologies, defected surfaces, and broadened pair distance and angular distribution functions (see e.g. [54]). The characterization of the phase change of a nanoparticle by estimating the percentage of atoms

with a chosen local order in their neighbourhood is thus negatively influenced in terms of both accuracy and precision by the above mentioned factors. Another commonly used approach was related to the calculation of cumulative time averages of the root mean bond fluctuation. This estimate is, however, affected by a non trivial determination of the convergence of this parameter to some characteristic value for melted or solid phases. Furthermore its convergence is negatively influenced by the occurrence of structural rearrangements [48]. In Chapter 5 Section 5.2 we will thus discuss how the systematic analysis of melting simulations of monometallic nanoparticles enabled to single out quantitative descriptors to determine univocally whether a nanoparticle is solid or liquid.

1.6 Nanoparticles as catalysts

The adsorption sites in a heterogeneous catalyst can be thought of as the ensemble of atoms that can bond with an adsorbate. Henceforth, the active sites will be the ones that catalyze a reaction involving the adsorbate.[58] Nanoparticles present a large number of surface adsorption site per metallic load (i.e. their surface to volume ratio is large), a good quantity of which might be potentially highly active. Thus, nanoparticles can be intuitively identified as ideal for applications in catalysis. Indeed engineering the largest possible amount of active adsorption sites per gram of metal in a catalyst is a paradigm to reduce the cost of a catalyst.

Furthermore, finite-size and electronic effects lead to unique catalytic properties, e.g. nanoparticles made of an highly inert bulk metal as Au, may result strongly active towards a given reaction.[59] Moreover miniaturization at the nanoscale may lead to the formation of adsorption sites whose topology or local strain are unique of low dimensional objects, hence enabling to overcome some of the intrinsic limitations in the chemistry of extended surfaces.[60] From these premises, it is thus clear that the architecture of a nanoparticle (morphology, size, and composition) determines its catalytic properties.

From simple chemical intuition, the local environment of each adsorption site in a nanoparticle affects the interaction strength with the adsorbate, with low coordinated atoms bonding with molecules more strongly (especially true for small molecules where complex effects, such as steric ones, are not present). Following from the Sabatier principle - stating that for a reaction to take place the adsorbate should bond nor too weakly nor too strongly - the adsorption energy is a good descriptor of the activity of an adsorption site.[61] In turn, the site coordination was often invoked as a surrogate descriptor of the adsorption energy, thus bypassing the need of electronic structure calculations to forecast the activity of a given site.[62, 63]

Beyond the success of counting-site methods in rationalizing size-dependent trends in the mass and specific activity of nanoparticles, the link between coordination and adsorption properties was only recently formalized for the case of the intermediates of oxygen reduction reaction and carbon dioxide reduction reaction, catalysed by mono- and bi-metallic nanoparticles, both in the gas phase and supported. [64–67, 9, 68, 69]

Rationalizing the catalytic properties of nanoparticles in terms of shape, size, and chemical composition contribution leads to: i) the clarification of the debate in the literature regarding mass-activity peaks for target systems employed to catalyze a given reaction; ii) the development of rational design criteria for the synthesis of better performing nanocatalysts, through the identification of the ideal structural features to be implemented in a nanoparticle. In this view, the synthesis of rationally designed nanoparticles that drive more efficient and selective reactions may trigger a revolution in the green economy, e.g. making fuel-cells economically viable against combustion engines, or opening the path towards a zero-emission energy conversion cycle in the making of fuels and base chemicals. In Chapter 6, we will discuss how enumerating the kind and occurrence of non equivalent sites on a nanoparticle according to an appropriate geometrical descriptor linking topological to catalytic properties allows for the fast and accurate prediction of the nanoparticle's ability in catalyzing a target reaction. The nanoparticle's catalytic properties will be estimated in terms of a macroscopic observable: the current produced during, e.g., the electrochemical reduction of oxygen. In turn, this calculations will be exploited to establish design principles towards the synthesis of high-performance Pt nanoparticles for catalysing oxygen reduction reaction.

Chapter 2

Numerical Methods

Simulation results reported and discussed in this work have been carried on using the "Low Dimensional System" package, LoDiS, the family of softwares I helped to develop towards the bespoke study of structural and catalytic properties of nanoparticles in silico.

The core of the LoDiS package is a Molecular Dynamics (MD) suite. MD allows for the sampling of the energetic landscape and dynamical evolution of nanoparticles in different ensembles (see also Section 2.1) and conditions (Section 2.2). The observed configurations can be thus analysed to characterize:

- Nanoparticle structure (Section 2.4 and Section 2.5 and Section 2.6).
- Nanoparticle catalytic properties (Section 2.6 and Section 2.7).
- Nanoparticle structural rearrangement mechanisms (Section 2.8).

When other techniques are coupled to molecular dynamics, a more varied set of information about the interplay of kinetic, entropic, and energetic contributions in determining the structures of a nanoparticle can be obtained. In turn these enable to address:

- Nanoparticles' structural stability against pre-melting (Section 2.9).
- Nanoparticles' structural stability against melting (Section 2.9).
- Nanoparticles' formation during a one-by-one process.
- Nanoparticles' formation during simulated annealing.

In the rest of the chapter the technical details related to each technique relevant to the results of this work will be discussed.

2.1 Molecular dynamics

Molecular Dynamics is a method to study the time evolution of a system from initial conditions by integrating Newton's equation of motion through a finite difference algorithm. A correct integration time interval encodes full information on the faster degrees of motion in the systems (i.e. the fastest vibrational frequencies of the bond between the lighter atoms in the system). For the case of metallic systems modelled classically, an appropriate time step is 5 fs.[25] Molecular Dynamics allows to sample the different stastical ensembles. While in LoDis both NVE and NVT ensembles can be sampled, only results within the latter will be reported here. Molecular Dynamics has been in fact used to sample a portion of the phase space of the systems of interest in relation to their temperature, the free energy barriers inherent to structural rearrangements of the initial structure, and the observation time (i.e. the simulation time). Meaningful statistical investigations through Molecular dynamics runs are based upon data gathered from a large number of trajectories and event. Non ergodic observations may in fact result in an unfaithful description of the properties of the system under investigation.[70] The number of simulations performed for each study addressed in this thesis was tailored to obtain valid statistics with respect to the complexity of the investigation itself and will be discussed case by case.

Velocity-Verlet integration To integrate Newton's equation of motion a velocity-Verlet algorithm is exploited in LoDiS. In this numerical procedure positions and velocities are calculated throughout a Taylor expansion, as reported in Equation 2.1 : [71]

$$\begin{aligned} r(t + \delta t) &= r(t) + v(t)\delta t + \frac{f(t)}{2m}\delta t^2 + \mathcal{O}(\delta t^4) \\ v(t + \delta t) &= v(t) + \frac{f(t) + f(t + \delta t)}{2m}\delta t^2 + \mathcal{O}(\delta t^2) . \end{aligned} \quad (2.1)$$

The calculation of position, velocities, and forces thus proceeds in two steps: first velocities at the half time-step are evaluated by integration of forces given positions at time t , then positions are updated at full step, using the just calculated velocities at half-step. The velocity-Verlet is chosen because of its robust properties: it is energy-conserving, time reversible, and order four (two) errors are committed on positions (velocities).

Andersen Thermostat The Andersen thermostat is used to mimic the interaction of the system with a stochastic bath that allows the temperature of the system to fluctuate around a selected temperature through virtual instantaneous interactions. It replaces the momentum of randomly selected atoms with a new one drawn from a Maxwell-Boltzmann distribution

at the chosen temperature. In the time from one stochastic collisions to the next one, the system evolves at constant energy obeying Newton's equations of motion. The time elapsed between two interactions follows a Poisson distribution, that is, being ν the frequency of the interactions, the distribution $P(\nu, t)$ of the t the elapsed time between two interactions takes the form:

$$P(\nu, t) = \nu e^{-\nu t} . \quad (2.2)$$

The strength of the coupling to the bath is determined by the thermostat frequency, which satisfies two opposite needs: it is high enough to ensure an efficient temperature control, but also not so large that the diffusive properties of the atoms in the system result too altered.[72]

2.2 Interatomic potentials

Investigation by means of in silico experiments are constrained by a trade-off between accuracy and computational expense in the treatment of the interactions between the components in the system. In this section we detail the different interatomic potentials employed (Subsection 2.2.1) and recently implemented (Subsections 2.2.2, 2.2.4, 2.2.3) in LoDiS to investigate the structural stability of nanoparticles in different conditions.

2.2.1 Second-moment approximation tight-binding potentials

Potentials derived in the framework of the second moment tight binding approximation established as reliable and efficient in the study of transition metal systems with size between tens and thousands of atoms. The Gupta or Rosato-Guillopie-Legrande[73] formulation belongs to this family of potentials. It consists of a repulsive and an attractive term. The first is well approximated by a Born-Meyer term, the latter by a many-body term derived according to the second moment tight binding approximation framework. The aforementioned approximation is well suited for transition metals given the strong d character of their valence states. The interaction potential, $V_{TBSMA}(rij)$, depends on the set of all atomic coordinates r_{ij} and is the sum of atomic contributions E_{TBSMA}^I , evaluated as

$$V_{TBSMA} = \sum_i^N E_{TBSMA}^i , \quad (2.3)$$

$$E_{TBSMA}^i = \sum_{j \neq i}^{n_v} A_{ab} e^{-p_{ab} \left(\frac{r_{ij}}{r_{ab}^0} - 1 \right)} - \sqrt{\sum_{j \neq i}^{n_v} \xi_{ab}^2 e^{-2q_{ab} \left(\frac{r_{ij}}{r_{ab}^0} - 1 \right)}} . \quad (2.4)$$

Table 2.1 Resume' of the Rosato-Guillopo-Legrande potentials parametrizations used in the systems investigated in this work.

M-M	A (eV)	p	q	ξ (eV)
Ni-Ni [74]	0.103	10.85	3.18	1.19
Pd-Pd [74]	0.175	10.87	4.00	1.71
Pt-Pt [74]	0.274	10.71	3.84	2.62
Cu-Cu [74]	0.089	10.55	2.43	1.28
Ag-Ag [74]	0.103	10.85	3.18	1.19
Au-Au [75]	0.206	10.23	4.03	1.79
Pt-Cu [53]	0.161	10.79	3.14	1.82
Pt-Ag [76]	0.175	10.73	3.59	1.79
Cu-Ag [77]	0.098	10.70	2.81	1.23
Au-Ag [75]	0.154	10.58	3.59	1.48

The sum runs up to the number of atoms n_v within an appropriate cut-off distance from atom i , a and b refer to the chemical species of the two atoms, r_0^{ab} is the bulk nearest neighbour distance for the homometallic atomic pairs and their arithmetical average for the bimetallic case. A_{ab} and ξ_{ab} fit the cohesive energy, while p_{ab} and q_{ab} do so for the stiffness of the potential. Parametrization in the case of homo-atomic and hetero-atomic interactions have been gathered from the literature and are reported in Table 2.1.

2.2.2 Non-parametric metal-metal interaction potentials

Machine learning algorithms, either within the framework of bayesian regression or neural networks, present the opportunity to develop non-parametric two- or three-body force-fields as accurate as electronic structure calculations and as fast as semi-empirical force-fields of the same interaction order.[78] As part of the PhD, I contributed to the production and testing of a non-parametric machine learning force-field for a Nickel cluster of 19 atoms.[79] The interested reader is referred to Appendix, Section A for a detailed discussion of this work.

Briefly, the generation of a non-parametric force-field is achieved by first calculating the two- and three-body contributions to energy and forces from triplet and atom pairs in a training database exploiting e.g., bayesian regression. Energy for configurations outside the training set can be thus calculated through spline interpolation over the stored machine learning predictions. Analytic differentiation of the spline expression produces an energy conserving force-field practically indistinguishable from the predictions of the 3-body gaussian process used to build it, but independent of the number of configurations used for training.[80]

2.2.3 Implicit metal-support interaction potential

Interaction with a support may play a significant role in determining the (meta)stability of a metallic nanoparticles, thus, I took part in the implementation of metal-oxide implicit force-field in LoDiS. Metal-oxide interaction can be modelled implicitly via a double Morse potential coupled to an expansion of the symmetries underlined in the substrate. This approach captures preferential binding to the inequivalent sites while ensuring small computational expenses. The implicit nature of the formulation obliges to neglect the possible thermal dependent corrugation of the substrate. Following the Vervisch-Mottet-Goniakowski formulation [81] the metal substrate interaction energy, E^{M-S} can be recast in terms of the distance between the atom and the substrate, z , weighted by parameters a , where the number of metallic nearest neighbours within the cluster is imposed to be less than 12. The $a_{i,\alpha}$ coefficients encode both the information on the metallic coordination CN_i and the substrate geometry with respect to x_i and y_i coordinates of atom i to the substrate itself:

$$E_i^{M-S}(x, y, z) = a_1(x, y, z)e^{-2a_2(x, y, z)(z-a_3(x, y, z))} - 2e^{a_2(x, y, z)(z-a_3(x, y, z))}, \quad (2.5)$$

where a_i are parameters dependent on coordination number, CN_i of the atom weighted by other parameters b_{ij}

$$a_i(x, y, z) = b_{i1}(x, y) + b_{i2}(x, y)e^{-CN_i/b_{i3}(x, y)}. \quad (2.6)$$

The metallic coordination CN_i is calculated via a continuous and smooth function for avoiding any discontinuity [82]:

$$CN_i = \sum_{j \neq i} \frac{1}{1 + e^{m\left(\frac{r_{ij}}{r_c} - 1\right)}}, \quad (2.7)$$

where the cut-off radius, r_c , and the exponent, m , tuning the smoothness of the Fermi function, are additional parameters to be fitted. The b_{ij} parameters instead depend on the parameters c_{ijk} weighted by trigonometric functions which ensure the periodicity and symmetry underlined in the substrate geometry, such that for a double square geometry, as in the case of MgO(100) surfaces:

$$b_{ij}(x, y) = c_{1ij} + c_{2ij} \left(\cos\left(\frac{2\pi x}{a}\right) + \cos\left(\frac{2\pi y}{a}\right) \right) + c_{3ij} \left(\cos\left(\frac{2\pi(x+y)}{a}\right) + \cos\left(\frac{2\pi(x-y)}{a}\right) \right). \quad (2.8)$$

The Pt-MgO(100) interactions are thus reproduced by the Vervisch-Mottet-Goniakowski potential after the fitting of the 27 parameters $c_{\alpha,\beta,\gamma}$, on top of r_c and m against DFT calculations (see [83]). A dimensional analysis demonstrates that $c_{\alpha,\beta,\gamma}$ are dimensionless

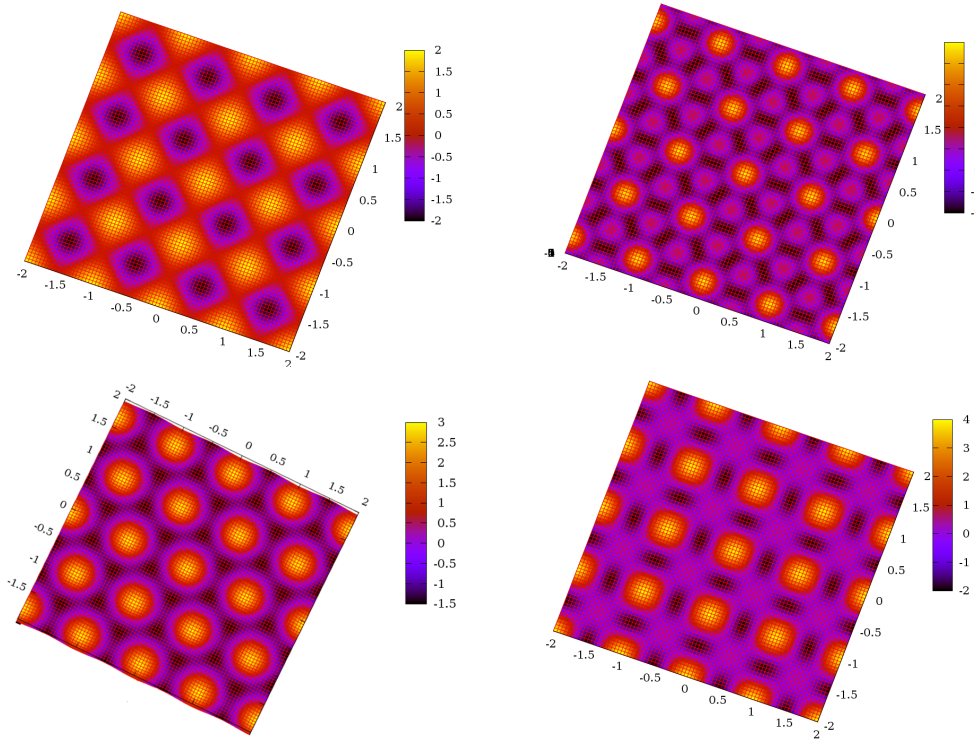


Figure 2.1 Lattice corrugation implicit in Equations 2.9 (top-left), 2.10 (top-right), 2.11 (bottom-left), 2.12 (bottom-right), to calculate the b_{ij} coefficients (Equation 2.8).

and tune the screening related to the metallic coordination of atom i . $c_{1,1,\gamma}$ and $c_{1,2,\gamma}$ determine the strength of the interaction, while $c_{3,1,\gamma}$, $c_{3,2,\gamma}$ are in \AA and control the interaction range between the nanoparticle and the support. $c_{2,1,\gamma}$ and $c_{2,2,\gamma}$, $1/\text{\AA}$ units, tune the screening of the support interaction. Coefficients with $\gamma = 2, 3$ allow to sculpt the lateral contributions from the substrate. The implementation of this potential in LoDiS resulted from the joint effort between people in Dr. Baletto's group.

Other trigonometric functions have been tested to introduce the possibility of simulating nanoparticles deposited on substrates presenting a surface with other corrugations (Figure 2.1), such as a square lattice (Equation 2.9), a triangular (Equation 2.10), or a honeycomb one (Equation 2.11). The combination of trigonometric function leading to such patterns is, respectively:

$$\text{square} = \cos(2\pi x) + \cos(2\pi y) \quad (2.9)$$

$$\begin{aligned} \text{triangle} = & \cos(2\pi(x + y/\sqrt{3})) + \cos(2\pi(x - y/\sqrt{3})) + \cos(4\pi(y/\sqrt{3})) + \\ & \cos(2\pi(x + y\sqrt{3})) + \cos(2\pi(x - y\sqrt{3})) + \cos(4\pi(x)) \end{aligned} \quad (2.10)$$

$$\begin{aligned}
\text{honeycomb} = & \cos(2\pi(x + y/\sqrt{3})) + \cos(2\pi(x - y/\sqrt{3})) + \cos(4\pi(y/\sqrt{3})) + \\
& \cos(2\pi(x + y\sqrt{3})) + \cos(2\pi(x - y\sqrt{3})) + \cos(4\pi(x)) + \\
& \cos(2\pi((x) + y/\sqrt{3})) + \cos(2\pi((x) - y/\sqrt{3})) + \cos(4\pi(y/\sqrt{3})) + \\
& \cos(2\pi((x) + y\sqrt{3})) + \cos(2\pi((x) - y\sqrt{3})) + \cos(4\pi((x)))
\end{aligned} \tag{2.11}$$

where the double square lattice corrugation, for reference, is:

$$\text{double square} = \cos(2\pi x) + \cos(2\pi y) + \cos(2\pi(x + y)) + \cos(2\pi(x - y)) \tag{2.12}$$

This extension of the Vervisch-Mottet-Goniakowski formulation was initiated together with Mr. Norbert Zicher during his summer undergraduate research fellowship and is still under development.

2.2.4 Implicit metal-environment interactions potential

Similar to the case of a strongly interacting support, the energetic landscape of metallic nanoparticles in a non inert environment can greatly vary from the one of their vacuum counterparts. Hence, I adapted and developed in LoDiS the treatment of metal-environment interactions according to an implicit force-field, where metal-environment interactions are recast in terms of single atoms contributions dependent on their coordination CN_i . According to the Huerto-Cortes, Goniakowski, Noguera formalism [55] the energetic contributions of a metallic nanocluster interacting with a non inert-environment, E_i^{M-E} , results equal to the number of absent bonds with respect to the bulk configuration, $CN_{open} = CN_{bulk} - CN_i$, weighted by two parameters, ε and ρ :

$$E_i^{M-E} = -\varepsilon CN_{open}^\rho \quad , \tag{2.13}$$

where CN_i is calculated according to equation 2.7, and CN_{bulk} equals to 12 for the case of fcc metals. In this framework, the interaction nature between the surface sites and the environment is captured by the ρ parameter, which takes a value of 1 for pairwise interaction, less than one for covalent like, and more than one for strongly interacting environments. The ε parameter instead is fitted to reproduce the interaction strength of interest. Different ρ and ε parameters set the ratio between the surface energies of low Miller index terminations, thus introducing a tunable parameter to favour an architecture or another.

2.3 Energetic characterization

To compare energetic rankings among systems with different nuclearities and chemical compositions, it is useful to introduce here a quantity which normalizes the energetic contributions with respect to nanoparticle size and stoichiometry. To this end we use the excess energy Δ : [3]

$$\Delta = (E_{\text{tot}} - NE_{\text{coh}})/N^{2/3} \quad , \quad (2.14)$$

where E_{coh} is the cohesive energy of the metal in the bulk and N the number of atoms in the nanoparticle. By definition Δ is 0 for the case of bulk systems in their equilibrium position and positive otherwise. Its formulation is particularly suited for the case of nanoparticles because of the $N^{2/3}$ normalization factor which accounts for surface to volume contributions in systems of different sizes, allowing to treat them on the same footing.

2.4 Structural characterization

Because of the many morphologies a nanoparticle can assume, it is of fundamental importance but highly challenging, to develop a framework which allows for an efficient and accurate structural characterization of any configuration. Beyond the use of big data techniques, currently under development also in the LoDiS suite, several global and local order parameters have been defined and/or implemented towards this end.

2.4.1 Nanocluster giant Icosahedron mapping

The simplest framework to classify a nanoparticle configuration hinges on recognizing the presence and mutual arrangement of atoms presenting characteristic symmetries in their neighbourhood (see. e.g. subsection 2.5.2 or reference [57]). In particular, we classify nanoparticles structures according to whether they belong to any of the following three morphological families:

- Closed packed (Cp): nanoparticles formed only by stacked close-packed layers. All morphologies deriving by a cut of a fcc or hcp lattice, e.g., the octahedron and its truncations, belong to this class.
- Decahedra (Dh): nanoparticles presenting a single five-fold symmetry axis. We note that this structural feature may not necessarily intersect the center of mass of the nanoparticles. Marks- and Ino- decahedra are notable example of motifs which belong to this class.

- Icosahedra (Ih): nanoparticles displaying more than one five-fold symmetry axes, which intersect in one or more points. We remark that this intersection may lie off-centre, or even outside the cluster itself. Nanoparticles constituted by many tetrahedral units, like the closed-shell icosahedra or poly-icosahedra, belong to this class.

The chosen characterization method offers the possibility to readily visualize the morphologies by mapping the nanoparticles motifs in reference to a much larger closed-shell icosahedron, referred here as giant icosahedron (gIh), as shown in Figure 2.2.[83] A graphical visualization consists of a 2D-projection, where the dashed lines represent the five-fold symmetry axes of the gIh upper half while the nanoparticles - examples in Figure 2.2 C - are drawn as a circle with diameter corresponding to the maximum pair distance in the cluster. The circles positions on the 2D gIh (Figure 2.2 B) are determined from the relative arrangement of the center of mass of the nanoparticle, and the icosahedral center or the five-fold axis, if any. A circle corresponding to an Ih is positioned by using the distance between its center-of-mass and the closest icosahedral atom - either truly present in the cluster or at the intersection of the five-fold axes - and aligning the longest five-fold axis of the cluster to one of the gIh. For Dh, the circle is located so that the distance between its center and the gIh five-fold axis approximates the one between the nanoparticle center-of-mass and its own five-fold axis. The gIh size is lower bounded by the smallest size where the three above listed morphological classes can be univocally distinguished, by a well-defined region of the gIh, as identified by a different colour in Figure 2.2.

The gIh mapping is particularly suited for the characterization of low symmetry structures, for which reference values for the other order parameters discussed in the rest of the section (pair distance distribution functions, coordination based genomes, as well as CNA signature distributions) are not known.

2.4.2 Pair distance distribution function

The Pair Distance Distribution Function (PDF) gathers the distribution of the distances between each pair of atoms in the cluster. It can be assumed to be a faithful and unique structural descriptor in the case of monometallic nanoparticles.[79, 84–86] Indeed, the PDF of a nanoparticle can be fingerprinted through spectroscopy experiments.

The PDF, assuming a discrete distribution of distances in the nanoparticle, results:

$$g(d) = \frac{1}{(N)(N-1)} \sum_i^N \sum_{j \neq i}^N \delta'(r_{ij} - d) \quad , \quad (2.15)$$

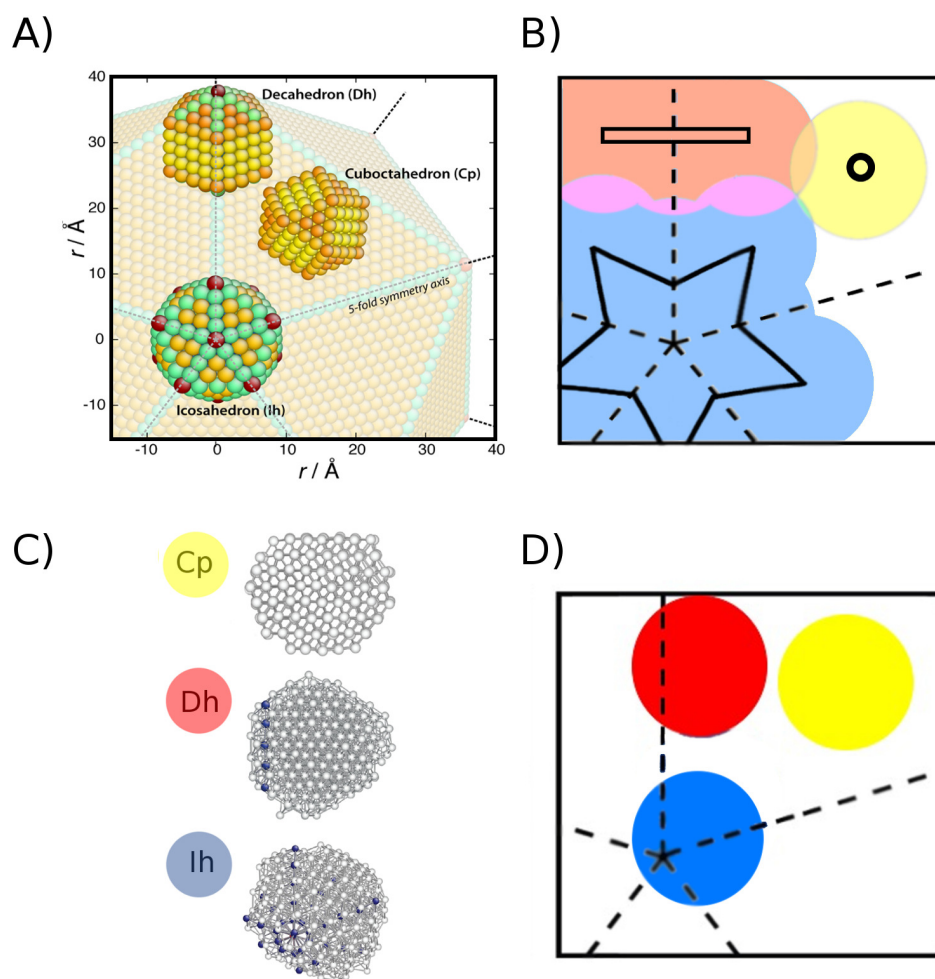


Figure 2.2 (A) Visual mapping of a 309 atoms closed-shell polyhedra into a 37995-atoms giant Ih. Though the solid angles are inherently different from the exact values of the ones in a perfect polyhedron, a smaller icosahedron can be readily placed in the innermost shells of a larger one; a decahedron can be formed from a section of an icosahedron along one 5-fold symmetry axis; a crystalline structure from the close-packed tetrahedral space between the gIh five-fold boundaries. (B) 2D-projection of the g-Ih where the coloured regions label the three morphological families where a nanoparticle, represented by a circle, can be placed. Circles might overlap, as in the pink, orange, and green regions. The classification is however univocal, as the position of the center of circle lies in well distinguished regions. The centre of Dh falls in the red rectangle, the Cp's one in the yellow circle, and the Ih's centre within the blue star. (C) Example of low-symmetry nanoparticles where atoms belonging to a five-fold axis are in blue, icosahedral centre in red, and otherwise in white. (D) Nanoparticles in (C) representation onto the 2D-gIh map. Reproduced under CC BY license from Thermodynamics of CuPt nanoalloys - K. Rossi, L. Bartok-Pártay, G. Csanyi, F. Baletto, Scientific reports 8, 2018.

where N is the number of atoms in the system, r_{ij} is the distance between an atom i and atom j and d is the distance length probed, with δ' defining the width of the distance bin itself:

$$\delta' = \begin{cases} 1 & \text{if } d - \varepsilon \leq r_{ij} \leq d + \varepsilon, \\ 0 & \text{otherwise} \end{cases} \quad (2.16)$$

The PDF numerical resolution is dictated by the choice of the distance according to which two atomic distance are parsed into the different distance bins, i.e. 2ε , the width of the δ' function in Equation 2.15. This choice needs to balance between a too high resolution - where each distance would present a singular occurrence, hence the PDF yielding no useful information - and a too large one - where different neighbour shells are projected onto the same distance width, conversely resulting in a too coarse description.

To clarify this argument the pair distance distribution functions of an Ih Pt nanoparticle of 147 atoms at 300 K for different binning resolutions are reported in Figure 2.3. A bin width larger than 0.5 Å yields unfaithful results, e.g., the second nearest neighbour peak becomes not distinguishable for the choice of larger bin widths.

When rescaling the pair distances with respect to the metal bulk lattice constant, the PDF first peak falls close to the fcc nearest neighbours distance ($\sqrt{2}/2$). Similarly, the second peak falls close to the bulk lattice constant (1). The others are instead dependent on the geometry of the cluster. An illustrative example of the pair distance distribution functions of Ih, Dh, Co geometries of an Pt nanoparticle of 147 atoms at 300 K are reported in Figure 2.4.

The PDF analysis may become rather inefficient when a large amount of data needs to be processed. The Kullback-Leibler divergence between the pair distribution functions of two structures offers a ground to provide an asymmetric estimate of the degree by which two PDFs encode mutual information one with respect to the other.

$$KL(P | Q) = \sum_i P(i) \log \frac{P(i)}{Q(i)}. \quad (2.17)$$

Commonly used in information theory, the Kullback-Leibler divergence $KL(P | Q)$ establishes a quantification of the amount of information lost when a function Q is used to approximate another function P , hence it is also known as the cross-entropy. It takes values of 0 if P and Q are equal and increases the more Q cannot approximate well P . Indeed $KL(P | Q)$ can also diverge if $Q(i) = 0$ and $P(i) \neq 0$. To avoid the calculation of possibly divergent quantities, $P(i) + Q(i)$ instead of $Q(i)$ can be used to calculate cross-entropy estimates via Equation 2.17.

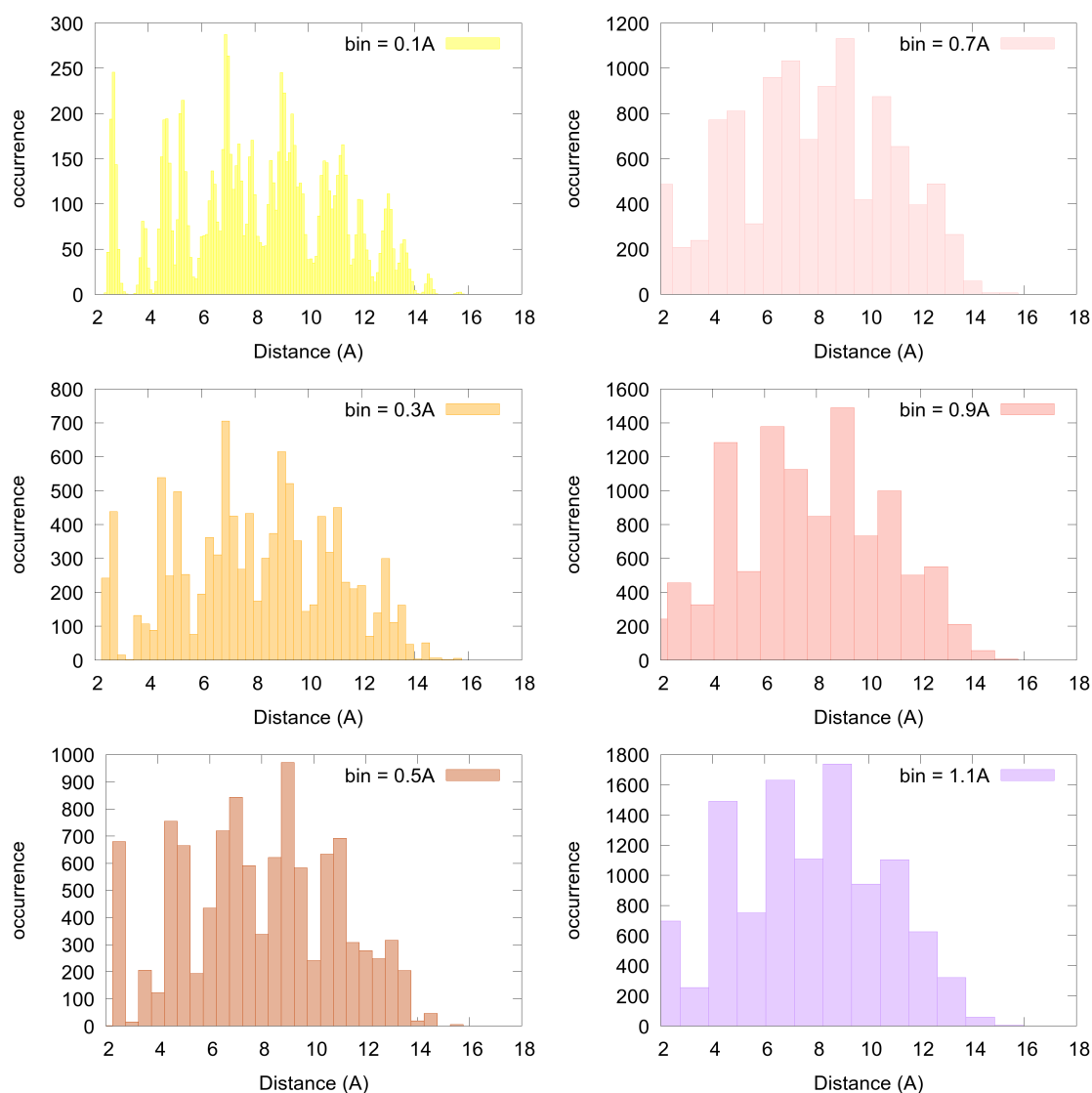


Figure 2.3 Histograms for the pair distribution functions of Pt nanoparticles of 147 atoms at 300K presenting an Ih morphology for different bin width, reported in the top right corner of each subfigure. Colour coding is also used to discriminate the different PDFs.

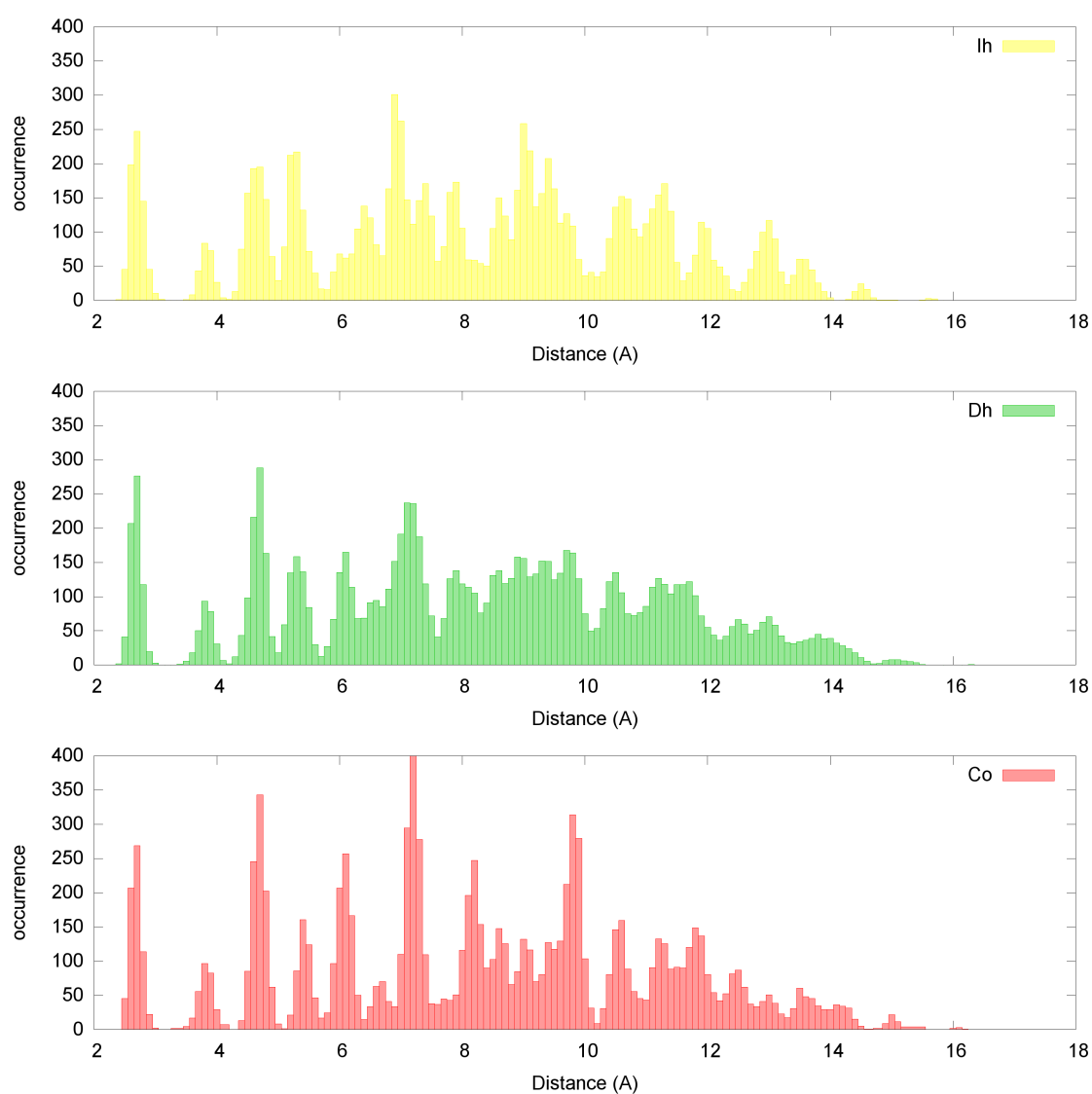


Figure 2.4 Histograms for the pair distribution function of Ag nanoparticles of 147 atoms at 300K presenting a Co (in red), Dh (in green), or Ih (in yellow) morphology.

2.4.3 Radial distribution function

An alternative to characterize the structure of a system is given by the radial distribution function (RDF), i.e. the measure of the change in the density of atoms from the center of mass of the nanoparticle. The coordinates of the latter are calculated as

$$d_{c.o.m}^x = \frac{\sum_i^N x^i}{N} \quad d_{c.o.m}^y = \frac{\sum_i^N y^i}{N} \quad d_{c.o.m}^z = \frac{\sum_i^N z^i}{N} \quad (2.18)$$

where i labels the atoms in the nanoparticles, amounting for a total of N , with x^i, y^i, z^i being their cartesian coordinates. We note that the $d_{c.o.m}$ coordinates may not necessarily be centered on the same position of an atom in the nanoparticle. In turn, the RDF is calculated by counting the occurrence of atoms i , positioned in $r_i = (x_i, y_i, z_i)$, within the volume limited by concentric spheres of constantly increasing radii and center coinciding with the center of mass, $d_{c.o.m}$, of the nanoparticle:

$$g(d)_{radial} = \sum_i^N \delta'[(r_i - d_{c.o.m}) - d] \quad (2.19)$$

where

$$\delta' = \begin{cases} 1 & \text{if } d - \varepsilon \leq r_i - d_{c.o.m} \leq d + \varepsilon, \\ 0 & \text{otherwise} \end{cases} \quad (2.20)$$

Chemical radial distribution function The comparison of chemically informed RDFs in a nanoalloy allows for a ready description of its chemical ordering: when the radial distribution functions of chemical species A and B overlap, a mixed or a Janus nanoparticle is observed, when layers are significantly occupied by only one-element, core-shell or multi-shell arrangements are observed, depending on whether one or more shared interfaces are detected. The calculation of the chemical RDF naturally follows from equation 2.19:

$$g(d)_{radial}^A = \sum_{i \in A}^N \delta'[(r_i - d_{c.o.m}) - d] \quad (2.21)$$

$$g(d)_{radial}^B = \sum_{i \in B}^N \delta'[(r_i - d_{c.o.m}) - d] \quad (2.22)$$

Chemistry informed radius of gyration To facilitate the analysis of the radial distribution function, one can refer to the radius of gyration of a nanoparticle, i.e. the measure of the extent by which atoms in the system are spread out away of the center of mass $r_{c.o.m.}$ of the nanoparticles.

$$G^2 = \frac{1}{N} \sum_{i=1}^N (r_i - d_{c.o.m})^2 . \quad (2.23)$$

Conversely, contrasting the radius of gyration of the two A and B chemical species present in a bimetallic nanoalloy,

$$G^A = \sqrt{\frac{1}{N} \sum_{i \in A}^N (r_i - d_{c.o.m})^2} , \quad (2.24)$$

$$G^B = \sqrt{\frac{1}{N} \sum_{i \in B}^N (r_i - d_{c.o.m})^2} , \quad (2.25)$$

will yield precise information on the chemical ordering of the nanoparticle itself: similar radii of gyration for the two chemical species will be observed for mixed or Janus ordering, while shelled-structures will be characterized by $G(r)^A$ and $G(r)^B$ of markedly different values.

Height distribution function For the case of supported nanoparticles, the presence of a substrate induces a symmetry breaking in the system. In turn, not only the radial distribution function but also the height distribution function can provide useful information about the structure of the nanoparticle. Its calculation proceeds according to the following equation:

$$g(z)_{height} = \sum_i^N \delta'(z_i - z) , \quad (2.26)$$

where the z axis is defined as the one perpendicular to the substrate and

$$\delta' = \begin{cases} 1 & \text{if } z - \varepsilon \leq z_i \leq z + \varepsilon , \\ 0 & \text{otherwise.} \end{cases} \quad (2.27)$$

2.5 Coordination distributions

Beyond the use of global descriptors, cataloguing local order parameters can aid in the characterization of the structural as well as catalytic properties of a nanoparticle. By the term local order parameter we here refer to the quantitative characterization of the symmetry and/or connectivity of local atomic environments.

2.5.1 Nominal coordination number

The simplest approach to characterize the local environment of an atom consists in counting the number of its nearest neighbours.

The easiest way to accomplish this goal is to consider a cut-off region, described by a sphere with radius equal to the bulk nearest neighbour distance and centered around the atom, and enumerate the other atoms that fall in such region.

$$CN_{tot} = \sum_{i,j} f(r_{ij}), \quad (2.28)$$

$$f(r_{ij}) = \begin{cases} 1 & \text{if } r_{ij} \leq d_0, \\ 0 & \text{if } r_{ij} > d_0, \end{cases} \quad (2.29)$$

Often it is however preferable to introduce analytic quantities for numerical reason. E.g. in subsections 2.2.3 and 2.2.4 it is shown how the interactions of atoms in a nanoparticle with a rigid support or an implicit environment can be expressed as function of their coordination. In turn, only if the latter is calculated according to an analytic function a smooth potential energy surface will be obtained. An alternative but equivalent formulation with respect to the one of Equation 2.7 has been also coded in LoDiS. Let d_0 be the nearest neighbour bulk reference distance, r_0 as the distance related to the width of the descending branch of a sigmoid function f , and n and m as the powers used to tune smoothness and asymptotic behaviour of the analytic function f (here set to 6 and 12 respectively), the total coordination number of atom, CN_{tot} , results

$$CN_{tot} = \sum_{i,j} f(r_{ij}), \quad (2.30)$$

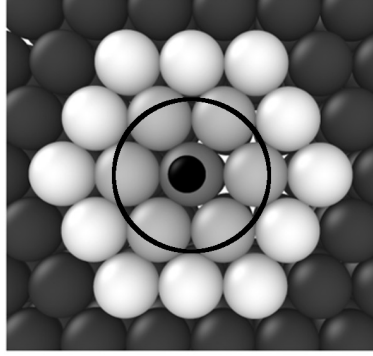


Figure 2.5 Atoms accounted for when calculating the nominal coordination of the central atom in dark shadowing. First nearest neighbour shell is delimited by a black circle.

$$f(r_{ij}) = \begin{cases} 1 & \text{if } r_{ij} \leq d_0, \\ 1 - \left(\frac{r_{ij} - d_0}{r_0} \right)^n & \text{if } r_{ij} > d_0, \end{cases} \quad (2.31)$$

The choice of the cut-off distance d_0 is not necessarily trivial. While it is tempting to take d_0 equal to the bulk nearest neighbour distance, this choice may not be robust enough against thermally driven first nearest neighbour bond elongations. Heuristically it was observed that taking a 20% threshold above this value ensures results relatively robust (especially at temperatures below the melting) to both the latter mentioned bond elongations, as well as second nearest neighbour bonds contractions. Exclusion procedures [87] or effective coordination [88] counting can be invoked in the cases where even more robust order parameters are needed.

Chemistry informed coordination number To characterize the chemical ordering of nanoalloys made of two chemical species A and B, it is further helpful to introduce chemically informed coordination numbers.

$$CN_{AA} = \sum_{i,j \in A} f(r_{ij}), \quad (2.32)$$

$$CN_{BB} = \sum_{i,j \in B} f(r_{ij}), \quad (2.33)$$

$$CN_{AB} = \sum_{\text{species}_i \neq \text{species}_j} f(r_{ij}), \quad (2.34)$$

Mixing Parameter The mixing parameter μ , thus measures the degree of alloying in a nanoparticle as a function of the specialized coordination numbers previously introduced:

$$\mu = \frac{CN_{AA} + CN_{BB} - CN_{AB}}{CN_{AA} + CN_{BB} + CN_{AB}}. \quad (2.35)$$

This quantity takes a value of 1 for fully mixed systems, -1 for fully segregated phases and between 0.2 and 0.5 for ordered and multi-shelled systems.[89]

2.5.2 Common neighbour signatures distributions

Having determined the connectivity networks among atoms in the nanoparticle, more complex characterization procedures can be introduced. Among these, common neighbour analysis, CNA, is one of the most established.[56] CNA characterizes pair of nearest neighbours depending on the local connectivity of their shared neighbours. Let i and j be a pair of atoms, they will be characterized by a three integers signature (r, s, t) , with r being the number of common nearest neighbours of the pair, s the number of bonds between the r atoms, and t the length of longest chain among them. Features in the signatures characterize different environments, e.g., whether a pair is in a face centred cubic environment (4,2,1), on a 5-fold symmetry axis (5,5,5), along a grain boundary (4,2,2), in the bulk or on the surface/subsurface ($r < 3$), on a (111) or (100) facet, respectively (3,2,2) and (3,1,1), in correspondence of defects or steps (2,0,0).

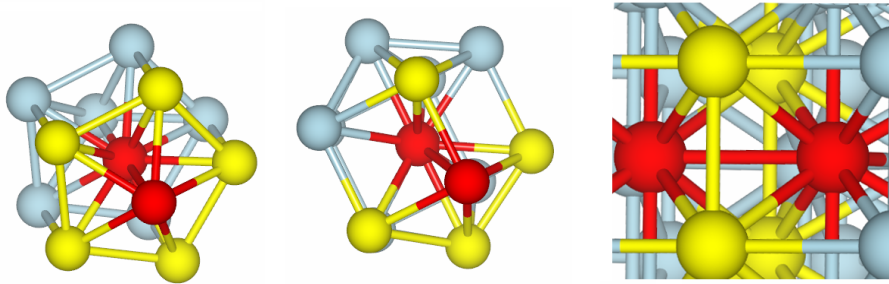


Figure 2.6 Examples of atoms pairs presenting (5,5,5), (4,2,2), or (4,2,1) common neighbour analysis signatures. The reference nearest neighbour pair is shown in red, their common neighbours are depicted in yellow.

2.6 Nanogenomics and nanoparticles catalytic properties

As mentioned in Section 1.6, rational design of nanoparticles for target applications in catalysis hinges on the understanding of the catalytic properties of each adsorption site in the nanoparticles themselves. A structural characterization analysis which encodes the mapping of catalytic properties into structural ones can thus drive the search of ideally performing nanoparticles architectures. In analogy to genetics, let's consider each nanoparticle non equivalent adsorption site (NEAS) as a gene, characterized by a unique tag, e.g. the value of some geometrical descriptor (GD) which univocally discriminates it from the other non-equivalent adsorption sites. Conversely, the collection of all the *kind* of NEAS a nanoparticle shows will be the "nanoparticle fingerprint". In turn, the "nanoparticle genome" will collect the full catalogue of the adsorption sites it presents, together with their occurrence, $\Omega(GD)$. The choice of this vocabulary is more significant than drawing a rethoric parallelism between bio-genomics and *nanogenomics*: information on the nanoparticle catalytic properties can indeed be predicted from their geometrical genome for the case of a GD which univocally maps the electronic and topological properties of the adsorption sites.

For the case of electrochemical reduction of oxygen and carbon dioxide it was demonstrated that such a geometrical descriptor exists, i.e. the generalized coordination number of the adsorption site. [64–67, 9, 68, 69] The generalized coordination of a set of atoms i , GCN_i , is calculated as the sum over the coordination number CN_j of their j neighbours, normalized with respect to the set of atoms bulk coordination:

$$GCN_i = \sum_j \frac{CN_j}{CN_{bulk}} . \quad (2.36)$$

Remarkably, the GCN formalism is not only suited for the case of single atoms, $CN_{bulk}=12$, but also transferable to count the coordination of bridge, $CN_{max}=18$, as well as hollow, $CN_{max}=24$) sites. CN_{max} values for the latter cases correspond to the total number of neighbours of a pair or of a triplet of neighbouring atoms in an fcc crystal.

For the case of adsorptions on top of a single atom, atop position, the atomic GCN of that atom will be of relevance in determining the adsorption strenght. When the adsorbate instead sits in between two adsorption sites, i.e. bridge position, the GCN of the pair determines the adsorbate adsorption energy. By the same token when the adsorbed molecule sits in a hollow position, i.e. surrounded by a triplet of atoms, the hollow GCN will correlate with the bonding strength. A visual description of the atoms determining the generalized coordination of a single atom, GCN atop, bridge pair, GCN bridge, and hollow triplet, GCN hollow, is reported in figure 2.7.

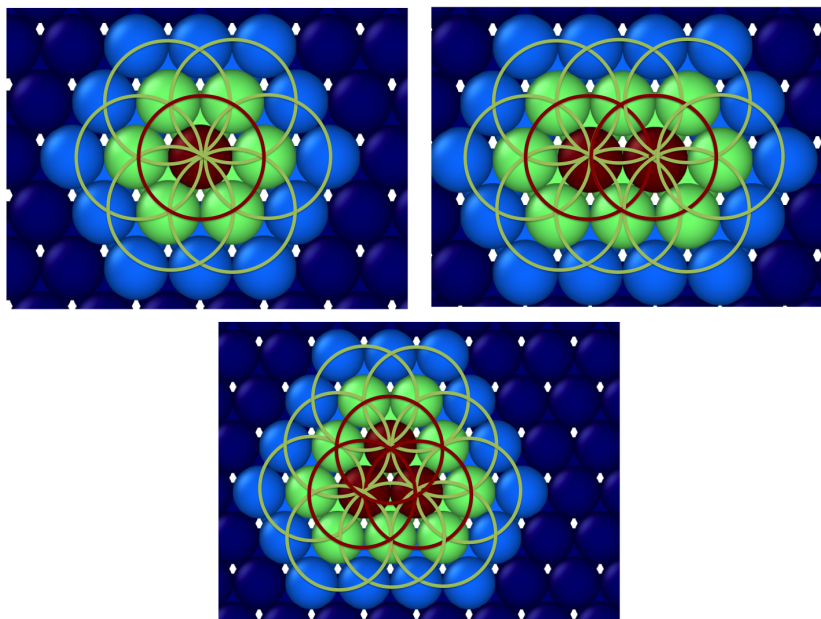


Figure 2.7 Visual representation of the atoms accounted for calculating the generalized coordination of a set of atoms atom in dark red shadowing. First nearest neighbour shells of the dark red atoms are delimited by red circles. Outer neighbour shells atoms determining the GCN of the dark red shaded atoms are inscribed in green circles. Reproduced from Ref. A genomic characterization of metallic nanoparticles - K. Rossi, G.G. Asara, F. Baletto - Physical Chemistry Chemical Physics 21 (9), 4888-4898, 2019 with permission from the PCCP Owner Societies.

2.6.1 Nanogenome of ideal closed-shell structures

As an illustrative example of nanogenome sequencing, we report the atomic GCN-genome of structures commonly observed in experiments, in the 1.5-7.5 nm range: cubes (Cb), octahedra (Oh), their regular truncations (To), cubocathedra (Co), icosahedra (Ih), and cuts of a pentagonal bipyramid referred to as the Ino-Decahedra (IDh), if they present no re-entrances ($p = 1$ in Equation 1.3), or Marks-Decahedra (MDh) if they display single atom-long re-entrances ($p = 2$ in Equation 1.3). For the decahedral structures, we consider cuts resulting in square (100) facets, that is $m = n$ according to the notation introduced in Section 1.1.

In Figure 2.8 we report, for each of the above mentioned structures, their visual representations at a given size, and size-dependent fingerprints. A clear pattern in the list of NEAS characteristic of each structure at different sizes emerges. Regardless of the shape, three size-regions, here discriminated according to the nanoparticle diameter, d_{np} , are evident. These are highlighted in Figure 2.8 in different colours and consist of the following:

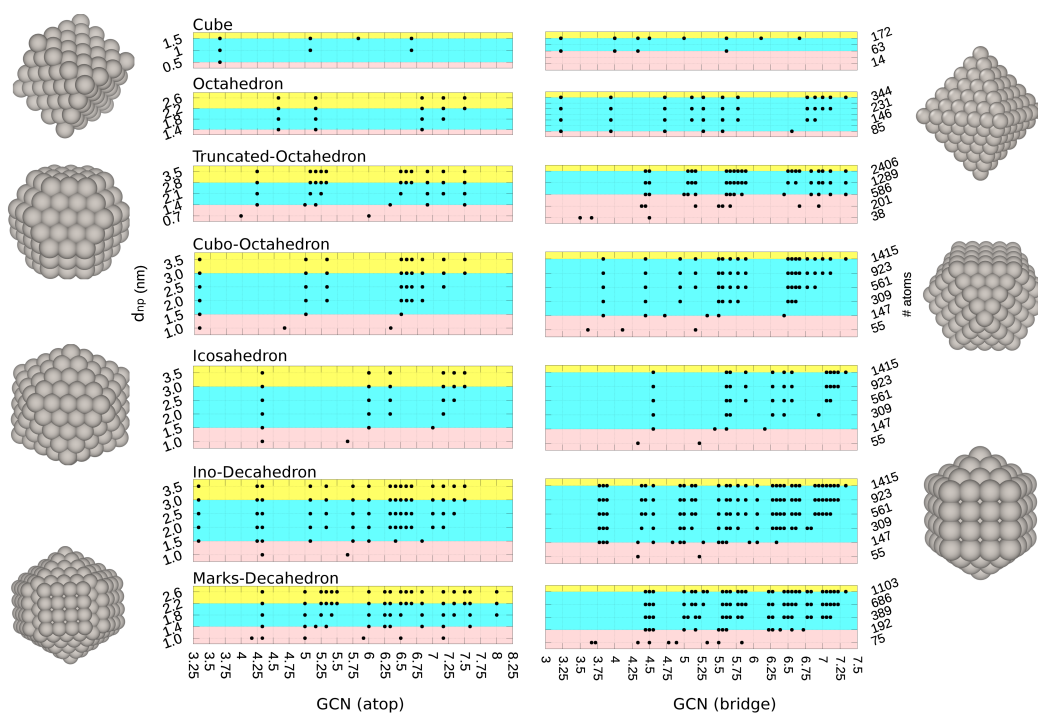


Figure 2.8 Nanoparticle GCN fingerprint size evolution in the seven structures under investigation (a snapshot of each is reported along side the graph), for atop (left) and bridge (right) adsorption. The three size regimes where the fingerprint is mobile (pink), incomplete (cyan), or fixed (yellow) are colour coded. Reproduced from Ref. A genomic characterization of metallic nanoparticles - K. Rossi, G.G. Asara, F. Baletto - Physical Chemistry Chemical Physics 21 (9), 4888-4898, 2019 with permission from the PCCP Owner Societies.

- For $d_{np} < 1.5$ nm, the nanoparticles display few NEAS. The GCN fingerprint presents signals that do not correspond to the GCN fingerprint of larger nanoparticles of the same morphology (pink shaded region).
- For $1.5 < d_{np} < 3.5$ nm, the GCN fingerprint is only partially corresponding to the one of a larger nanoparticle of the same shape, e.g. the facets are not large enough to accommodate all the NEAS present in larger systems such as the ones with $GCN > 7.4$ (blue shaded region).
- For $d_{np} > 3.5$ nm, all the considered morphologies display a complete GCN fingerprint which constitutes one of their distinctive geometrical attributes (yellow shaded region).

These size-regimes hint to the nanoparticles size(s) at which the electronic charge distribution at an active site is similar to its surface counterpart (if existing). By taking advantage of the GCN genome analysis we demonstrate how the properties of NEAS in large systems,

prohibitively expensive to be studied via electronic-structure methods, can be thus inferred from the ones of equivalent active sites in smaller nanoparticles.

The non-trivial interplay between size and shape effects drives NEAS relative occurrence. Vertex and close-to vertex sites are the first to appear. Yet, their number is fixed. Edge NEAS are the second to appear, followed by close-to-edge sites. Their occurrence scales linearly with size. Finally surface-like NEAS are observed. A quadratic dependence of their occurrence with nanoparticle size can be inferred from geometric considerations. Nanoparticles that present facets with a large (small) area to perimeter ratio show earlier (later) a full and constant with size GCN fingerprint. To substantiate this discussion with an example we show in Figure 2.9 and Figure 2.10 the non-equivalent active site size-occurrence scaling in Octahedra of different nuclearities, for both atop and bridge sites. We further report on how to enumerate NEAS occurrence as a function of the number of atoms along the edge of the Octahedron.

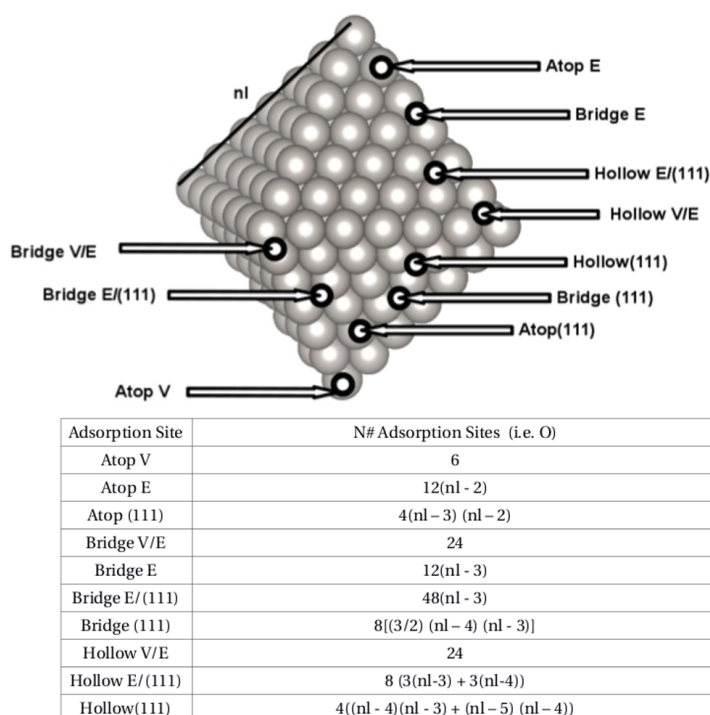


Figure 2.9 A visual resume of the non equivalent active sites for atop adsorption in an Octahedron. For each case we report polynomial expressions that allow to estimate each NEAS occurrence as a function of the number of atoms, nl , at the Oh edge. Reproduced from Ref. A genomic characterization of metallic nanoparticles - K. Rossi, G.G. Asara, F. Baletto - Physical Chemistry Chemical Physics 21 (9), 4888-4898, 2019 with permission from the PCCP Owner Societies.

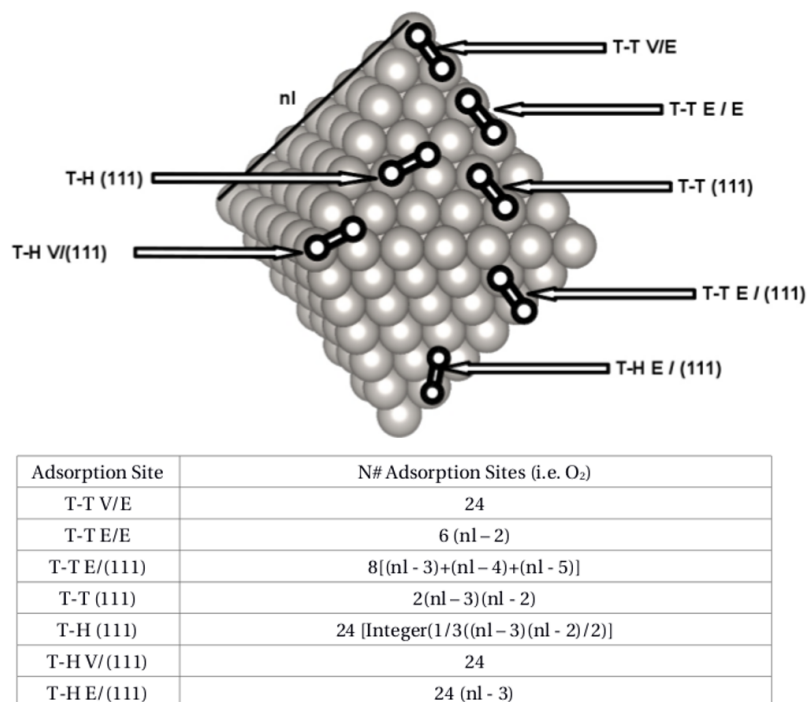


Figure 2.10 A visual resume of the non equivalent active sites for bridge adsorption in an Octahedron. For each case we report polynomial expressions that allow to estimate each NEAS occurrence as a function of the number of atoms, nl , at the Oh edge. Reproduced from Ref. A genomic characterization of metallic nanoparticles - K. Rossi, G.G. Asara, F. Baletto - Physical Chemistry Chemical Physics 21 (9), 4888-4898, 2019 with permission from the PCCP Owner Societies.

Moreover in Figure 2.11 we report the size-dependent relative abundance of NEAS in Oh nanoparticles. At $d_{cl} \sim 2.6$ nm, 344 atoms, the relative occurrence of each NEAS is rather similar, only NEAS with GCN ~ 7 are slightly more common than others. At $d_{cl} = 4.3$ nm, 1156 atoms, only the (111) surface sites (GCN=7.5) and the NEAS with GCN=7.16 display a comparable occurrence. The favourable scaling of surface-like NEAS drives their larger frequency at bigger sizes. Indeed, at $d_{cl} = 7$ nm (4579 atoms), (111) NEAS relative occurrence is approximately the 55%. Similarly, for a nanoparticle of 10425 atoms, $d_{cl} = 9.5$ nm, (111) sites top to the 70% of the total.

GCN fingerprint features can be also rationalized from the cluster morphology. Nanoparticles show a more diversified fingerprint, depending on the number of different terminations they present. Cb, Oh, and Ih display the smaller number of NEAS. Indeed they are terminated only by (100) (Cu), or (111) (Oh and Ih) facets. Co, IDh, and To present a larger number of NEAS as they encompass both (100) and (111) facets. 5-fold twinned re-entrant nanoparticles

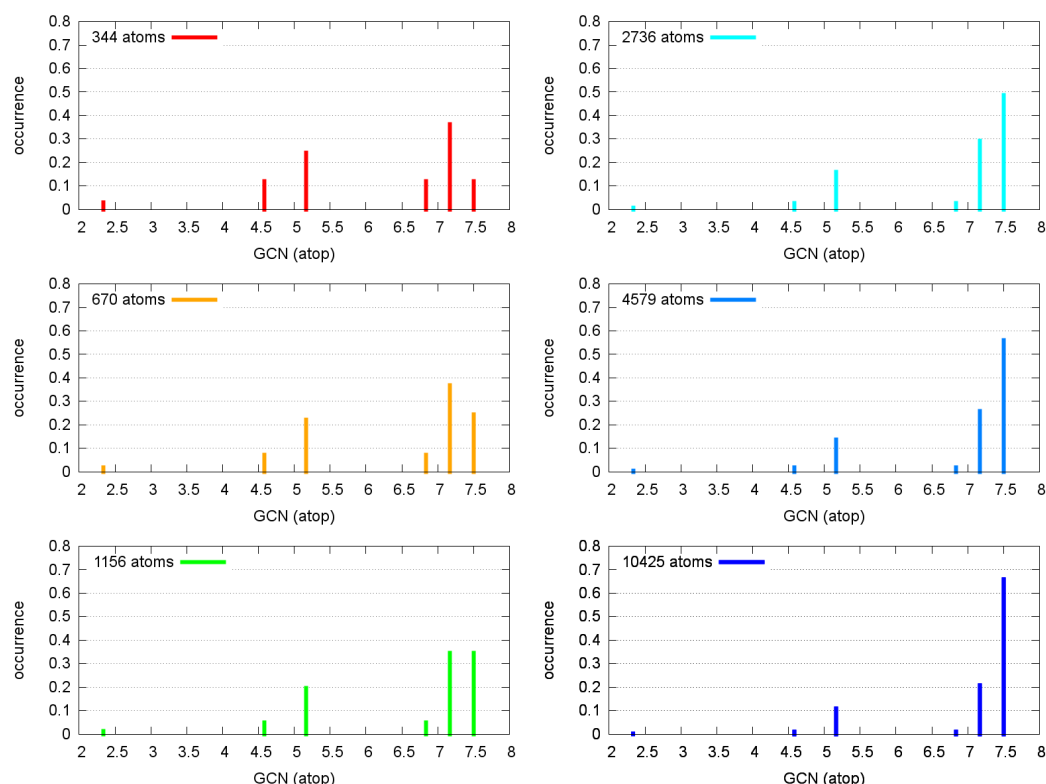


Figure 2.11 A visual representation of the genome for Oh morphologies of different size(top left label of each plot). As expected from a geometric argument the relative occurrence of (111) sites, i.e. $GCN(atop)=7.5$, increases quadratically with cluster size and determines their more frequent occurrence with respect to other NEAS in Oh nanoparticles with more than ~ 3000 atoms. Reproduced from Ref. A genomic characterization of metallic nanoparticles - K. Rossi, G.G. Asara, F. Baletto - Physical Chemistry Chemical Physics 21 (9), 4888-4898, 2019 with permission from the PCCP Owner Societies.

present the largest number of NEAS. Morphologies which share a given local environment, also display adsorption sites characterized by the same GCN values, e.g., active sites with $GCN=7.5$ lie on (111) facets and are found in all the architectures here discussed, apart for cubes. By the same token, active sites with $GCN(atop)=6.66$, i.e. sites on (100) surfaces, are found in all structures apart Ih and Oh. Only re-entrant structures present concave NEAS with $GCN(atop) > 7.5$. This geometric considerations are exemplified by the circos plot reported in Figure 2.12. Here, NEAS in the seven commonly observed structures are reported in the left hand side, while the individual genomes in the seven different geometry (of size ~ 1000 atoms) under scrutiny lie on the right hand side. A band connects the two if the former belongs to the latter.

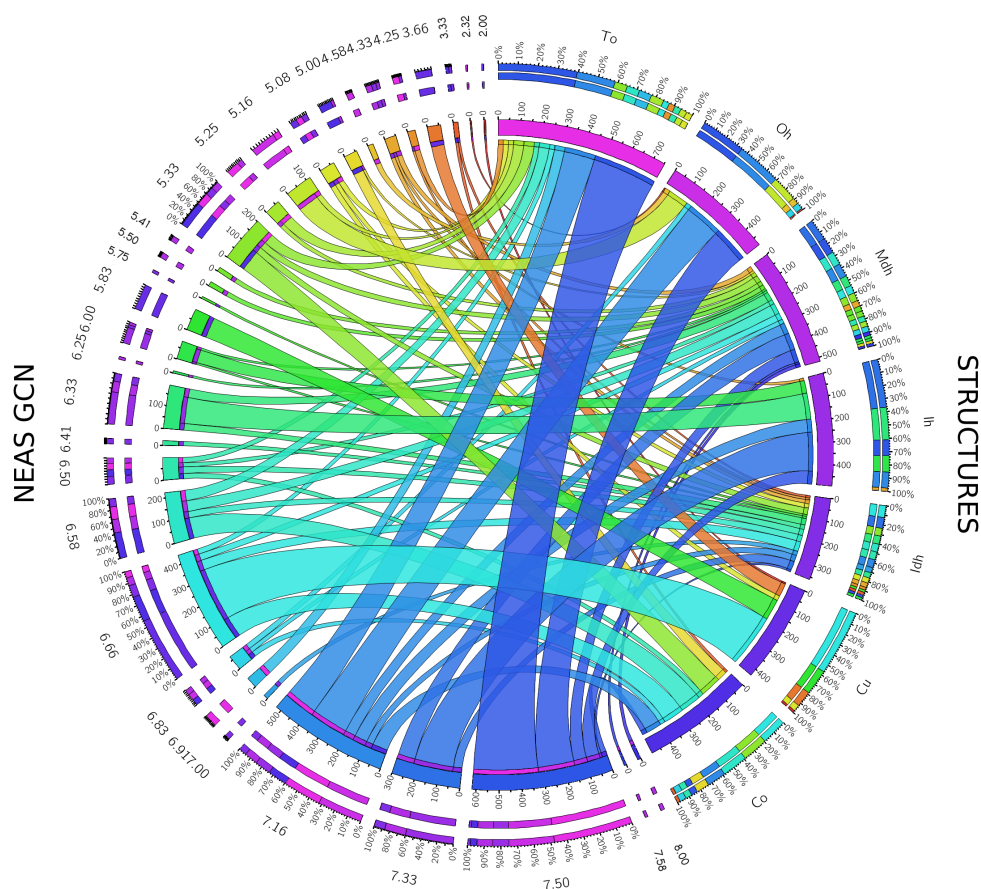


Figure 2.12 Circos plot to represent the relationships between NEAS, labelled according to their GCN value, and the nanoarchitectures they are observed in. Bands of different colour connect NEAS (left portion of the circle) and the nanoarchitecture (right portion of the circle) they belong to. For each architecture we report the relative (outer circle) and nominal (inner circle) occurrence of each non equivalent active site. For each NEAS we report their relative (outer circle) and nominal (inner circle) distribution in the different nanoparticles under consideration. Reproduced from Ref. A genomic characterization of metallic nanoparticles - K. Rossi, G.G. Asara, F. Baletto - *Physical Chemistry Chemical Physics* 21 (9), 4888-4898, 2019 with permission from the PCCP Owner Societies.

Nanoparticle Area The sequencing of the adsorption sites in a nanoparticle according to their generalized coordination further provides ground for the calculation of the nanoparticle area. The calculation of this quantity is highly non-trivial especially for the case of imperfect polyhedra. On the other hand this property is of strong significance in determining the catalytic performance of a nanoparticle.

The approach proposed to estimate the area of a nanoparticle is based upon the following argument. Let r_{at} be the atomic radius, the exposed area of a single atom is, within the approximation of atoms as spheres:

$$A_{atom} = 4\pi r_{at}^2 \quad . \quad (2.37)$$

For the case of an atom in a nanocluster, depending on its coordination, it will either:

- not contribute to the area of the nanoparticle because it's in the inner layers, i.e. it's not an adsorption site.
- contribute in relation to its coordination, with low coordinated atoms being more exposed than highly coordinated ones, thus contributing largely.

The nanoparticle area A_{NP} can be thus estimated as the sum of the exposed areas of each adsorption site kind in the nanoparticle, weighted according to its coordination and occurrence:

$$A_{NP} = 4\pi r_{at}^2 \sum_{\alpha} \left(1 - \frac{GCN_{\alpha}}{12} \right) \Omega_{\alpha} \quad , \quad (2.38)$$

where the $(1 - \frac{GCN_{\alpha}}{12})$ term corresponds to the free exposed atomic surface, while Ω_{α} is the total number of α sites presenting a GCN_{α} coordination. It is worth to note that, although tempting, the use of the nominal coordination number of adsorption sites to estimate the exposed area of an adsorption site yields a too low estimate for the case of atoms lying on (100) and (111) surfaces. Indeed for the case of the generalized coordination number approach, the exposed area of such adsorption sites is approximately half of that of a single atom, as expected from a heuristic geometrical argument.

2.6.2 Towards in operando conditions

The formalism of the GCN nanogenome sequencing is immediately transferrable to the case of nanoparticles not in the gas phase so to mimick conditions more closely related to *in operando* ones.

Supported nanoparticles When sequencing the NEAS of a nanoparticle on a substrate one must exclude the sites which lie at the interface between the nanoparticle and the support. To this end we exclude from the genome calculations atoms within a spherical sector with height = 5 Å and base radius equal half the maximum distance between atoms in the layer in contact with the substrate, defined as atoms with $z < 3$ Å, with $z = 0$ being the height at which the surface of the support is centered. In Figure 2.13 we show an illustrative example of the resulting exclusion zone for two nanoparticle presenting a different wetting and contact area. Note that this choice allows to treat on an equal footing structures presenting both obtuse or acute wetting angles. Due to the distortion induced by the support, the cutoff for enumerating the atoms in the first coordination shell is further set to 2.5 times the atomic radius (instead of 2.4 times as in the gas phase). Indeed the definition of the GCN does not include the contributions arising from the nanoparticle-support interaction, likely to propagate one layer (to few at maximum) above the contact one.

Further in Figure 2.14 we report how the genome of the example structure in the left hand side of Figure 2.13, an Ih nanoparticle of 561 atoms, changes with respect to the

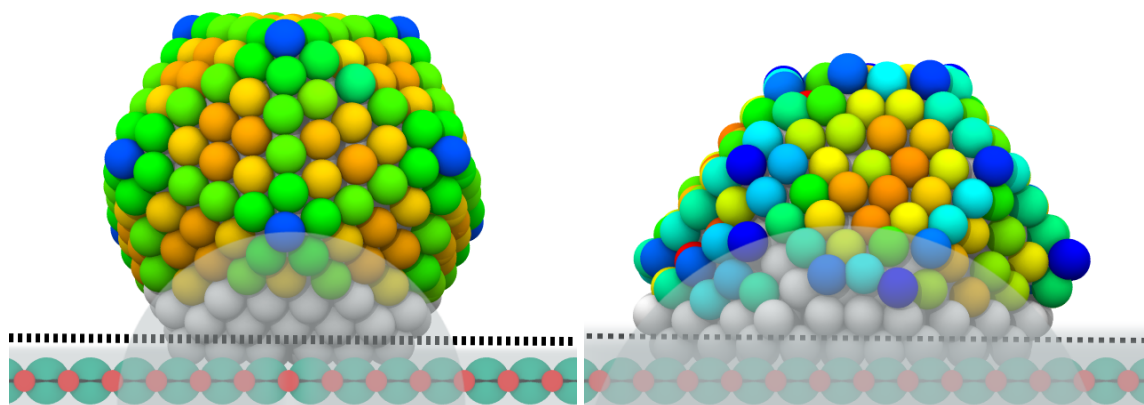


Figure 2.13 Representation of the spherical sector exclusion zone of active sites from the genome for the case of nanoparticles supported on a substrate. Atoms in grey are excluded from the genome, the others are colour coded according to their generalized coordination (blue = low coordinated, red = highly coordinated). Atoms in grey contribute to the coordination of their neighbours even if excluded from the genome.

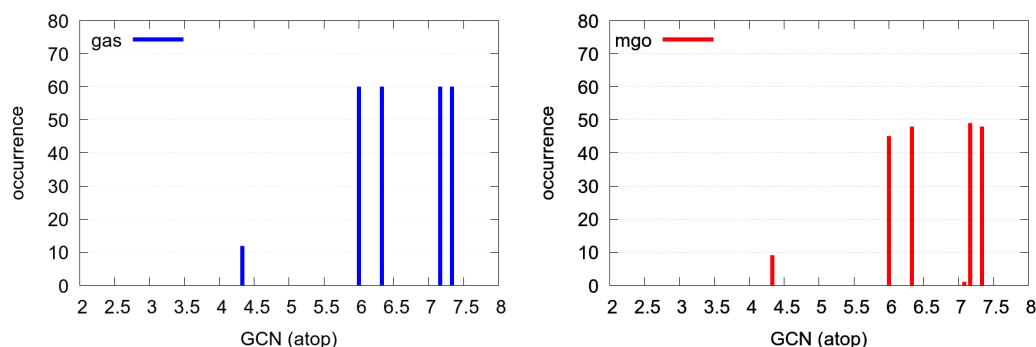


Figure 2.14 GCN(atop) nanogenome of an Icosahedral nanoparticle of 561 atoms in the gas phase (left) and supported on an MgO substrate (red) where the exclusion principle discussed above diminishes each NEAS occurrence.

gas phase case: a net decrease in the occurrence of each of the NEAS in the nanoparticle is witnessed. Although the choice of the parameters determining the exclusion zone was heuristic, a sensible ensemble of sites is excluded in all the investigated cases, as the ones here shown on the right hand side of Figure 2.13.

Ligand protected nanoparticles To account for the presence of ligands coating the nanoparticle and for their effect on the nanoparticle properties, three different model assumptions can be envisioned:

- Model (1): the ligand forbids adsorption on the site it is bonded to.
- Model (2): the ligand forbids adsorption on the sites it is bonded to, and the one it covers under its Tolman cone.[90]
- Model (3): the ligand modifies the metallic coordination of the site it is bonded to, and thus the generalized coordination number of the atoms in the first neighbour shell of the latter.

The resulting nanoparticle genomes may be thus strongly affected. Figure 2.15 reports the genome of a Pt_{561} nanoparticle, where a single atom (colour coded in blue) is bonded to a ligand whose Tolman cone is 3 \AA (shadowed in grey), for the different models presented earlier and for the bare gas phase as reference. Within the assumptions of Model (1), top right panel, the genome is poorly affected with respect to the gas phase reference, with the two GCN genomes differing only because of the absence of a single site. When accounting for the Tolman cone 7 sites are instead subtracted from the gas phase genome, as shown in the bottom left subfigure, for Model (2). The complexity inherent to the case of a change

of the metallic coordination of the ligated site is reflected in the genome of the nanoparticle calculated following model (3), reported in the bottom right panel of Figure 2.15. Indeed 15 NEAS and not just 5 as in the bare nanoparticle case are observed. Although this newly developed site-counting method is at its infancy, it is worth to note that it may enable to explain non trivial size-dependent non-monotonic trends at large sizes where surface-like behaviours are instead expected. Indeed, ligands preferential attachment to facets sites may hinder strongly adsorption of nanoparticles presenting large facets, but yet not large enough to emerge out of the Tolman cone of the ligand.

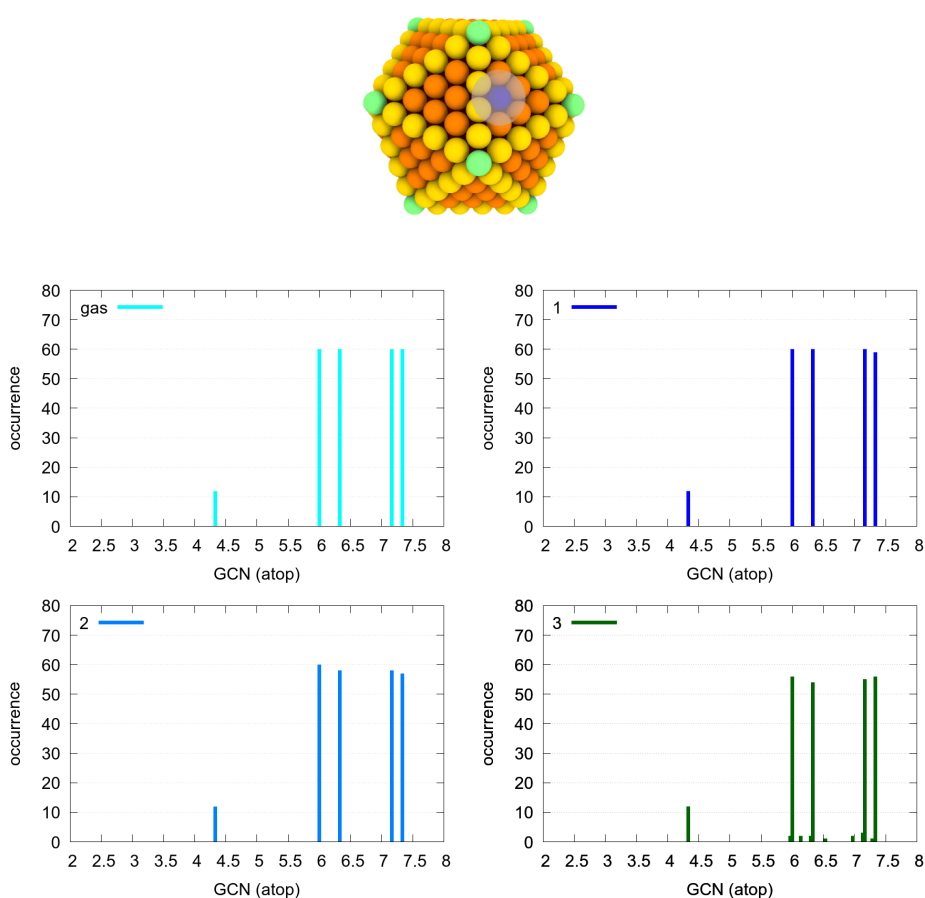


Figure 2.15 Top panel shows an Icosahedral nanoparticles of 561 atoms where atoms are colour coded according to their generalized coordination, from light tones (green = lower coordinated) to hot ones (orange = highest coordinated). The ligated atom is highlighted in blue and its Tolman cone is represented by a grey shadowing. Lower panel displays the GCN(atop) nanogenomes of the nanoparticle in the gas phase (top left), and according to Model 1 (top right), Model 2 (bottom left), and Model 3 (bottom right).

2.7 Nanogenomics hydrogen evolution model

Towards the prediction of macroscopic observables related to the catalytic performance of nanoparticles we adapted the computational hydrogen electrode model (CHE) [91, 60] to forecast currents from reactions taking place at any active site, as a function of a geometrical descriptor, GD, which links explicitly the active site topological and catalytic properties. Considering only the degree of endoergonicity of the process, the CHE model provides an upper limit for the reaction rate by disregarding (intentionally) any activation barriers [91, 60] other than the maximum reaction free energy of any i -elementary step while avoiding the explicit treatment and calculation of the free energy of solvated protons involved in the formation of water. For the case of Oxygen reduction reaction this reads:



where, in reversible hydrogen electrode conditions, the reaction $H^+ + e^- \rightarrow 1/2H_2$ is in equilibrium at 0 V, and at any other potential the free energy change results:

$$G(H^+ + e^-) = G(1/2H_2) - eU \quad (2.40)$$

where G is the free energy associated to each reaction state, e is the electron charge and U the applied potential. When evaluating the reaction free energy for water formation at a certain potential, $\Delta G_\alpha(U)$, in the CHE framework the free energy of H^+ is substituted with the one for $1/2H_2 - eU$. In turn, the current density produced by a reduction reaction happening at a given site α at temperature T and applied potential U results:

$$j_\alpha(T, U) = \mathcal{C}_\alpha e^{\beta(T)\Delta G_\alpha(U)} \quad (2.41)$$

where β is the Boltzmann factor (with temperature fixed to 300 K in the here reported calculations) and the coefficient \mathcal{C}_α matches the active site limiting specific current. In its GD-adapted version, we assume that the free energy ΔG and the limiting current \mathcal{C} can be calculated as a function of a geometrical descriptor GD. j_α thus results:

$$j_\alpha(GD, T, U) = \mathcal{C}_\alpha(GD) e^{\beta(T)\Delta G(GD, U)} \quad (2.42)$$

Gathering information from the local properties of each active site one can in turn rationalise the nanoparticles' global catalytic activity as a function of their size and shape. The current density produced by a nanoparticle, j_{NP} , at temperature T and applied potential U can be thus estimated taken as the sum of all the non equivalent adsorption sites contributions,

weighted for their relative occurrence $\frac{\Omega_\alpha}{N_{NP}}$:

$$j_{NP}(T, U) = \sum_{\alpha \in NEAS} \frac{\Omega_\alpha}{N_{NP}} j_\alpha \quad (2.43)$$

where N_{NP} is the total number of adsorption sites, and Ω_α is the number of α sites presenting a given generalized coordination. An example application of the model here proposed is discussed for the case of Pt nanoparticle and oxygen reduction reaction in Chapter 6.

2.8 Rearrangements characterization

Beyond structure characterization routines, quantitative descriptors to analyse rearrangements as a function of the evolution of the bond networks in a nanoparticle have been also developed and implemented in a LoDiS suite. Let the adjacency matrix M_{ij} , be a $N \times N$ matrix, where N is the number of atoms in the nanoparticle, with entries equal to 1 if i and j are nearest neighbours atoms and 0 otherwise. We calculate the matrix, $MM_{ij}(\Delta t)$, by counting the number of bond formed or lost in a characteristic time length Δt :

$$MM_{ij}(\Delta t) = |M_{ij}(t + \Delta t) - M_{ij}(t)|. \quad (2.44)$$

By monitoring the evolution of the adjacency matrix over time, it is possible to observe when and how a rearrangement takes place. For reference, if no bonds are changed $MM_{ij}(\Delta t) = 0$ in all its entries, if all of them are renewed, for the case of fcc-bulk atoms, $\sum_{j \neq i} MM_{i,j}(\Delta t) = 24$.

Mobility index The system mobility during a rearrangement, $R(t, t + \Delta t)$, can be thus estimated by summing over the single atoms local mobilities:

$$R(t, t + \Delta t) = \sum_i R_i(t, t + \Delta t), \quad (2.45)$$

$$R_i(t, t + \Delta t) = \sum_{j \neq i} MM_{ij}(\Delta t) \quad (2.46)$$

Collectivity index To estimate the collectivity of a mechanism, H , one can thus count the portion of atoms changing at least one nearest neighbour, during a Δt time interval, and the total number of atoms in the cluster:

$$H = \sum_i \frac{\Theta(R_i(t, t + \Delta t))}{N} \quad \begin{cases} \Theta(0) & = 0 \\ \Theta(R_i) & = 1 \forall R_i > 0 \end{cases} \quad (2.47)$$

H ranges between 0 and 1: $H = 0$ when no bond has been broken/formed, $H = 1$ when all atoms change at least one neighbour.

Concertedness index We define the degree by which a rearrangement is concerted, C , as the difference between the number of atoms involved in the process between $t - \Delta t$ and t , and between t and $t + \Delta t$.

$$C(t - \Delta t, t, t + \Delta t) = |H(t - \Delta t, t) - H(t, t + \Delta t)|. \quad (2.48)$$

If all atoms undergo a change in their neighbourhood at time t , but none in the successive one $t + \Delta t$, $C(t - \Delta t, t, t + \Delta t)$ peaks at its maximum value of 1. Single-step mechanisms involving only a sector of the cluster, or multi-step processes are characterized by lower values of $C(t - \Delta t, t, t + \Delta t)$, while continuous atomic rearrangements display $C \sim 0$.

These descriptors can be readily specialized to account for the presence of more than one chemical species in the cluster, $chem = A, B$

$$R^{chem}(t, t + \Delta t) = \sum_i R_i^{chem}(t, t + \Delta t), \quad (2.49)$$

where R_i^{chem} is given by

$$R_i^{chem}(t, t + \Delta t) = \sum_{j \neq i} |M_{ij}^{chem}(t + \Delta t) - M_{ij}^{chem}(t)|. \quad (2.50)$$

$$H^{chem} = \sum_{i \in chem} \frac{\Theta(R_i^{chem}(t, t + \Delta t))}{N^{chem}} \begin{cases} \Theta(0) = 0 \\ \Theta(R_i^{chem}) = 1 \quad \forall R_i^{chem} > 0. \end{cases} \quad (2.51)$$

$$C^{chem}(t - \Delta t, t, t + \Delta t) = |H^{chem}(t - \Delta t, t) - H^{chem}(t, t + \Delta t)|. \quad (2.52)$$

H and C depend on the choice of Δt , which has to capture the fastest structural movement of interest. A too large Δt may lead to a dramatic change in the H and C estimate by coarsening different atomic rearrangements into a single instance. On the other hand, a too small Δt may disguise a single step rearrangement as a multi-step one because, although the rearrangement of several neighbours is simultaneous, the degree in the bond breaking/elongation might not be identical for each pair, leading to an artifact discretisation of how the system adjacency matrix varies. In the following, we opt for $\Delta t = 10$ ps, roughly the time scale over of diffusion process on low Miller index facets, as it represents the fastest process we want to discriminate.

2.9 Sampling Techniques in LoDiS

The sampling of the nanoparticle energetic landscape at finite temperature by means of molecular dynamics may be rather inefficient. A set of sampling techniques are thus implemented in LoDiS to overcome this challenge. Indeed, high energetic barriers may hinder structural rearrangements, hence leading to a not fully informative sampling of the energetically relevant portion of the potential energy of the systems under investigation. Further, some processes such as nanoparticle melting and freezing likely necessitate the use of methods beyond simple NVT and NVE MD sampling because of their non-equilibrium nature.[92, 25]

2.9.1 Metadynamics

Metadynamics (MetaD) [93, 94] is an enhanced sampling algorithm coupled to Molecular Dynamics to simulate rare events such as morphological transitions between structural basins separated by high energetic barriers. MetaD acts in a coarse grained representation of the dynamics of the system, i.e. in a reduced dimensionality order parameter space, also known as collective variables space, by building up an history dependent potential to enhance minimum-minimum transition, thus allowing a wider exploration of the conformational space of the system with respect to canonical Molecular Dynamics sampling. According to the standard Metadynamics formalism the biasing potential ΔV evolves in time as the sum of Gaussians of height ω and width σ added every t_G time interval

$$\Delta V(CV(r_{ij,t}), t) = \sum_{t'=t_G, 2t_G, \dots} \omega e^{-\frac{[CV(r_{ij,t}) - CV(r_{ij,t'})]^2}{2\sigma^2}}, \quad (2.53)$$

where $CV(r_{ij})$ represents the set of collective variables chosen and defines the order parameter space where the MetaD potential evolves, with $CV(r_{ij}(t_0))$ being the value of the collective variable at time t_0 . After a transient, the Metadynamics potential provides an unbiased estimate of the underlying free energy, F :

$$\Delta V(CV, t \rightarrow \infty) = -F + constant. \quad (2.54)$$

In particular, for a well-tempered evolution of the Gaussian deposition and the presence of a Langevin diffusion regime for transitions between basins in the energy landscape, the exact reconstruction of the free energy surface from the deposited Gaussians was demonstrated.[95]. Well-tempering is carried on by damping Gaussian height depending on the presence of other

previously deposited gaussians in a local portion of the CV space as:

$$\omega(t_G) = \omega_0 e^{\left(\frac{-\Delta V(CV(r_{ij,t}),t)}{kB\Delta T}\right)} \quad (2.55)$$

where ω_0 is the initial Gaussian height, ΔT an input parameter with the dimension of a temperature, and kB the Boltzmann constant. This Metadynamics variant, though possibly yielding more converged results, is more time consuming and has not been employed during the investigations presented in this thesis.

2.9.2 Metadynamics collective variables

Metadynamics reliability and robustness depend on the collective variables of choice. Collective Variables (CVs) should determine a metric which discriminates the different configurations sampled, while being representative of the slow degrees of motions in the structural rearrangement of interest. Moreover, the number of collective variables to be used in a simulation should be limited so to minimize computational expenses. When these requirements are not respected, it is likely that the system will be forced into high energy configurations. Further, processes of interest may be hidden by the chosen reduced dimensionality space choice. [94]

Coordination based collective variables The coordination number is a well-known CV to promote diffusion driven rearrangements. For this reason we proposed [96] the hetero (*HeCN*) and homo (*HoCN*) coordinations numbers as efficient CVs to simulate chemical reordering via single atom intracluster or surface diffusion. Let p_0 be the nearest neighbour bulk reference distance, q_0 as the distance related to the width of the descending branch of a sigmoid function f , set to 0.05 times the bulk lattice constant, and n and m as the powers used to tune smoothness and asymptotic behaviour of the analytic function f , the hetero coordination number, *HeCN*, results:

$$HeCN = \sum_{i,j} f(r_{ij}),$$

$$f(r_{ij}) = \begin{cases} 1 & \text{if } r_{ij} \leq p_0, \\ 1 - \left(\frac{r_{ij} - p_0}{q_0}\right)^n & \text{if } r_{ij} > p_0, \end{cases} \quad (2.56)$$

where n and m take the numerical value of 6 and 12 in the simulations reported in this thesis.

Although using the *HeCN* as sole collective variables enables to sample efficiently minima with various chemical ordering and energy differences of several eV, it does not encode enough information to discriminate among nanoparticle shapes. This implies that nanoparticles presenting different motifs but similar chemical orderings are projected onto the same basin, hampering the possibility to reconstruct faithfully the free energy profile.

Pair distribution function based collective variables As first discussed in [97] window functions on the PDF enables to readily distinguish common metallic nanocluster structures, Figure 2.4, and equally capture the slow degree of motions involved in concerted structural rearrangements among them. A window function is evaluated as:

$$WF(x) = \sum_{i,j;i \neq j} \frac{1 - \left(\frac{r_{ij}-d_0}{r_0}\right)^6}{1 - \left(\frac{r_{ij}-d_0}{r_0}\right)^{12}}, \quad (2.57)$$

where r_{ij} is the distance between the i^{th} and j^{th} atoms, r_0 the window width, set to 0.05 times the bulk lattice constant, and d_0 is the window function characteristic distance. We note that Equation 2.57 takes a similar form of 2.56, here however distances contracted or elongated with respect to the reference one are treated on the same footing. d_0 is set to be 1.354 and 3.4 of the bulk lattice parameter for the calculation of the stacking fault number (SFN) and the maximum pair distance difference number (MPDN) respectively.

A physical argument supports the choice of these collective variables. The SFN is evaluated at a characteristic hcp peak in the PDF, indeed, the one corresponding to topological defects arising from the intersection of two planes with different symmetry orientation. At the nanoscale, as in the bulk, morphological transformations happen via nucleation and vanishing of stacking faults. The defining structural feature of multiply-twinned (fcc cut) nanoparticles is indeed the presence (absence) of grain boundaries and stacking faults. Consequently, a bias on the stacking fault number collective variable should not constrain the FES exploration to unphysical structural transitions while driving the sliding and rotation of (111) planes. Similarly, the maximum pair distance number collective variable window is centred where the PDF of different geometries of interest are not highly overlapping. In turn this collective variable will also promote breathing and concerted rearrangements and will be only partially correlated to the SFN CV.

2.9.3 Iterative temperature molecular dynamics

Iterative Temperature Molecular Dynamics (itMD) consists of concatenated loops where the temperature is lowered or increased by the quantity ΔT every $\Delta \tau$ time. The kinetics of structure or phase changes can be thus analysed in terms of a single parameter, the temperature change rate, $\lambda = \frac{\Delta T}{\Delta \tau}$. ItMD is in turn an efficient and suitable tool to sample representative trajectories at finite temperatures while estimating caloric curves for either freezing formation processes and nanoparticles melting. Further, itMD allows to probe the occurrence of shape fluctuations occurring in a time scale comparable with the chosen observation time scale at different finite temperatures.

2.9.4 Other sampling tools employed for comparison

Although not implemented in the LoDiS package, other sampling tools have been used parallel to itMD and MetaD simulations to further the discussion of energetic, kinetic and entropic contributions in determining structural stability of a nanoparticle against melting and pre-melting transitions.

Nested sampling Nested sampling (NS) is an algorithm to estimate the density of states of a system.[98, 99] The latter is obtained by selecting a set of decreasing potential energy levels, E_i , starting from an high energy phase (e.g. a vapour of metallic atoms for the case of nanoparticles). Each level bounds from above a volume of configuration space χ_i , with χ_i being approximately a constant and smaller than the volume χ_{i-1} , corresponding to the level above. This is obtained by starting from randomly selected configurations uniformly distributed and bounded above by energy E_i . A new energy level is obtained by discarding the energy of the configuration with highest energy, and reconstructing the uniform distribution under a new energy limit. From the discretisation of the cumulative density of states $\chi(E)$, the partition function of the system can be evaluated at arbitrary temperatures,

$$Z(N, V, \beta) = \frac{1}{N!} \left(\frac{2\pi m}{\beta h^2} \right)^{3N/2} \int dE \chi'(E) e^{-\beta E} \quad (2.58)$$

$$\approx Z_m(N, \beta) \sum_i (\chi_{i-1} - \chi_i) e^{-\beta E_i} \quad (2.59)$$

where N is the number of particles of mass m , V is the volume, β is inverse thermodynamic temperature, h is Planck's constant, the density of states χ' is the derivative of χ , and we labelled the factor resulting from the momentum integral as Z_m . A detailed discussion of the comparison between itMD and NS results is reported in Section 5.1.

Double ended transition path sampling Double ended transition path sampling uses a double-ended nudged elastic band method [100] between local minima (endpoints) to find a transition state guess that links them. This search is refined by means of an eigenvector-following calculation. Once the transition state is found, paths crossing it and connecting two neighbouring local minima are calculated through steepest-descent energy minimisations. In this way a sequence of minimum-minimum transitions is identified. If these two minima coincide with the endpoints of the search, the problem is solved, otherwise more searches of transition states and local minima are iteratively performed until a multi-step pathway connecting the endpoints is found. The analysis of the relationship between the energetic barriers for rearrangements between archetypical nanoparticle structures are discussed in Chapter 3 and 4.

Chapter 3

On concerted rearrangements in monometallic nanoparticles

Morphology, size, and composition determine nanoparticle's chemophysical properties. Solid-solid transitions imply a change in the structural features of a nanoparticle, and in turn, of its catalytic, optic, and magnetic properties. Forecasting the accessible structural fluctuations in a nanoparticle is then fundamental to predict and suggest how to control, through specific synthesis routes, the structural polydispersity of nanoparticle ensembles. This, in turn, would open the path to tailoring in a controllable manner nanoparticle physicochemical properties, or at least to forecasting their changes over time by predicting which structural rearrangements may take place.

3.1 Concerted rearrangement in gas phase nanoparticles

Here we will discuss the study of the rearrangement mechanisms by which metastable structures may evolve, for the case of monometallic nanoparticles. We here systematically probe and discuss structural transitions among the Ih, IDh, and Co minima for magic size monometallic nanoclusters of Ni, Pd, Pt, Cu, Ag, and Au, of 55, 147, 309, and 561 atoms. The choice of these sizes is dictated by the structural crossover ones predicted in [3]: Ih structures become unfavourable with respect to Dh ones for nanoparticles of ~ 500 atoms with deviations around this value which can be recast in terms of the stiffness of the interatomic potential.

3.1.1 Computational set-up and analysis method

The numerical tools involved in this study are iterative temperature Molecular Dynamics and Metadynamics. The former consists of concatenated iterations of canonical Molecular Dynamics where the system temperature, starting as low as 10K, is increased by 10K every 1 ns, up to the melting of the nanocluster. The latter enables the sampling of structural rearrangements at room temperature, and involves the use of the pair distance distribution functions collective variables (equation 2.57). The Metadynamics potential is developed through the deposition of Gaussian of height 0.05 eV and width 15 (adim) multiplied by the number of cluster shell(s) (55 atoms = 1 shell, 147 atoms = 2 shells . . .) every 10 ps.

In a Metadynamics simulation, when two different minima are explored successively, e.g. for a Dh \rightarrow Ih transition followed by a Ih \rightarrow Dh transition, $\Delta F_{\rightarrow Ih}$ and $\Delta F_{\rightarrow Dh}$ are taken as the negative of the meta-potential so far developed, as discussed in Equation 2.54. Their estimate is formally correct only when a diffusive transition regime is reached, for a well-tempered simulation, and when the CV(s) of use correspond to the slow variable(s) in the transition. When a minimum is not sampled twice during a Metadynamics simulation, we then provide a heuristic (over)estimate of the free energy barrier, $\Delta F_{\rightarrow Ih}^*$. This is taken as the highest point in the energy landscape reconstructed from the meta-potential when the initial basin is left. We thus report its mean value $\overline{\Delta F_{\rightarrow Ih}^*}$ by averaging the $\Delta F_{\rightarrow Ih}^*$ found in at least 8 independent MetaD runs.

For the case of itMD simulations, it is relevant to note the temperature at which the nanoparticle rearranges into an Ih via a martensitic rearrangement, $T_{\rightarrow Ih}$, or the one for which at least two atoms display a coordination of 10, $T_{\rightarrow dX}$, suggesting the start of collective surface diffusion processes. In Table 3.1 we will report $T_{\rightarrow Ih}$ or $T_{\rightarrow dX}$, depending on whether the former or the latter are first observed, averaged with respect to the number of independent runs we performed (at least 8), and normalized with respect to the melting temperature of the nanoparticle. We here recall that the chosen observation time scale and the basin from which sampling starts dictate the topology of the portion of the free energy landscape sampled through itMD.

The CNA (2,0,0) and (5,5,5) relative abundance with the evolution of the system is monitored to characterize the nanoparticle structure, while the eventual rearrangement mobility, collectivity, and concertedness are estimated following what discussed in Section 2.8, Equations 2.46, 2.47, 2.48.

3.1.2 Size and shape effects

For the case of the investigated systems, we observe that structural rearrangements between different archetypical basins take place via highly concerted mechanisms -the so called Diamond-Square-Diamond (DSD) ones, reported in Figure 3.1 - while surface diffusion drives solid-solid transitions within a given archetypical motif, as shown in Figure 3.2. Though the archetypical motif remains the same, structural features in the nanoparticle change dramatically, e.g. note the absence of (100) facets in the last snapshot reported in Figure 3.2.

A DSD mechanism consists of a stretching and rotation of triangular facets into a diamond first, and in a square then, by a collective screw dislocation of atoms. The dislocation corresponds to a rotation of different angles according to the initial and the final configurations. Conversely, a squared facet can transform into two triangular facets by the opposite movement. Five parallelograms are involved in the collective rearrangement $Dh \leftrightarrow Ih$ (Figure 3.1 top panel) and six in the case of the $Co \leftrightarrow Ih$ (Figure 3.1 lower panel).

Surface peeling instead comprises a variegated set of adatom hopping, diffusion, vacancy diffusion, and atomic exchanges at the surface of the nanoparticle, leading to the formation

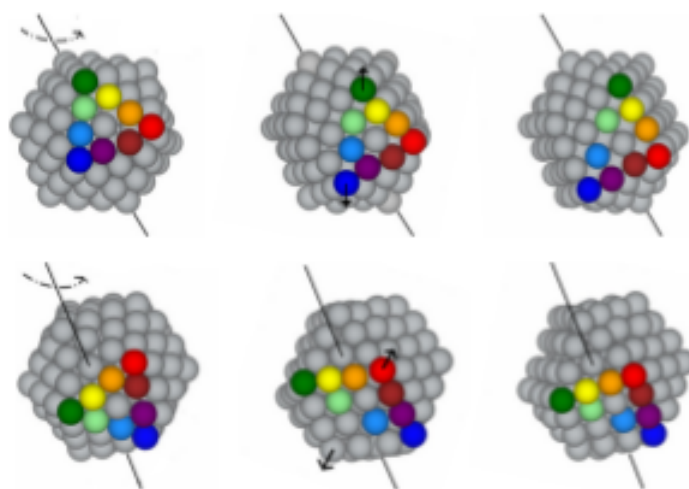


Figure 3.1 Initial, "saddle", and final configurations during a DSD rearrangement of an Ih into Dh (top) and Co (bottom). Multicolored atoms delimit a facet in the original Ih. Rotation along the depicted axis is of 36° for the Dh and of 60° for the Co. Note that the axis of rotation lies along a five-fold axis in the Dh case, so to always preserve it during the rearrangement. The rotation axis instead lies along two (111) facets centers for the Co case. "Reproduced from Metallic nanoparticles meet metadynamics - L. Pavan, K. Rossi, F. Baletto, The Journal of Chemical Physics 143 (18), 184304, 10 2015, with the permission of AIP Publishing."

of low-symmetry structures characterized by highly defected surfaces. An example of how surface peeling proceeds in the rearrangement of an InoDecahedron nanoparticle of 561 atoms into a more defected re-entrant penta-twinned structure is reported in Figure 3.2.

The structural transitions characterization for rearrangements starting from an Ino-Dh is summarised in Table 3.1 while the ones from a Co can be found in Table 3.2. For each chemical species and size we report: the percentage of runs sampling a Ih before the melting, $\rightarrow Ih\%$, the average temperature at which diffusionless transitions towards the Ih or surface diffusion are probed, $\overline{T_{\rightarrow Ih}}$ or $\overline{T_{\rightarrow dDh}}$, both normalized with respect to nanoparticle melting temperature, and the average of the largest C values for dynamics ending in either the Ih or X, X = Dh, Co basins, $\overline{C_{\rightarrow Ih}^{max}}$ or $\overline{C_{\rightarrow X}^{max}}$. Finally, we also report the free energy barrier for the direct X \rightarrow Ih transition, $\overline{\Delta F_{\rightarrow Ih}^*}$.

$\overline{T_{\rightarrow Ih}}$ and $\overline{\Delta F_{\rightarrow Ih}^*}$ increase while $\overline{T_{\rightarrow Dh}}$ decreases with nanoparticle size. This result can be rationalized in terms of size effects: concerted mechanisms in large size nanoparticles involve more atoms, thus being increasingly expensive, while the energetic cost for adatom hopping or exchange, driving the formation of surface defect, does not depend on nanoparticle size.

Solid-solid diffusionless transitions via the DSD mechanisms from both the Dh and the Co minima to the Ih one are observed in all the systems of 55 atoms, in each of the runs performed. A visual example and quantitative characterization of the transition for the case of an Ag₅₅ nanoparticle can be found in Figure 3.3: the rearrangement happens in a single step, with quasi-intermediate configurations presenting a characteristic diamond-like facets. For a quantitative analysis of the process at stake it is useful to probe the evolution of the CNA (555) and (200) during the rearrangement. The first moves between the values of perfect structures (1.8 to 10.3), the latter is always null. The instantaneous concerted rearrangement corresponds to a peak in the value of H and C at the time for which the transition took place. The martensitic character of the transformation is evident from the

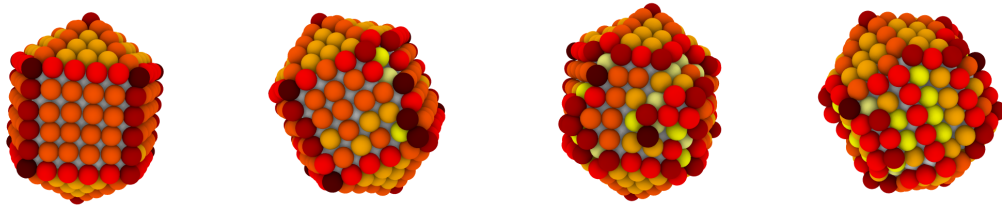


Figure 3.2 Example snapshots describing how surface peeling of a Decahedral nanostructure may proceed. Colour coding reflects atoms coordination: vertexes and adatoms are black, edges coloured are dark-red, atoms in (100) and (111) facets are red and orange respectively, atoms in re-entrances (coordination larger than 9) are yellow, bulk-like atoms are in grey.

analysis of the coordination number distributions before and after the transition, with no atom with coordination 11, 10 or < 4 observed. MetaD runs for 55 atoms nanoparticles sample diffusively the Dh, Co, and Ih basins before exploring a series of low-symmetry structures. The $\overline{\Delta F}$ for the Dh \rightarrow Ih (Ih \rightarrow Dh) transition in 55 atoms clusters is in the order of the 0.15 (1.25) eV, a magnitude comparable with previous results for potential energy surfaces[100], thus highlighting the small temperature dependence of the barriers associated to the DSD mechanism, as reported also in Ref.[101].

Following the formation of the Ih structure, the atoms at the edges display a rather fluctuating coordination, between 7 and 8, with a diminishing amount of atoms coordinated seven, for increasingly high temperatures. We remark that this is not because of the formation of a (100) facet, but due to the broadening of the peaks in the pair distribution function and the choice of a rigid-cut off to estimate the (integer) number of neighbours. We further highlight the nucleation of several surface defects just before the nanoparticle melting. In particular, rosette defects [102] are likely at high temperatures, implying that they are entropically favourable.

Both for an initial Dh or Co structure, rearrangements to the Ih basin via the DSD mechanism are observed in all the 147 atoms systems, apart for Au nanoparticles. During the transition, the (555) CNA signature shifts to the Ih ideal value, the (200) signature occurrence is constantly null, while the coordination number distributions do not display low coordinated atoms ($CN_i < 5$), or defects at the surface ($CN_i=10,11$). Indeed, H and C spike towards values near to 1 at the transition. The barrier for the rearrangement (~ 0.15 eV for 55 atoms clusters, 0.5-1.5 eV for 147 ones) is comparable to the one of adatom diffusion via hopping on an homoatomic (100) surface (0.37-0.88 eV [103]). The former transition however generally leads to much more energetically favourable structures. Defects in the surface of the Ih arise before the melting of the 147 atoms clusters.

For the Au₁₄₇ case, only transitions towards low-symmetry same-archetype structures are observed in itMD simulations. Surface defects formation corresponds to an increase in low-coordinated atoms and (200) CNA signatures pairs. Similarly, H increases with temperature, yet, C does not display any net trend, with spikes to a maximum value of 0.2, just before the melting transition, after which it drops to 0. The number of atoms along the 5-fold axis remains constant when the Ino-Dh structure rearranges towards another one, more similar to a Marks-Dh: the Ino-Dh (100) square facets become defected while (110) re-entrances form. We note that during MetaD simulations, Au₁₄₇ Ino-Dh and Co still display a transition towards an Ih shape, although defected, after the initial nucleation of few defects on the surface of the cluster. The rearrangement mechanism involves a DSD-like transition of the inner shell which propagates to the defected surface, as shown by the jump around 0.4

of the C index. The defected Ih structures generally display a 6-fold ring around one or more vertexes, i.e. a rosette defect, and surface adatoms. Accordingly, the (555) CNA signature

Table 3.1 Recap of data gathered for rearrangement of an initial Dh structure. Per each system (leftmost column) we report $\rightarrow \text{Ih}$ %, the $\overline{C_{\rightarrow \text{Ih}}^{\text{max}}}$ and $\overline{T_{\rightarrow \text{Ih}}}$, or, $\overline{C_{T \rightarrow \text{dDh}}^{\text{max}}}$ and $\overline{T_{\rightarrow \text{dDh}}}$, for simulations ending respectively in the Ih or defected-Dh (dDh) funnel as found via itMD. $\overline{T_{\rightarrow \text{Ih}}}$ and $\overline{T_{\rightarrow \text{dDh}}}$ are normalized over the corresponding nanoparticle melting temperature. The error on $\overline{C_{\rightarrow \text{Ih}}^{\text{max}}}$, $\overline{C_{\rightarrow \text{dDh}}^{\text{max}}}$, $\overline{T_{\rightarrow \text{Ih}}}$, and $\overline{T_{\rightarrow \text{dDh}}}$ is taken as the maximum deviation of their estimate, from each single independent run, with respect to the corresponding average value. It is around 0.1 for the concertedness index and of 0.03 for the characteristic transition temperatures. Rightmost column reports $\overline{\Delta F_{\rightarrow \text{Ih}}}$, and $\overline{\Delta F_{\rightarrow \text{dDh}}}$ in bracket if observed. Error on $\overline{\Delta F}$ as found from simulations sampling both basins can heuristically considered as the height of one deposited Gaussian. In the other cases the reported value represents an overestimate, and thus an upper bound of the true free energy barrier.

System	$\rightarrow \text{Ih}$	$\overline{C_{\rightarrow \text{Ih}}^{\text{max}}}$	$\overline{T_{\rightarrow \text{Ih}}}$	$\overline{C_{\rightarrow \text{dDh}}^{\text{max}}}$	$\overline{T_{\rightarrow \text{dDh}}}$	$\overline{\Delta F_{\rightarrow \text{Ih}}} \text{ (eV)}$
Ni ₅₅	100	0.9	< 0.02			0.05(1.25)
Ni ₁₄₇	100	0.7	0.37			0.2
Ni ₃₀₉	38	0.2	0.85	0.3	0.37	0.6
Ni ₅₆₁	0			0.2	0.33	1.3
Pd ₅₅	100	0.7	0.20			0.05(1.4)
Pd ₁₄₇	100	0.7	0.55			0.9
Pd ₃₀₉	0			0.2	0.57	3.8
Pd ₅₆₁	0			0.2	0.52	
Pt ₅₅	100	0.7	0.36			0.3(1.3)
Pt ₁₄₇	100	0.7	0.58			1.9
Pt ₃₀₉	0			0.2	0.57	7.4
Pt ₅₆₁	0			0.2	0.45	
Cu ₅₅	100	1.0	< 0.02			<0.05(1.3)
Cu ₁₄₇	100	1.0	< 0.02			0.2
Cu ₃₀₉	100	0.6	0.24			0.6
Cu ₅₆₁	100	0.4	0.61			1.3
Ag ₅₅	100	0.7	0.19			0.05(1.4)
Ag ₁₄₇	100	0.6	0.51			0.6(4.3)
Ag ₃₀₉	0			0.2	0.55	3.7
Ag ₅₆₁	0			0.2	0.50	
Au ₅₅	100	0.7	0.43			0.05(0.9)
Au ₁₄₇	0			0.4	0.52	0.5
Au ₃₀₉	0			0.2	0.48	
Au ₅₆₁	0			0.1	0.42	

Table 3.2 Recap of data gathered for rearrangement of an initial Dh structure. Per each system (leftmost column) we report $\rightarrow \text{Ih}$ %, the $\overline{C_{\rightarrow \text{Ih}}^{\text{max}}}$ and $\overline{T_{\rightarrow \text{Ih}}}$, or, $\overline{C_{\rightarrow d\text{FCC}}^{\text{max}}}$ and $\overline{T_{\rightarrow d\text{FCC}}}$, for simulations ending respectively in the Ih or defected FCC funnel. $\overline{T_{\rightarrow \text{Ih}}}$ and $\overline{T_{\rightarrow d\text{Dh}}}$ are normalized over the corresponding nanoparticle melting temperature. The error on $\overline{C_{\rightarrow \text{Ih}}^{\text{max}}}$, $\overline{C_{\rightarrow d\text{FCC}}^{\text{max}}}$, $\overline{T_{\rightarrow \text{Ih}}}$, and $\overline{T_{\rightarrow d\text{FCC}}}$ is taken as the maximum deviation of their estimate, from each single independent run, with respect to the corresponding average value. It is around 0.1 for the concertedness index and of 0.03 for the characteristic transition temperatures. Rightmost column reports $\overline{\Delta F_{\rightarrow \text{Ih}}}$, and $\overline{\Delta F_{\rightarrow \text{FCC}}}$ in bracket if observed. Error on $\overline{\Delta F}$ as found from simulations sampling both basins can heuristically considered as the height of one deposited Gaussian. In the other cases the reported value represents an overestimate, and thus an upper bound of the true free energy barrier.

System	$\rightarrow \text{Ih}$	$\overline{C_{\rightarrow \text{Ih}}^{\text{max}}}$	$\overline{T_{\rightarrow \text{Ih}}}$	$\overline{C_{\rightarrow d\text{Dh}}^{\text{max}}}$	$\overline{T_{\rightarrow d\text{Dh}}}$	$\overline{\Delta F_{\rightarrow \text{Ih}}}$ (eV)
Ni ₅₅	100	1.0	< 0.02			<0.05
Ni ₁₄₇	100	0.9	0.38			0.1(3.5)
Ni ₃₀₉	62	0.6	0.62	0.2	0.34	0.3
Ni ₅₆₁	0			0.2	0.45	0.7
Pd ₅₅	100	1.0	0.23			0.05
Pd ₁₄₇	100	0.9	0.60			0.5(3.0)
Pd ₃₀₉	0			0.3	0.58	3.7
Pd ₅₆₁	0			0.2	0.48	
Pt ₅₅	100	1.0	0.39			0.25
Pt ₁₄₇	100	0.8	0.55			1.7
Pt ₃₀₉	0			0.3	0.49	
Pt ₅₆₁	0			0.2	0.42	
Cu ₅₅	100	1.0	< 0.02			<0.05
Cu ₁₄₇	100	1.0	< 0.02			0.1
Cu ₃₀₉	100	1.0	< 0.02			0.3
Cu ₅₆₁	100	0.8	0.33			0.7
Ag ₅₅	100	0.9	< 0.02			<0.05
Ag ₁₄₇	100	0.8	0.47			0.4(3.2)
Ag ₃₀₉	0			0.3	0.57	2.5
Ag ₅₆₁	0			0.2	0.51	
Au ₅₅	100	0.9	0.40			<0.05
Au ₁₄₇	0			0.3	0.61	0.5
Au ₃₀₉	0			0.2	0.50	
Au ₅₆₁	0			0.1	0.41	

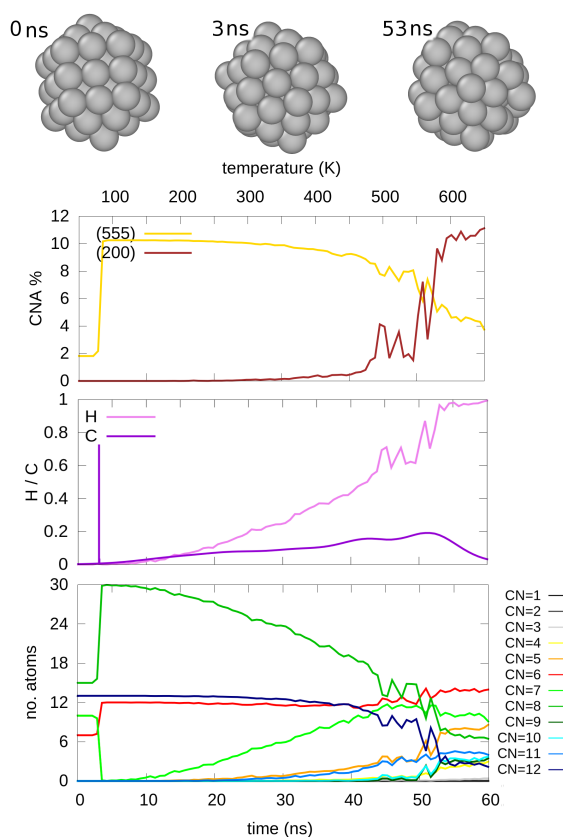


Figure 3.3 Structure and rearrangement characterization for a Dh to Ih transition in Ag₅₅ sampled by itMD. The top panel displays snapshots of representative structures observed during the simulation and the corresponding time at which they are first formed. Lower panels show the evolution of the (555) and (200) CNA signature percentages, H and C , respectively the collectivity and concertedness indexes, and coordination number distributions during the course of the simulation. Reproduced from The effect of size and composition on structural transitions in monometallic nanoparticles - K. Rossi, L. Pavan, Y.Y. Soon, F. Baletto, The European Physical Journal B 91 (2), 33, 3, 2018 under Creative Commons Attribution 4.0 International License.

is slightly lower with respect to the value of the perfect Ih and some 10 and 11 coordinated atoms are detected.

Martensitic transitions towards the Ih are not observed in 309 and 561 atoms nanoclusters during itMD simulation, apart for the case of Ni₃₀₉, Cu₃₀₉, and Cu₅₆₁. This result is in agreement with previous studies employing similar parametrizations of the metal-metal interactions and temperature change heating rates. [41, 104] Adatom hopping and exchanges from edges and corners to facets drive the reconstruction of the Dh and Co motifs towards their low-symmetry counterparts. In Figure 3.4 we report the structural and rearrangement

characterization for the selected case of an Ag_{561} with an initial Ino-Dh structure, which rearranges towards a defected Marks-Dh one. The cluster surface is rather mobile as evident from the continuous non monotonic changes in the cluster CNA signature percentages and coordination number distributions. H shows a positive correlation with the temperature of the system, while C always displays relatively low values, indicating a lack of concertedness in the rearrangements at stake. The constant number of pairs with a (5,5,5) CNA signature demonstrates that the clusters not only maintain the number of 5-fold axis in the architecture but also the original number of atoms along them. Defects at the surface increase with temperature, as signalled an increase in the (2,0,0) signature percentage and the number of low coordinated atoms. An entropic argument can be evoked to rationalise this behaviour, as well as considering the probability for adatom diffusion on low-Miller index surfaces at high temperatures.

A diffusionless transition from an initial Dh and Co morphology towards an Ih is still observed for Cu_{309} and Cu_{561} during both itMD and MetaD sampling. The rearrangements, although being screw-dislocation motions, happen layer-by-layer. The two-steps in the transitions are evident when looking at the intermediate configurations sampled between the perfect geometries. They presents a mixture of (100) and (111) facets, as identified from the presence of both 6 and 5 coordinated vertexes and by a (555) CNA signature percentage in between the one of the ideal Dh, Co, or the Ih ones. Similarly, H and C display a value near 0.5 at the two rearrangements steps (3.5).

We note that during the MetaD sampling of the rearrangements in Ni_{309} the transitions from an Idh to an Ih take place similarly to what observed in Au_{147} . After the nucleation of surface defects a DSD rearrangement in the inner shells of the nanocluster brings the system in the Ih minimum.

During MetaD sampling, rearrangements to and from the Ih minimum via layer-by-layer DSD mechanism, for clusters of 309 and 561 atoms, are observed not only in Cu clusters but also for Ni, Pd, Pt, and Ag, notwithstanding the competition with surface peeling and defects formation. We note that the larger size at which MetaD samples concerted rearrangements is bigger than the itMD one. It is worth to recall here the difference between the two methods: MetaD energy landscape exploration happens at fixed temperature, while itMD sampling may hide possible structural transition if the temperature is rescaled at a too fast rate. Our results hence suggest a competition between concerted rearrangements and surface diffusion ones in sizes close to the crossover one.

It is finally intriguing to discuss the material dependence of the size ranges where concerted mechanisms have been sampled, and hence deemed likely to happen. A striking correspondence between the lower energetic structures and the mechanisms crossovers sizes

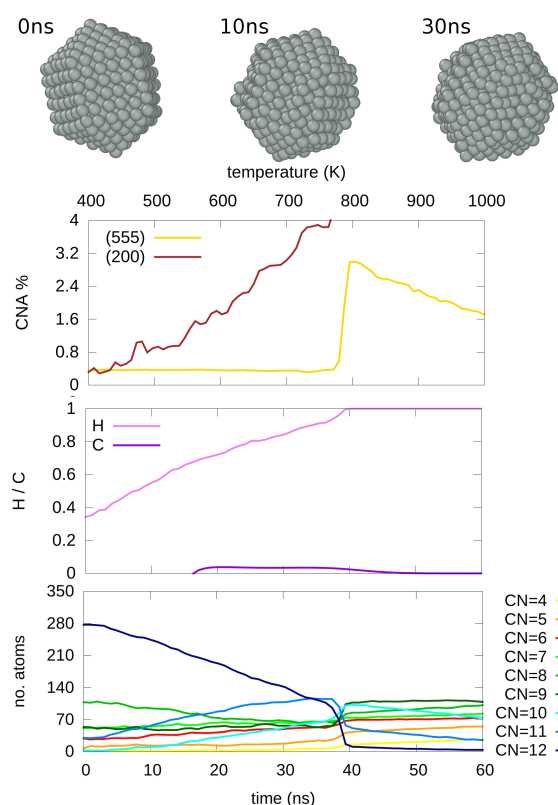


Figure 3.4 Structure and rearrangement characterization for a Dh to defected Dh transition in Ag₅₆₁ sampled by itMD. Panel ordering follows what described in Figure 3.3. Reproduced from The effect of size and composition on structural transitions in monometallic nanoparticles - K. Rossi, L. Pavan, Y.Y. Soon, F. Baletto, The European Physical Journal B 91 (2), 33, 3, 2018 under Creative Commons Attribution 4.0 International License.

emerges. Concerted rearrangements are hindered, if not forbidden at all, in Ni, Ag, and Pd clusters larger than 561 atoms, Pt clusters with size above 309 atoms, and in Au clusters with a nuclearity higher than 147. For Cu clusters, the crossover size is expected above the one here considered, as a layer-by-layer screw dislocation motion is still observed in clusters of 561 atoms. This result finds a parallelism with the structural crossover sizes for Ih and Dh morphologies. As first highlighted in [105] twinned re-entrant structures are favourable for Au or Pt clusters as small as 100 atoms, for Ag, Ni, and Pd clusters of size above 300 atoms, and for Cu nanoparticles with 1000 atoms or more. Our data thus highlight that softer interatomic potentials, as the one for copper-copper interaction, not only favours Ih structures in a larger size range but also concerted motions towards this basin, opposite to what found for elements which present a more stiff homoatomic interaction, e.g., gold.

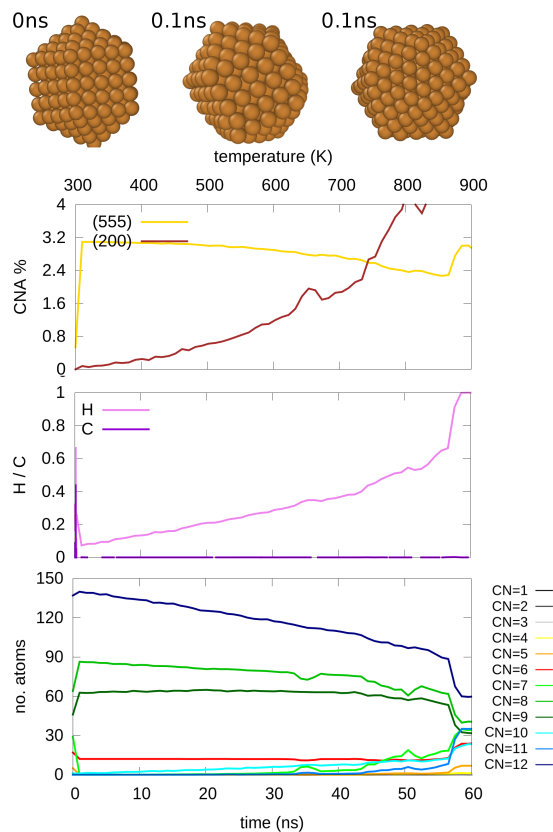


Figure 3.5 Structure and rearrangement characterization for a Dh to Ih transition in Cu₃₀₉ sampled by itMD. Panel ordering follows what described in Figure 3.3. The transition happens after just few tens of ps from the start of the sampling.

3.2 Concerted rearrangement in supported nanoparticles

Structural transitions via concerted mechanisms can be observed also in nanoparticles supported on an oxide. However, the symmetry breaking dictated by the substrate implies that concerted rearrangements via screw dislocation motion can happen, most likely, only parallel to the substrate. Conversely, they will not involve the whole set of atoms in the nanoparticles (as it was the case for the Diamond-Square-Diamond mechanism). In turn, they may be observed also in systems larger than the one discussed in Section 3.1.2.

Let us here discuss the case of a Pt₅₆₁ nanoparticle with an initial Ih morphology, soft landed on a (100) terminated MgO oxide.

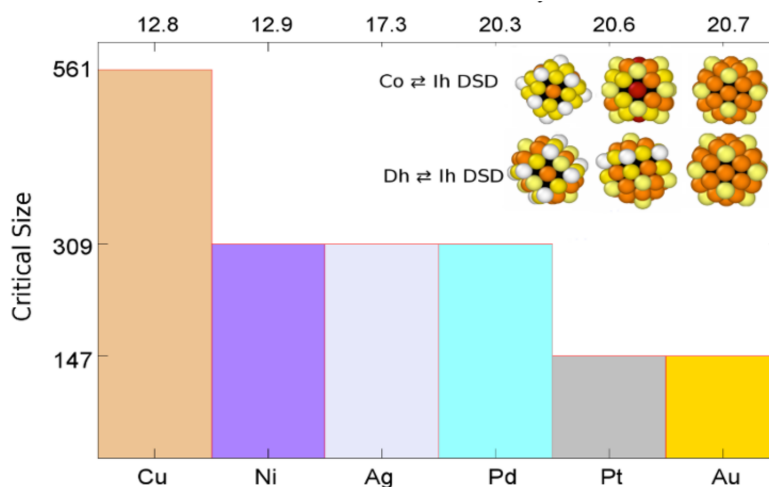


Figure 3.6 Resume of the largest sizes at which rearrangements via DSD mechanism are observed, depending on the nanoparticle composition and interaction stickyness.

3.2.1 Computational set-up and analysis method

To investigate structural rearrangements in supported nanoparticles we adopt an iterative temperature MD scheme, where the temperature, controlled by an Andersen thermostat, is increased by 50 K every 10 ns, ensuring a heating rate as slow as 5 K/ns. After a temperature increment, the system is left free to evolve at each temperature, accordingly to Newton's equations of motion, integrated using the velocity-Verlet algorithm with a time step of 5 fs. The overall temperature range explored is 350-1500 K, although a few runs are carried out between 700-1500 K. We perform at least 7 Molecular Dynamics simulations to gather sensible statistics. Metal-Metal and Metal-support interactions are modelled according to what described in Section 2.2.

Although seven independent runs have been performed, we will here discuss the results gathered from a paradigmatic trajectory where a structural rearrangement was observed. Indeed the aim of this investigation is to qualitatively characterize the possible different rearrangement mechanisms arising from the interaction of the metallic nanoparticle with a non-inert support. We however remark that rearrangement mechanisms similar to the one discussed in the next subsection have been observed in the other runs too, as well as in systems of different size.[106]

To characterize the pre-melting structural changes we employ the CNA (555) signature and the height distribution function to enumerate the number of atoms in layers of heights multiple of 2.37\AA . This height is taken as the first peak of the pair distribution function

multiplied by $\sqrt{3}/2$, to account for the $\sim 60^\circ$ incidence angle between the five-fold axes of the Ih and the pristine MgO(100) substrate.

3.2.2 Support effects

Figure 3.7 upper panel reports the system excess energy evolution with temperature. Two drops are evident. The first one corresponds to a structural rearrangement in the interface layer, which undergoes a transition towards a (100) arrangement via a concerted mechanism. While the nanoparticle lower layer takes a squared morphology, the rest of the system maintains its original Ih arrangement. The second drop happens because of the formation of a crystalline architecture. The non continuous transition from non-crystalline to crystalline morphologies has been also detected experimentally in similar systems, corroborating the robustness of the potentials employed in the simulation. [107]

From Figure 3.7, we can also infer the stability of the initial icosahedral structure up to 650 K from the constant number of (555) CNA signatures observed. After soft landing on the MgO (100) surface, Figure 3.7 first snapshot, the lowermost layer is made of ~ 20 atoms, the second layer by ~ 30 , with similar increases in the number of atoms in the subsequent above layers, until the sixth. This is the most populated one and encompasses ~ 75 atoms. By symmetry, the number of atoms in the upper layers decreases after the sixth. The initial Pt₅₆₁ Ih nanoparticle presents a total of 11 layers, (i.e. the number of atoms on each 5-fold axis) and the contact angles between the incident facets and the oxide support are acute.

In the 650-700 K temperature range, the interface layer rearranges to match the O-sites of the oxide support. This rearrangement corresponds to a net decrease of the (555) signatures. Hence, adatom diffusion drives the population of the first three layers at the expense of the five upper ones. Simultaneously the interface layer presents an almost square shape. Around ~ 750 K a hybrid morphology of the nanoparticle, presenting (100) square lowermost layers and twinned upper layers, is observed. Just before 950 K, the remaining 5-fold symmetry axes in the nanoparticle disappear, i.e. an Ih \rightarrow fcc transition completes. We note that, previous to this final-step, the lower layers of the nanoparticle continued their growth at the expense of the upper ones. Up to 1100 K the newly observed crystalline morphology is stable, with only few surface adatom diffusion steps observed, as well as nanoparticle surface reconstructions towards the formation of more favourable truncations of its facets. Above 1250 K the first three layers increase their population. While the first encompasses 50 atoms, the others present almost 100 units. Around 1300 K, we note that the second layer becomes the more populated one, implying a significant change in the wetting angle of the nanoparticle with the substrate.

3.3 Summary

In this chapter solid-solid structural transitions in noble and quasi-noble magic-size monometallic clusters of 0.5-2.0 nm have been investigated. A special focus was paid to investigate whether they are more likely to be concerted or characterized by surface diffusion, and how size and chemical composition effects determine such result. Concerted diffusionless rearrangements connecting two different archetypical morphologies are observed only below a critical size. Above, surface peeling and surface defects nucleation were observed to dominate and drive ideal to defected structure rearrangements. The stiffness of the interatomic interaction in monometallic nanoparticle was found to correlate with the probability of observing surface diffusion driven rearrangements at relatively small sizes.

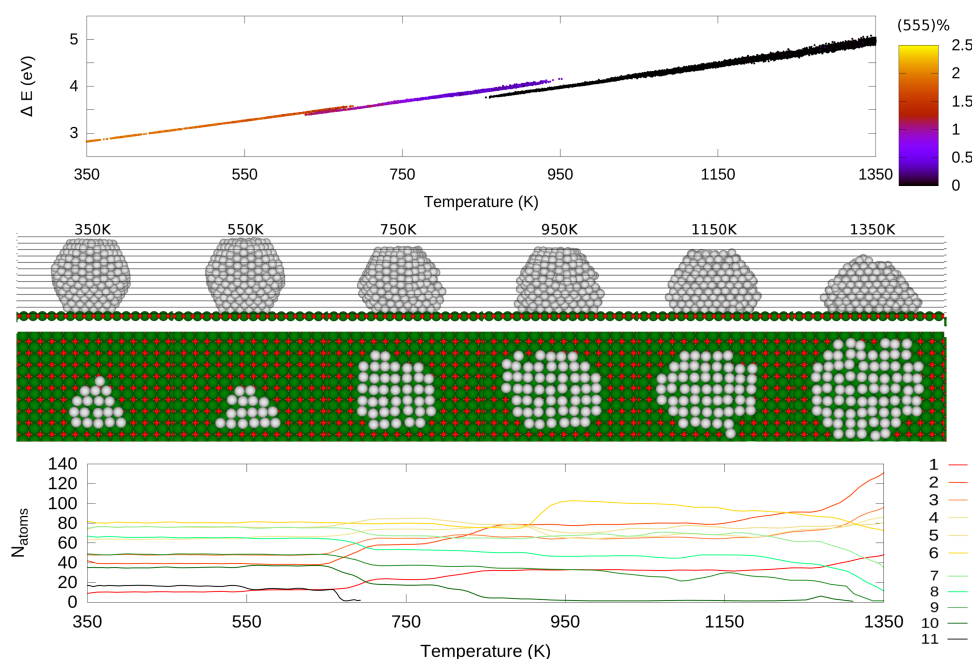


Figure 3.7 Top panel reports the caloric curve for the melting of a Pt_{561} nanoparticle on $\text{MgO}(100)$. Colour coding reports the nanoparticle (555) CNA signatures percentage (hot colours for 5-fold twinned structures, dark for crystalline ones). Mid panel shows snapshots of the system during its dynamical evolution. Pt atoms are in grey, Mg in green and O in red. The thin lines show the binning in height-distribution function. Lower panel displays the evolution of the number of atoms in each layer, layer 1 being the lowermost. Reproduced with Permission from Melting of large $\text{Pt@MgO}(100)$ icosahedra - K. Rossi, T. Ellaby, L.O. Paz-Borbón, I. Atanasov, L. Pavan, F. Baletto, *Journal of Physics: Condensed Matter* 29 (14), 145402, 10, 2017.

The paradigms inferred from gas phase nanoparticle demonstrated to be transferable to the supported case. Indeed the symmetry breaking dictated by the presence of a substrate hinders concerted rearrangements comprising screw dislocation in a 3D space, but favours the one happening parallel to the substrate. Conversely, also for the case of a system with size above the critical one observed for nanoparticles, e.g. Pt₅₆₁, concerted rearrangements of atomic layers drive the rearrangement from an Ih morphology to a more favourable crystalline one, whose interface layer matches the oxide (100) termination.

Chapter 4

On concerted rearrangements in bimetallic nanoparticles

After the in depth discussion of size and chemical composition effects on concerted rearrangements in monometallic systems it is natural and stimulating to assess how the presence of two chemical species in a nanoalloy introduces constraints on the feasibility of concerted structural rearrangements from one archetypical structural basin to another.

We consider (putative [6]) magic size bimetallic nanoalloys of 147 atoms, as monometallic group X and XI elements nanoparticles showed concerted diffusionless rearrangements at these sizes. For core@shell nanoparticles we investigate $M@Ag$, $M=Au, Cu, Pt$ systems with a one layer-thick silver outer shell. This is their favourable chemical ordering from an energetic perspective. For the case of AgAu nanoparticles we also probe rearrangements in $Ag@Au$ structures. To sample rearrangements in Janus nanoalloys we instead focus on AgPt and AgCu because of their higher tendency to segregate in the bulk. We consider structures where the metal-metal interface is described by a cut along the (100) facet for Co structures, and perpendicular to the five-fold axis for Idh architectures. We remark that a Janus chemical ordering is expected to be the energetically favourable one in these AgPt and AgCu nanoalloys at sizes larger than the one here considered.

4.1 Computational set-up and analysis method

To investigate structural transitions in the chosen systems we analyze results via MetaD and compare them with those found by either itMD or double ended transition path sampling depending on the complexity of the rearrangement we want to probe. During MetaD runs, we sample the system at 300K and employ the PDF CVs to promote concerted structural

transitions, sliding of (111) planes, breathing, and distortions. When transition path sampling data are reported as a term of comparison with MetaD estimates of energetic barriers for target rearrangements, calculations have been carried on by Dr. Anna Gould (University College London) and Dr. Andrew Logsdail (University College London, now Cardiff University).

We run up to eight independent MetaD and itMD simulations for each system. We perform the CNA of the whole nanoparticle and its core. For the case of chemical reordering, we further probe the nanoalloy mixing and chemical radii of gyration to measure the degree of alloying or separation of the two chemical species (see Section 2.4). Structural rearrangements are further analysed in terms of the chemical informed adjacency matrix evolution order parameters (see Section 2.8). The reported Free Energy Barriers are taken as the average of the ones estimated in each independent MetaD simulation. When a temperature label is shown on the graph, it refers to itMD simulations where the temperature of the system is increased, starting from an initial one of 100 K, by 50 K every 1 ns.

4.2 Mismatch effects

Geometric considerations about closed-packed non-interacting hard ball systems first proposed by Mackay promoted the discovery of the Diamond-Square-Diamond mechanism. Within the same framework (hard spheres), the presence in the system of two chemical species presenting a large mismatch may suggest that the latter can strongly affect the accessible rearrangement kinetics by hindering concerted screw dislocation mechanisms. We thus here analyse the case of M@Ag, M=Au (subsection 4.2), Pt (subsection 4.2), Cu (subsection 4.2) systems.

Small mismatch

As illustrated in Figure 4.1 Ih \leftrightarrow Co and Ih \leftrightarrow Dh transitions via concerted diffusionless screw dislocation, identical to the monometallic cases discussed in Chapter 3, take place in core-shell systems where chemical species present a small mismatch, i.e. Au₅₅@Ag₉₂ and Pt₅₅@Ag₉₂. The (100) facets of the Co or IDh first distort into a (111) diamond, which, following a concerted rotation, become two distinct and adjoint (111) facets, corresponding to the new Ih geometry of the nanoparticle. The inverse transition, although more costly from an energetic perspective, is also sampled. The free energy barriers for the Co \rightarrow Ih (Co \leftarrow Ih) transitions is of 0.25 eV (3.6 eV) for the AgPt nanoalloy and 0.55 eV (2.55 eV) for the AgAu one. A slight overlap between the AgPt Ih and Dh geometries during the MetaD simulation arises due to the sampling of intermediate defected structures and the presence of a non negligible mismatch between the two chemical species in the nanoalloy. We heuristically

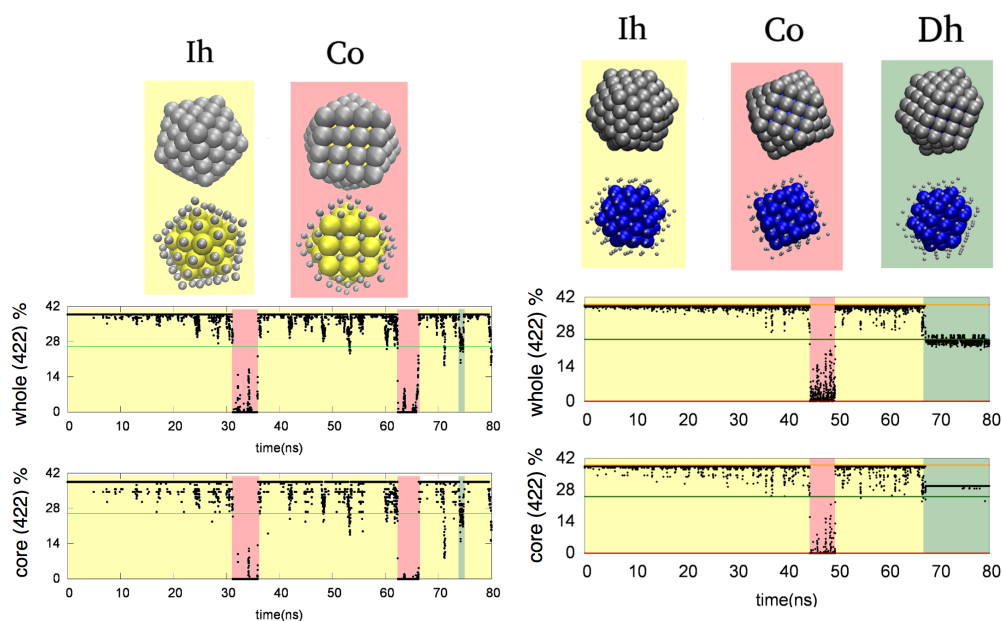


Figure 4.1 (422) CNA signature, in %, of the whole nanoparticle (top) and the 55-atoms core (bottom) for $\text{Au}_{55}@\text{Ag}_{92}$ (left) and $\text{Pt}_{55}@\text{Ag}_{92}$ (right) during the course of MetaD runs at 300K. Reference values for ideal Ih, Dh, and Co geometries are shown via a straight gold, green and red line. When Ih, Dh and Co geometries are sampled, the plot is highlighted in yellow, dark-green or pink. A representative snapshot for each of the above mentioned geometries is reported. Au atoms are in gold, Ag atoms are in silver, Pt atoms are in blue. Left Panel image is partially edited from Controlling Structural Transitions in AuAg Nanoparticles through Precise Compositional Design - A.L. Gould, K. Rossi, C.R.A. Catlow, F. Baletto, A.J. Logsdail, *The Journal of Physical Chemistry Letters* 7 (21), 4414-4419, 7, 2016 <<https://pubs.acs.org/doi/10.1021/acs.jpclett.6b02181>>, further permissions related to the material excerpted should be directed to ACS. Right panel image is reproduced from Ref. The effect of chemical ordering and lattice mismatch on structural transitions in phase segregating nanoalloys - K. Rossi, F. Baletto, *Physical Chemistry Chemical Physics* 19 (18), 11057-11063, 5, 2017 - Themed collections: 2017 PCCP HOT articles with permission from the PCCP Owner Societies.

determine an upper bound on the barriers dividing the two geometries, 1.5 eV (4.3 eV) for the $\text{Dh} \rightarrow \text{Ih}$ ($\text{Ih} \leftarrow \text{Dh}$) transition, by summing up the amount of MetaD potential needed to escape the initial Dh (Ih) basin.

Large mismatch

A different transition pathway is observed in $\text{Cu}_{55}@\text{Ag}_{92}$: the geometric constraints imposed by the mismatch between Ag and Cu undermine full concerted screw dislocation motions in the nanoparticle outer shell. As reported in Figure 4.2, the (4,2,2) CNA signature of the

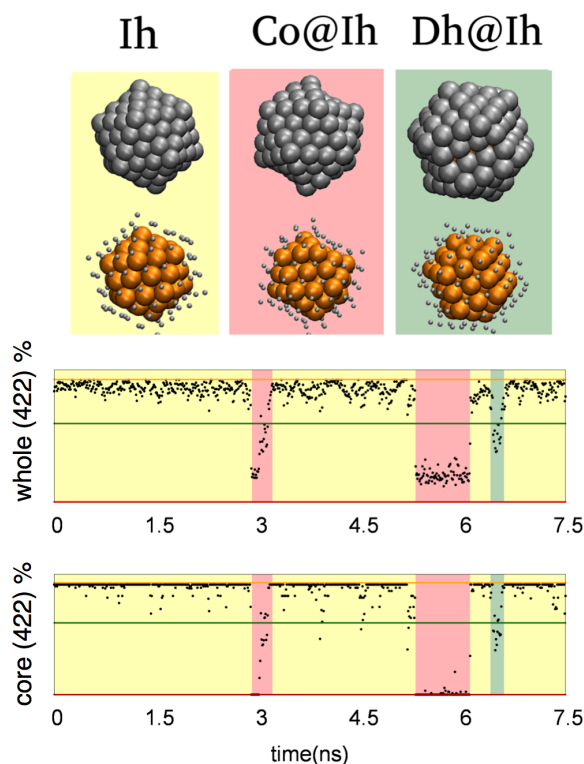


Figure 4.2 (422) CNA signature, in %, of the whole nanoparticle (top) and the 55-atoms core (bottom) for Cu₅₅@Ag₉₂ during the course of MetaD runs at 300K. Reference values for ideal Ih, Dh, and Co geometries are shown via a straight gold, green and red line. When Ih, Dh, and Co geometries are sampled, the plot is highlighted in yellow, dark-green, and pink. A representative snapshot for each of the above mentioned geometries is reported. Cu atoms are in copper, Ag atoms are in silver. Image is reproduced from Ref. The effect of chemical ordering and lattice mismatch on structural transitions in phase segregating nanoalloys - K. Rossi, F. Baletto, *Physical Chemistry Chemical Physics* 19 (18), 11057-11063, 5, 2017 - Themed collections: 2017 PCCP HOT articles with permission from the PCCP Owner Societies.

whole nanoparticle does not match the one of perfect Dh and Co nanoparticles, while the one for the Cu₅₅ core shows that it actually presents an ideal Dh and Co geometry.

Indeed the Cu core undergoes a clear Ih → Dh or Ih → Co transition by a screw dislocation motion. This rearrangement is however hindered in the external Ag shell which displays 5-fold twins and distorted concave (111) facets. The arrangement of the Ag skin is reminiscent of the one observed for non-perfect chiral shells in AgCu nanoalloy of different size [77] and affine to the shell-wise Mackay transformations first reported in Fe₅₆₁ large-scale DFT optimization.[108] Energetically, the Dh@Ih and Co@Ih structures are a few eV more favourable than the perfect Dh and Co structures while the Cu inner core transition

is characterized by barriers as low as 0.1 eV, similarly to the one found in the case of monometallic systems of the same size (55 atoms),[109] implying a weak significance of the Ag outer shell in determining the rearrangement kinetics and barriers of the inner core.

4.3 Chemical ordering effects

Also the initial chemical ordering of the nanoalloy can strongly affect the accessible rearrangement pathways for transitions between archetypical structural basins.

Janus nanoparticles

To discuss the chemical ordering effect for phase segregating nanoalloys, we report on the transition from Janus Co and Dh geometries towards a Janus Ih, in AgCu nanoalloys. In these systems, the rearrangement mechanisms are the same of the one observed for AgPt Janus nanoparticles, hinting to a negligible role of the mismatch in the here discussed systems. We note that geometrical reconstructions towards the Ih, a more energetically favourable structure, always precede chemical reordering.

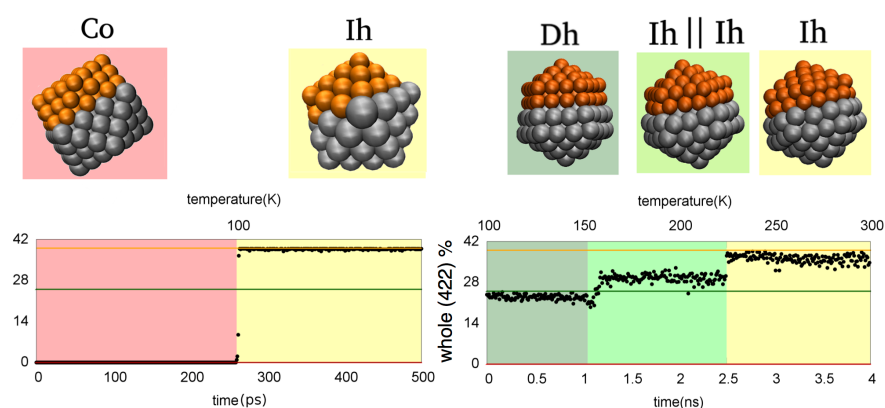


Figure 4.3 (422) CNA signature %, in Cu|Ag nanoparticles during the course of itMD runs. Note the two different timescales reported (0.5 ns for the Co→Ih transition, and 4 ns for the Dh→Ih case.) Reference values for ideal Ih, Dh, and Co geometries are shown via a straight gold, green and red line. When Ih, Ih|Dh, Dh and Co geometries are sampled, the plot is highlighted in yellow, light-green, dark-green or pink. A representative snapshot for each of the above mentioned geometries is reported. Cu atoms are in copper, Ag atoms are in silver. Image is reproduced from Ref. The effect of chemical ordering and lattice mismatch on structural transitions in phase segregating nanoalloys - K. Rossi, F. Baletto, *Physical Chemistry Chemical Physics* 19 (18), 11057-11063, 5, 2017 - Themed collections: 2017 PCCP HOT articles with permission from the PCCP Owner Societies.

The Co \rightarrow Ih transition takes place through the twisting and the stretching of the (100) square facets with the axis of the rotation crossing the center of the triangular facets. The DSD mechanism leads to the splitting of the two mixed square (100) facets in four mixed triangular (111) facets (Figure 4.3 left). In structures with an initial Dh geometry, where the metal-metal interface crosses the (100) facets perpendicular to the 5-fold axis, we sample a new mechanism. The latter interface is in fact fixed during the rearrangement towards an Ih while a multi-step transition happens: first, an intermediate mis-stacked Ih||Ih morphology is formed, second, the halves undergo a DSD motion along the same 5-fold axis, but rotating in opposite directions, lastly the resulting (100) interface between silver and copper regions is formed through a rotation of one species with respect to the other to complete the formation of a Janus Ih (Figure 4.3 right).

For the case of the Co \rightarrow Ih transition, the very short time scale needed to observe the rearrangement suggests an almost null barrier in the transition pathway. This is not the case for the Dh \rightarrow Ih transition. Metadynamic sampling, after driving such rearrangement, only enhances chemical reordering, thus not allowing for an estimate of the free energy barrier between the Ih and the Co or the Dh structures.

Inverse core-shell nanoparticles

A more complex behaviour is observed for the case of the Ag@Au systems when compared to Au@Ag one, as shown by Figure 4.4. While rearrangements among the Co and the Ih basin proceed through a single-step in Au@Ag, they consist of a large number of exchanges, atomic diffusion and vacancy formation steps for the case of Ag@Au (top panels).

Interestingly, the largest barrier in the pathway (3.07 eV) is still related with a local screw dislocation that drives 5-fold axis nucleation. For the opposite rearrangement, the tallest barrier is of 3.98 eV. Because of the complexity in the rearrangements and the relative high energy of the Co morphology, barriers have been calculated by means of transition path sampling, with Metadynamics instead allowing to sample a variety of defected low energy minima in the proximity of the lowest energetic structure found by transition path sampling (see middle panel of Figure 4.4).

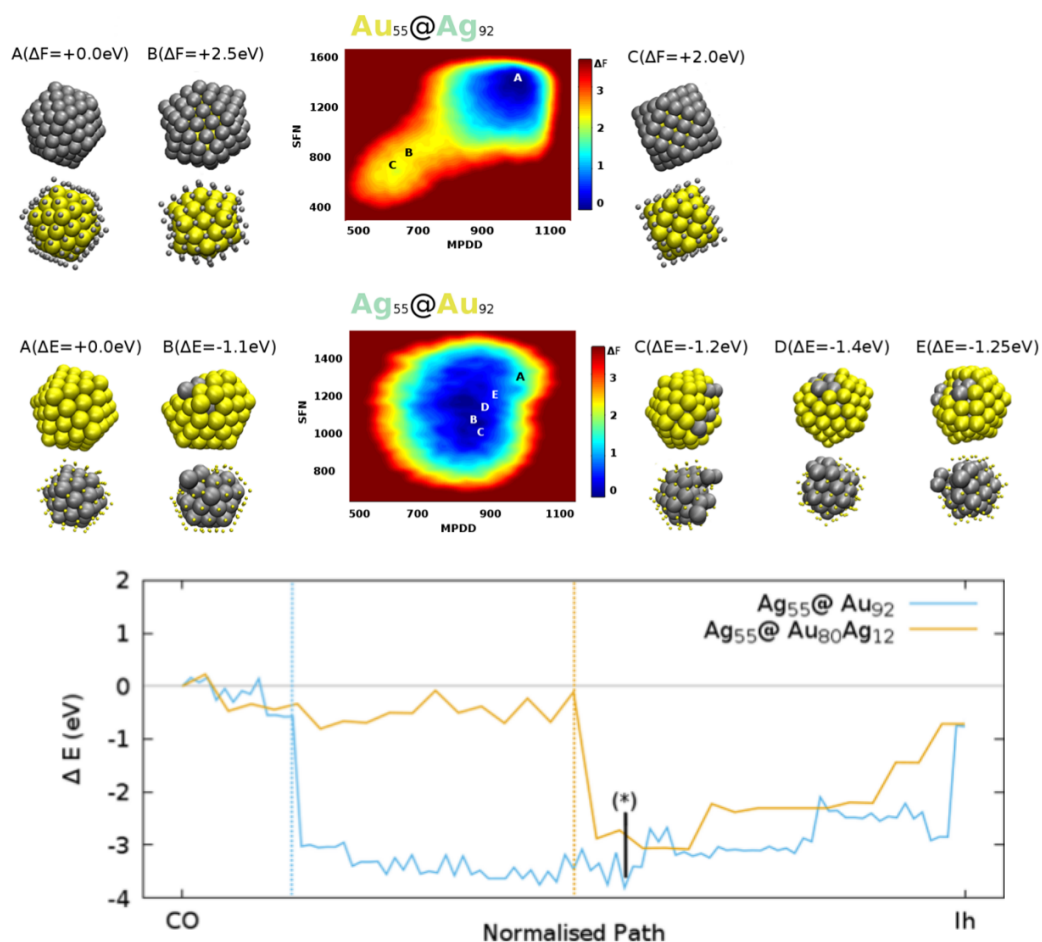


Figure 4.4 The upper panel shows the comparison between the energetic landscape sampled during MetaD simulations at 300K for $\text{Au}_{55}@\text{Ag}_{92}$ and $\text{Ag}_{55}@\text{Au}_{92}$. Landmarks are signalled with letters. The corresponding structure and its potential energy are also reported for comparison. Note how energetically favourable low symmetry Ih-like motifs are sampled only for the case of $\text{Ag}_{55}@\text{Au}_{92}$. The lower panel displays the transition pathways for $\text{Co} \leftrightarrow \text{Ih}$ in $\text{Ag}_{55}@\text{Au}_{92}$ (and $\text{Ag}_{55}@\text{Au}_{80}\text{Ag}_{12}$ for the descriptive purpose of comparing with another Au-outer-layer rich system). A vertical dashed line in each plot indicates where the transition from/to CO-like to/from Ih-like motifs occurs. The star symbol indicates the lowest energy rosette-Ih minima encountered, a rosette-defected Ih structure. image is partially edited from Controlling Structural Transitions in AuAg Nanoparticles through Precise Compositional Design - A.L. Gould, K. Rossi, C.R.A. Catlow, F. Baletto, A.J. Logsdail, The Journal of Physical Chemistry Letters 7 (21), 4414-4419, 7, 2016 <<https://pubs.acs.org/doi/10.1021/acs.jpcllett.6b02181>>, further permissions related to the material excerpted should be directed to ACS.

4.4 Chemical reordering

Diffusion rearrangements drive chemical reordering. Let us discuss the paradigmatic case of the structural and chemical rearrangements in Dh Ag₈₆||Cu₆₁. Figure 4.5 shows the evolution of the (4,2,2) CNA signature, segregation parameter μ and chemical radius of gyration G^α , as well as the evolution of H^α and R^α during the course of an itMD run starting from an Dh Ag₈₆||Cu₆₁ architecture. After the first 3 ns the earlier described Dh \leftrightarrow Ih transition takes place. The Janus-Ih is then a long-lived metastable architecture surviving up to 450 K. Above this temperature, the Ag atoms initiate disordering, surface defects emerge, and surface diffusion onto (111) facets kicks in. Just below 600 K, chemical reordering of a defected Janus into a defected shell@core architecture happens via many atomic surface and intra-cluster diffusion steps. Initially the mobility of the Cu atoms is lower with respect to the one of Ag atoms, both in the number of Cu atoms modifying their connectivity, and in the number of bonds which have been broken or formed. Above 600 K, in agreement with free energy calculations in the literature[110], a core@shell pattern is clearly formed with both Ag and Cu shells presenting an high mobility and a strong structural fluctuationality being observed.

By the use of the heteroatomic coordination number collective variable, Metadynamics can drive and sample chemical reordering transitions to substantiate the detail offered by itMD simulation. In Figure 4.6 we report the evolution of mixing parameter, μ , and chemical radii of gyration, G^{Ag} and G^{Pt} , during a 200 ns run. The initial structure is a Pt₅₅@Ag₉₂ Ih motif. Reordering of the nanoparticle inner shells are signalled by the growth of the Pt radius of gyration and by the decrease in the segregation parameter. The outer shell maintains its Ag-rich composition. The two inner shells are instead Pt-rich. Occasionally, also Ag@Pt@Ag multi-shell chemical ordering is observed in the nanoparticle (e.g., in the 140-160 ns time interval). After 170 ns, a Janus pattern is observed, as evident from the Ag and Pt radii of gyration of comparable magnitude and from the increase in the segregation parameter.

Core@shell \leftrightarrow Janus reordering takes place via surface adatom diffusion. Random \leftrightarrow core@shell instead happens via vacancy formation and intra-cluster atomic diffusion, in agreement with previous studies.[38] We remark that the two mechanisms can take place simultaneously and promote a variety of reordering transitions connecting, e.g., Janus to mixed or multi-shell to core-shell motifs.

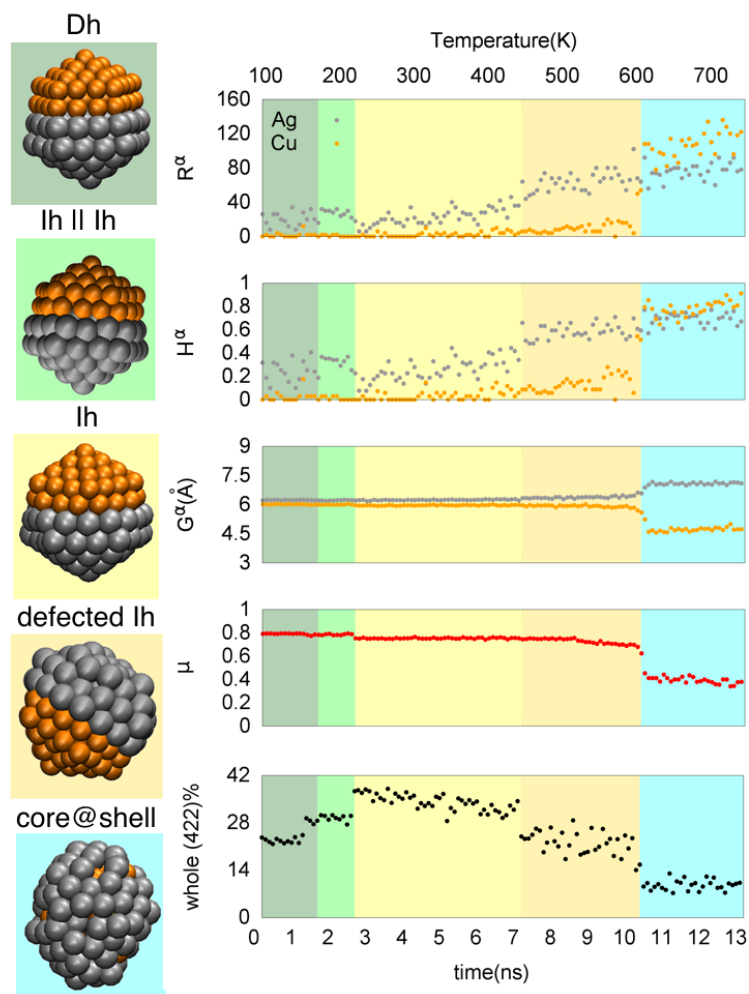


Figure 4.5 Typical snapshots during an itMD dynamics of a $\text{Ag}_{85}\text{Cu}_{62}$ Dh up to the melting. Five regions are found, shadowed by different colours, in correspondence of changes in the (4,2,2) %. The first 4 ns correspond to the one reported in Figure 4.3 right panel. μ and G^α show that the initial Janus ordering is altered only after the formation of a Ih. A core@shell ordering is completely formed only after 600 K, very close if not after the melting point. From the evolution of the R^α and H^α parameters, Ag (grey dots) is initially more mobile than Cu (orange). Ag starts to move clearly after 450 K with the formation of a defected Ih in the silver half, while the latter only above 550 K. Image is reproduced from Ref. The effect of chemical ordering and lattice mismatch on structural transitions in phase segregating nanoalloys - K. Rossi, F. Baletto, Physical Chemistry Chemical Physics 19 (18), 11057-11063, 5, 2017 - Themed collections: 2017 PCCP HOT articles with permission from the PCCP Owner Societies.

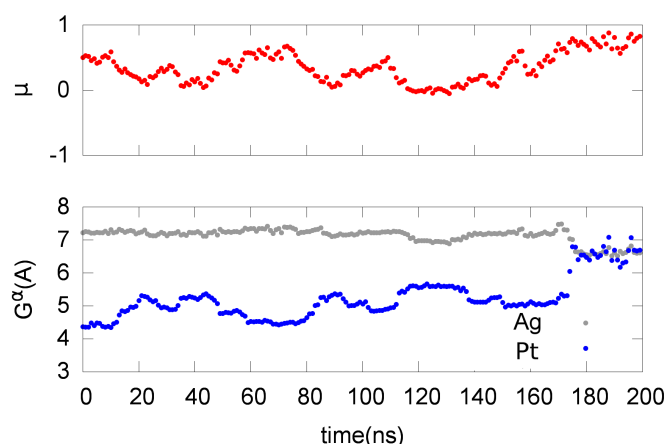


Figure 4.6 Evolution of the chemical radius of gyration (G^α) and of the segregation parameter (μ) for Ag (silver) and Pt (blue), during a HeCN driven MetaD at 300K starting from an Ih Pt₅₅@Ag₉₂ architecture. Image is reproduced from Ref. The effect of chemical ordering and lattice mismatch on structural transitions in phase segregating nanoalloys - K. Rossi, F. Baletto, *Physical Chemistry Chemical Physics* 19 (18), 11057-11063, 5, 2017 - Themed collections: 2017 PCCP HOT articles with permission from the PCCP Owner Societies.

4.5 Summary

By systematically assessing nanoalloys presenting different stoichiometries and chemical orderings we unveiled a great complexity in the characterization of the rearrangements in bimetallic nanoalloys. Our approach allowed to identify how stoichiometry, ordering, mismatch, and size permit or hinder concerted diffusionless rearrangements connecting different archetypal basins.

The Diamond-Square-Diamond [111] pathway connects Ih to Co and Dh in favourable core-shell nanoalloys when the chemical species mismatch is smaller than the 10%. An incomplete Diamond-Square-Diamond rearrangement, alike the shell-wise Mackay[108] mechanism, was observed instead in Cu@Ag nanoalloys, where the Cu core accomplishes fully its rearrangement, while the Ag skin is constrained to form convex rhombic (111) facets. In unfavourable Ag@Au core-shell nanoalloys we instead observe that the diffusionless screw dislocation pathway is unfavourable and dominated by the combination of many of local rearrangements involving few atoms and few less collective and concerted steps.

In Janus nanoalloys, the Co rearranges into an Ih via the DSD mechanism, while Dh does so in two steps: the two segregated hats first rotate around its 5-fold axis in opposite direction to form of a mis-stacked Ih, which only then adjust into a perfect Ih. Surface diffusion in the surface and inner regions of the nanoparticles drives chemical reordering, with little influence of composition and mismatch.

Our results thus also enable to establish general criteria towards predicting the persistence of favourable concerted mechanisms among different archetypical structures. Further they show how tailoring the stoichiometries and initial chemical ordering allows to tailor the energetic barriers for rearrangements among different structures, hence demonstrating a valid tool for the rational design of nanoalloys structural and, in turn, chemo-physical properties.

Chapter 5

On phase changes in metallic nanoparticles

The interplay between kinetic, entropic, and finite-size effects determines the complexity which characterizes phase changes at the nanoscale. In this chapter we demonstrate how a systematic analysis of the energetic and structural properties of nanoparticles undergoing a phase change enables to isolate the kinetic effects determining an hysteresis in the melting and freezing of a nanoparticle (Section 5.1) and the structural features which are univocally characteristic of melted or liquid phases (Section 5.2).

5.1 Kinetic effects on nanoparticle phase change

In this section we will discuss how to disentangle the kinetic and thermodynamic contributions determining the presence of an hysteresis in the freezing and the melting of a nanoparticle. As a case study we investigate the solid-liquid and liquid-solid phase change of a CuPt nanoalloy of 309 atoms with 1:1 stoichiometry and demonstrate the synergic use of two complementary methodologies, iterative temperature molecular dynamics and nested sampling, towards our goal. We choose a 309 atoms nanoparticle because at this size we expect that its thermodynamic and energetic properties will be dictated mostly by the surface to volume ratio contributions and not by electronic effects. Further, this is the smallest size where surface, subsurface, and core shells are, in principle, clearly distinguishable, hence making possible to detect possible surface-melting or inner-core solidification phenomena unequivocally.

5.1.1 Computational set-up and analysis method

In itMD simulations we fix $\Delta T = 25$ K and vary $\Delta\tau = 1, 2.5, 5, 25, 250$ ns with $\lambda = \Delta T / \Delta\tau$ to assess kinetic effects contributions in determining the phase change temperature of the system when undergoing freezing or melting. At least 25 independent runs for each λ are performed to obtain robust statistics on the nanoparticle structures observed after nucleation from the melt. The starting configuration for freezing simulation is a liquid droplet, obtained after 10 ns of a microcanonical run at 1400 K. Final structures from each independent solidification run are then reheated to a liquid phase. Nested sampling calculations follow the framework discussed in Ref [99] and involve an initial set of 1920 configurations generated by randomly positioning the 309 atoms in a periodic cubic box of volume of 91125 \AA^3 . Two runs of 9.6×10^4 steps are performed. The steps by which sampling evolves are 92% single atomic displacements, and 8 % atomic species swaps. Converged Nested Sampling (NS) runs yield information about the thermodynamic limit behaviour of the system properties. NS calculations have been carried on by Dr. Livia Bartok-Partay (Reading University) in collaboration with Prof. Gabor Csany (Cambridge University).

For each λ value in the itMD simulations, we record the nanoparticle instantaneous temperature and excess energy and average them over the ensemble of independent runs. We here recall that the excess energy, Δ , is a measure of the nanoparticle energy contributions normalized as a function of its size and stoichiometry:[3]

$$\Delta = (E_{\text{tot}} - NE_{\text{coh}}) / N^{2/3} , \quad (5.1)$$

where E_{coh} is the cohesive energy of the metal in the bulk, N the number of atoms in the nanoparticle, raised to the power $2/3$ to account for surface to volume contributions.

The error on ensemble and time averaged T and excess energy are rather negligible, except for the case of the phase change region. The phase change temperature reported in the rest of the subsection, T_f for freezing, T_m for melting, was found by fitting splines on the caloric curve, in correspondence of its inflection point. The term caloric curve is here understood as the function defined by expressing the energy as the dependent variable and the temperature as the independent one. The ensemble of nanoparticle structures resulting from the freezing of a liquid droplet are characterized according to the arrangement of atomic environments presenting peculiar local symmetries in their neighbourhood (icosahedral, 5-fold twinned, fcc crystalline), as discussed in subsection 2.4.1. The nanoalloy chemical ordering is analysed using the chemical radial distribution function, detailed in subsection 2.4.3.

5.1.2 Kinetics driven melting/freezing hysteresis

The caloric curves from freezing itMD and NS simulations are shown in Figure 5.1. In the NS framework, the freezing temperature, T_f , is estimated to be 965 ± 10 K. In the case of freezing itMD, depending on the cooling rate, the nucleation temperature shifts from $T_f=888$ K ($\lambda = 25$ K/1 ns) to $T_f=975$ K ($\lambda = 25$ K/250 ns), the latter falling within the NS prediction.

The solid structures sampled by NS and a subset of the ones found below freezing by itMD runs, totalling a minimum of one hundred per rate, are characterised following the gIh mapping discussed in Subsection 2.4.1. Table 5.1 gathers the structural population distributions right after freezing as found by itMD or NS. Both techniques identify that more than 80% of the structures nucleated a twinning, with a low occurrence of Dh. The abundance of Ih over Dh nanoparticles sampled by itMD with respect to NS hints at the presence of kinetic effects leading to the formation of surface hcp islands and short five-fold axes at the phase change. Nonetheless, the relative abundance of the morphological groups is not significantly affected by λ .

When more than one five-fold axis is present within the nanoparticle, they are positioned so that the angles among them are approximately $60 - 65^\circ$, near the reference value in a perfect icosahedron (63.43°). The axes intersection may also lie outside the nanoparticle. A

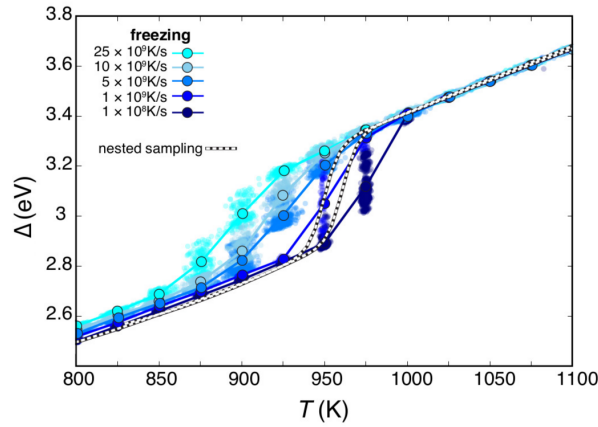


Figure 5.1 Caloric curves for the freezing of a $\text{Cu}_{162}\text{Pt}_{147}$ liquid droplet: scattered points and filled circles refer to the itMD data averaged as discussed in the text, lines are guides to the eye only. Colours refer to λ , where a lighter blue tone corresponds to faster rate. NS results are shown by black and white dashed lines, and they should be considered as quasi-thermodynamic limit for that system. Reproduced under CC BY license from Thermodynamics of CuPt nanoalloys - K. Rossi, L. Bartok-Pártay, G. Csanyi, F. Baletto, Scientific reports 8, 2018.

Table 5.1 Percentages of the three morphological families as found in itMD freezing simulations at different λ and NS, taken just below T_{pc} . The itMD occurrence corresponds to temperatures at 700 K, below which no morphological changes are observed, and they are averaged over all the 25 independent runs. The nested sampling percentages are reported for the two runs exploring all basins.

λ (10^9 K/s)	Ih	Dh	Cp
10	75	7	18
1	73	10	17
5	69	12	19
10	75	14	11
25	72	8	20
NS (850-900K)	58	18	24
NS (850-900K)	54	22	24

large portion of structures with more than two five-fold axes present them in a triangular or tetrahedral arrangement, matching what found in Ref. [112, 113]. However they are never parallel one another, as instead found in Au_{923} [114, 115]. This behaviour can be possibly ascribed to the three times smaller size of the nanoparticle under investigation. If three or more five-fold axes intersect in different points, the so formed triangles have an 8-9 atoms long edge, while tetrahedra edges consist of 5 (as in a perfect Ih of 309 atoms) or 6 atoms. Dh structures generally have their five-fold axis off-centre, possibly also at the very surface of the nanoparticle, with a virtual column of atoms completing the 5-fold symmetry. In the absence of five-fold axis, the nanoparticle shows 8 or 9 close-packed layers, both hcp or fcc, in comparison, a perfect Co of 309 atoms presents 9 fcc layers. During the nucleation of a Cp motif, kinetic contributions may be significant, the ratio of hcp to total layers in fact decreases from 50% to 33% when λ decreases, matching the NS predictions of fcc layers occurrence in the 50%-70% range.

Contrasting itMD structures sampled at same temperatures but for different observation time scales, we can estimate the characteristic time for shape rearrangements in a CuPt_{309} nanoparticles. For cooling rates faster than 10^8 K/ns the landscape explored consists of a single basin also just below the solidification temperature, corresponding to the absence of accessible morphological structural transitions. At $\lambda = 10^8$ K/s, the itMD trajectory instead probes multiple basins for temperatures below melting and up to 780 K. After the latter, the system gets trapped in a single structural basin and no other morphological transition, but surface diffusion, takes place. We thus estimate the characteristic observation time scale for

shape rearrangements to be larger than 25 ns for temperatures in the 750-950 K and at least ten-fold longer below this range.

To investigate the presence of an hysteresis in the caloric curve of the melting and freezing of nanoparticles we reverse the itMD procedure and melt the solidified structures sampled at the end of the freezing runs. As reported in Figure 5.2 the hysteresis width appears to depend on the λ driving the temperature change. Indeed faster heating rates drive the estimate of higher melting temperatures. When λ is reduced, the melting-freezing caloric curve hysteresis gets considerably narrower: at $\lambda = 25 \times 10^9$ K/s the difference between the melting and the freezing temperatures is ~ 160 K, but only of ~ 80 K for $\lambda = 5 \times 10^9$ K/s, and smaller than 15 K for $\lambda = 10^8$ K/s, suggesting a closure at even slower rates, if not at the latter. In fact, already for this rate, we note that for temperatures above 1000 K, $\text{Cu}_{162}\text{Pt}_{147}$ is always liquid while below 950 K is always solid. When estimating the melting temperature from the caloric curve inflection points, the itMD estimate for the phase change of $\text{Cu}_{162}\text{Pt}_{147}$ is 970 K for the slowest temperature change rate, again matching very well the NS prediction.

When analysing the nanoparticle radial distribution function, Figure 5.3 left panel, we note that at temperatures around the critical one, both the nanoparticle surface and core show regions with liquid-like and solid-like ordering. This result hints at the absence of surface

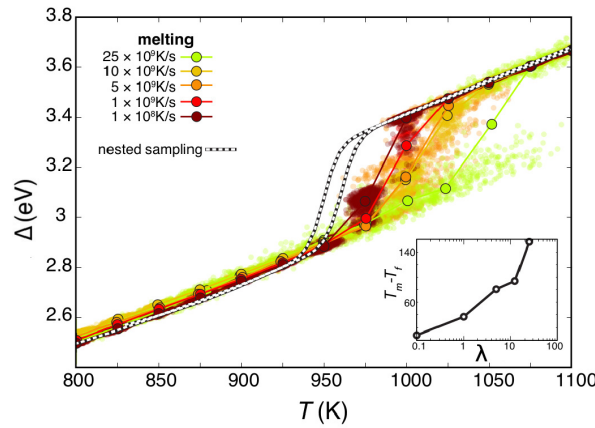


Figure 5.2 Top panel shows the melting caloric curves of the previously solidified $\text{Cu}_{162}\text{Pt}_{147}$ by itMD, scattered points and filled circles as in Fig. 5.1. Colours refer to λ , where a lighter red tone corresponds to faster rate. NS results (black and white dashed lines) are reported as reference point. The inset displays the temperature-width, between the highest temperature at which the nanoparticle is always solid during heating, T_m , and T_f , the lowest temperature at which nanoalloys are liquid during cooling, against λ . Reproduced under CC BY license from Thermodynamics of CuPt nanoalloys - K. Rossi, L. Bartok-Pártay, G. Csanyi, F. Baletto, Scientific reports 8, 2018.

pre-melting or inner core solidification phenomena, opposite to what found in other smaller (55 atoms) or larger (1000-10000 atoms) systems[116, 52]. In these previous investigations it was demonstrated that when the kinetics of the phase changes differ - e.g, melting initiates at the surface, but freezing starts by the nucleation of an inner core solid seed - the hysteresis in the caloric curve is physical and is not affected by the temperature change rate. Our results demonstrate that in $\text{Cu}_{162}\text{Pt}_{147}$ melting and freezing proceed via the same mechanism, and the hysteresis in the caloric curve can be closed for slow enough rates. This result is in good agreement with the picture of size-dependent melting mechanisms in nanoparticles: the formation of one or more quasi-liquid layers before a complete melting was observed only in nanoparticles larger than several nanometers. [47, 117] Similarly, we can argue that the interface energy needed to form a quasi-liquid layer in 1-2.5 nm CuPt nanoparticles is too big.

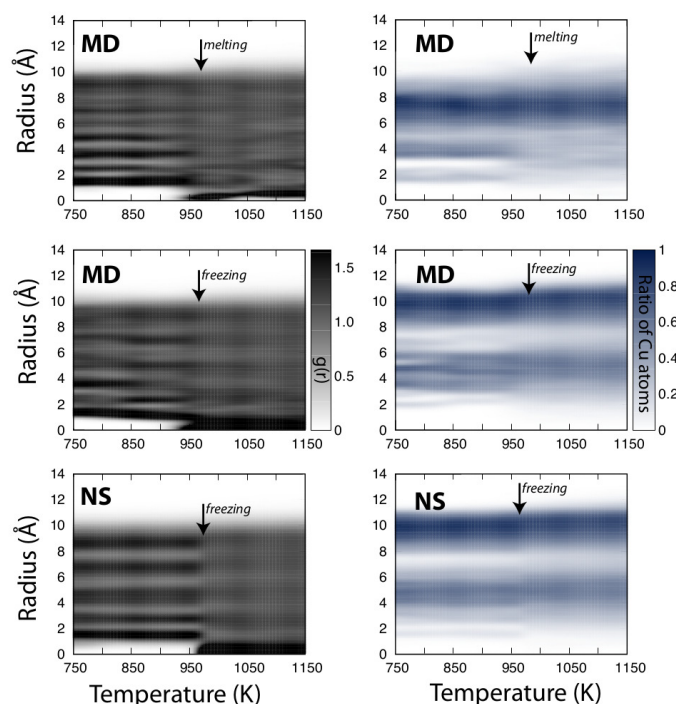


Figure 5.3 Radial distribution of atoms around the centre-of-mass as a function of temperature. The top two panel shows an example itMD run with a $\lambda = 10^9$ K/s for melting and freezing, respectively, while the bottom panel shows the results from NS calculations. The left hand side panels show the overall distribution of atoms, while the right hand side figures show the relative occurrence of Cu atoms within the nanoparticle. The estimated phase change temperatures are marked by arrows for reference. Reproduced under CC BY license from Thermodynamics of CuPt nanoalloys - K. Rossi, L. Bartok-Pártay, G. Csanyi, F. Baletto, Scientific reports 8, 2018.

Hence, melting and solidification happen via the same mechanism and the respective phase change temperatures coincide for slow enough temperature change rates. Indeed, NS data provide an estimate at the quasi-thermodynamic limit of the thermodynamic properties of the system and are matched by itMD ones for simulations with $\lambda < 1$ K/ns. The low temperature dependence of the radial (chemical) distribution function of the nanoalloy is evident from Figure 5.3 left panel. The multi-shell elemental distribution, Cu-rich surface (60%), a Pt-rich subsurface ($\sim 80\%$), and the third and fourth layers again Cu-rich, is preserved also above the melting point.

5.2 On the structure of melted and solid nanoparticles

The aim of this section is to discuss the success in the application of the pair distribution function structural analysis to discriminate melted and solid nanoparticles. While structural differences between melted and solid nanoparticles can be trivially predicted, recasting them in terms of a single robust order parameter has been a longstanding challenge in the literature (see also Subsection 1.5.3).

For a comprehensive investigation of phase changes in transition metal nanoclusters we focus on a wide set of systems: Cu, Ag, Au, Pt nanoparticles of different sizes below 4 nm (146, 147, 192, 201, 309, 344, 389, 405, 434, 489, 561, 486, 686, 891, 923, 976 atoms) and initial shapes (Icosahedra, re-entrant Decahedra, Truncated Octahedra, Octahedra). Results from this work have been gathered in collaboration with Raphael Pinto-Miles during his Master Thesis.

5.2.1 Computational set-up and analysis method

To simulate phase changes in metallic nanoparticles we employ an iterative temperature Molecular Dynamics scheme. It consists of concatenated canonical molecular dynamics runs where the temperature of the system is lowered or increased by a temperature ΔT every $\Delta \tau$ time. Here we report data for $\Delta T = 5$ K and $\Delta \tau = 1$ ns. The initial temperature of the system is set to 400 K for Ag and Au systems, 500 K for Cu, and 900 K for Pt. The final temperature is instead 500 K more for the first three systems and 600 K for the last one. The Velocity-Verlet algorithm is used to evolve Newton's Equation of motion while an Andersen thermostat is used to mimic the interaction of the system with a stochastic bath, with the instantaneous temperature of the system estimated according to the equipartition theorem. Metal-Metal interactions are modelled within the second moment approximation of the tight-binding theory,[73] whose parametrizations were reported in Table 2.1.

To analyse within a coherent framework the energetic trends found for nanoparticles of different size and composition we monitor their excess energy Δ (see Equation 5.1) as a function of temperature. To characterize the nanoparticles structural evolution when subject to heating up to melting and beyond, we instead monitor their Pair Distance Distribution Function.

During the dynamical evolution of the system subject to heating we store instantaneous atomic positions, excess energy, and temperature every 10 ps. For a robust investigation we analyze results averaged from at least eight independent simulations. We parse each data set according to their instantaneous temperature. Here, we report data for temperature bin widths ranging from 5 K to 25 K. The larger the temperature binning is, the less precise but not less accurate the estimate of the melting phase change results. We then average the instantaneous excess energies of all the configurations in the same temperature bin and calculate the standard deviation from the average excess energy. Similarly, for each configuration, we first calculate the corresponding pair distance distribution function, with distance occurrences grouped in bins of 0.1 Å. We then estimate an average PDF for each temperature bin, by summing the instantaneous PDF therein, normalized by the number of configurations found in such temperature bin. When the nanoparticle melting temperature, T_m , is estimated from the caloric curve, and it is defined as the one for which the error on the average excess energy is larger. The error on the T_m estimate is taken as the width of the temperature bin.

5.2.2 PDF analysis to characterize melted and solid structures

The PDF of the 16 platinum nanoparticles presenting different sizes and initial shapes are reported in Figure 5.4, 5.5, 5.6, and Figure 5.7. We systematically observe the absence of a peak at the 2nd nearest neighbours distance in the PDFs of all systems when in a liquid phase. The solid-to-liquid phase change was here determined from the caloric curve. The absence of a peak at the second nearest neighbours distances in the systems' pair distribution function emerges as a universal fingerprint of melted nanoparticles.

Further, the PDF second peak intensity is found to gradually diminish in nanoparticles of increasing nominal temperatures. In Figure 5.8 we report the PDF temperature dependent evolution in a Pt₂₀₁ nanoparticle as a paradigmatic example. This observation establishes a fundamental relationship between structural and thermal properties of a nanoparticle. Conversely, measurements tailored to probe changes in the broadness of peaks in the pair distribution function of a nanoparticle one can also inform about the corresponding temperature variations causing them.

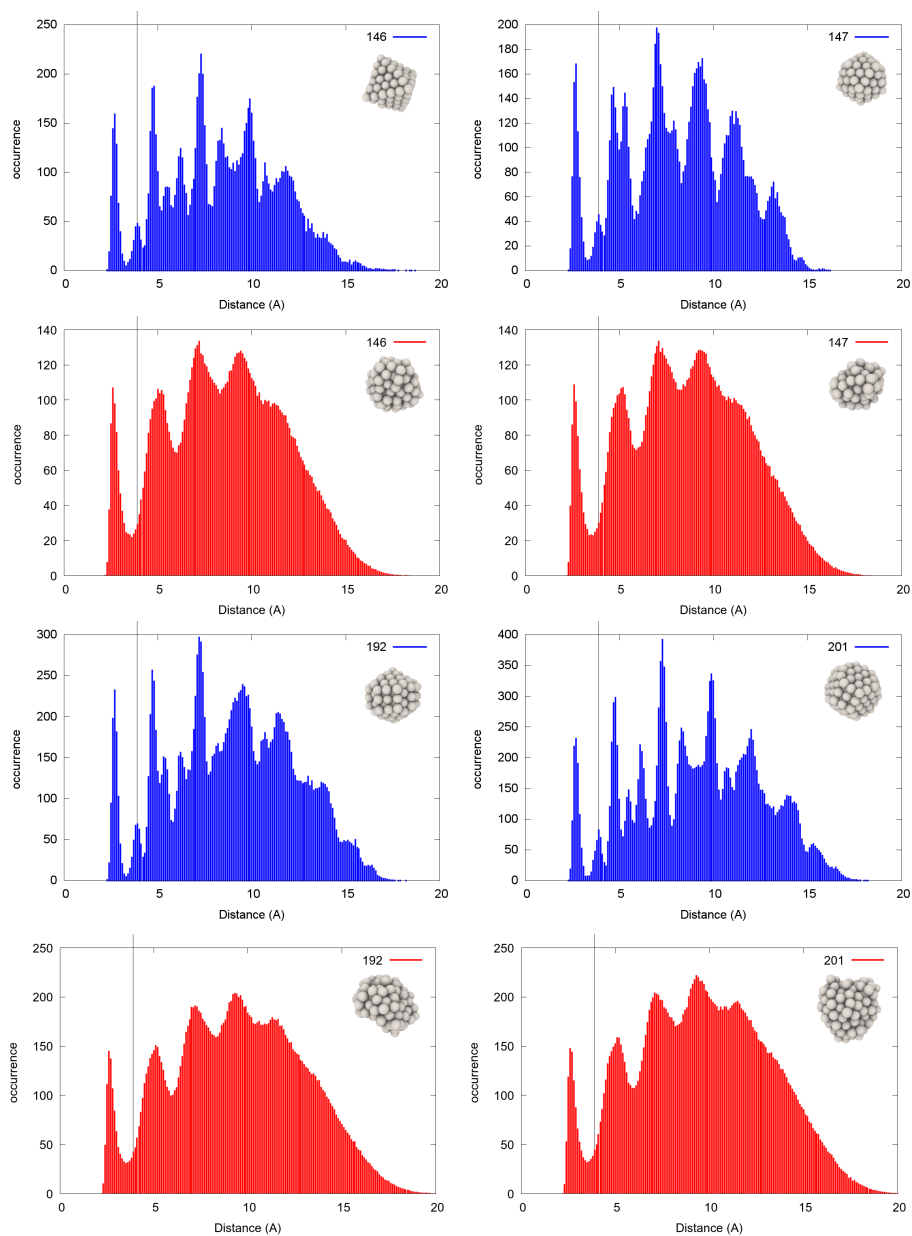


Figure 5.4 Average pair distance distribution function of Pt nanoparticles of different shapes and sizes (146 - 147 - 192 - 201) at 900 K and 1500 K. The top right corner of each subfigure shows the solid structure and an example snapshot of structures observed at 1500 K in the same system.

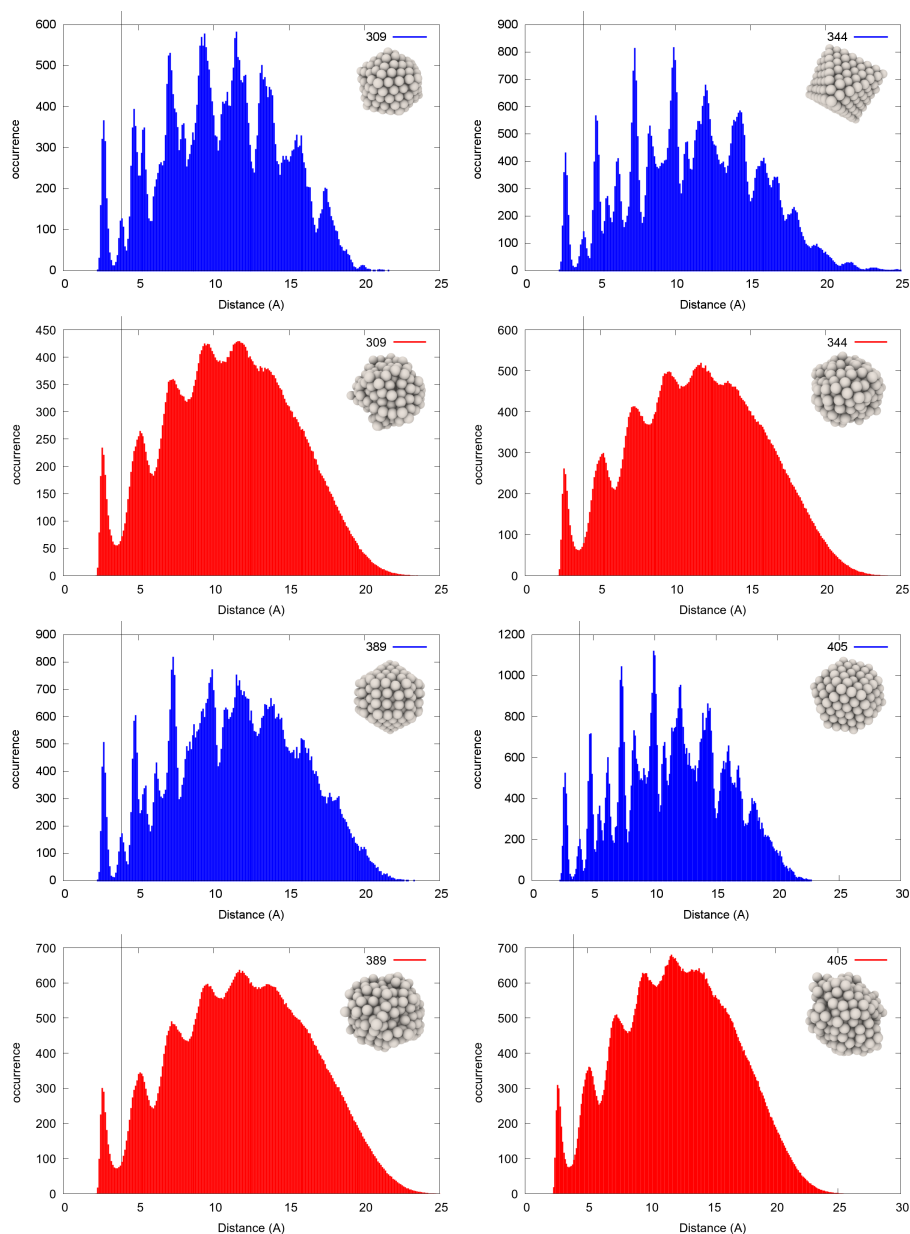


Figure 5.5 Average pair distance distribution function of Pt nanoparticles of different shapes and sizes (309 - 344 - 389 - 405) at 900 K and 1500 K. The top right corner of each subfigure shows the solid structure and an example snapshot of structures observed at 1500 K in the same system.

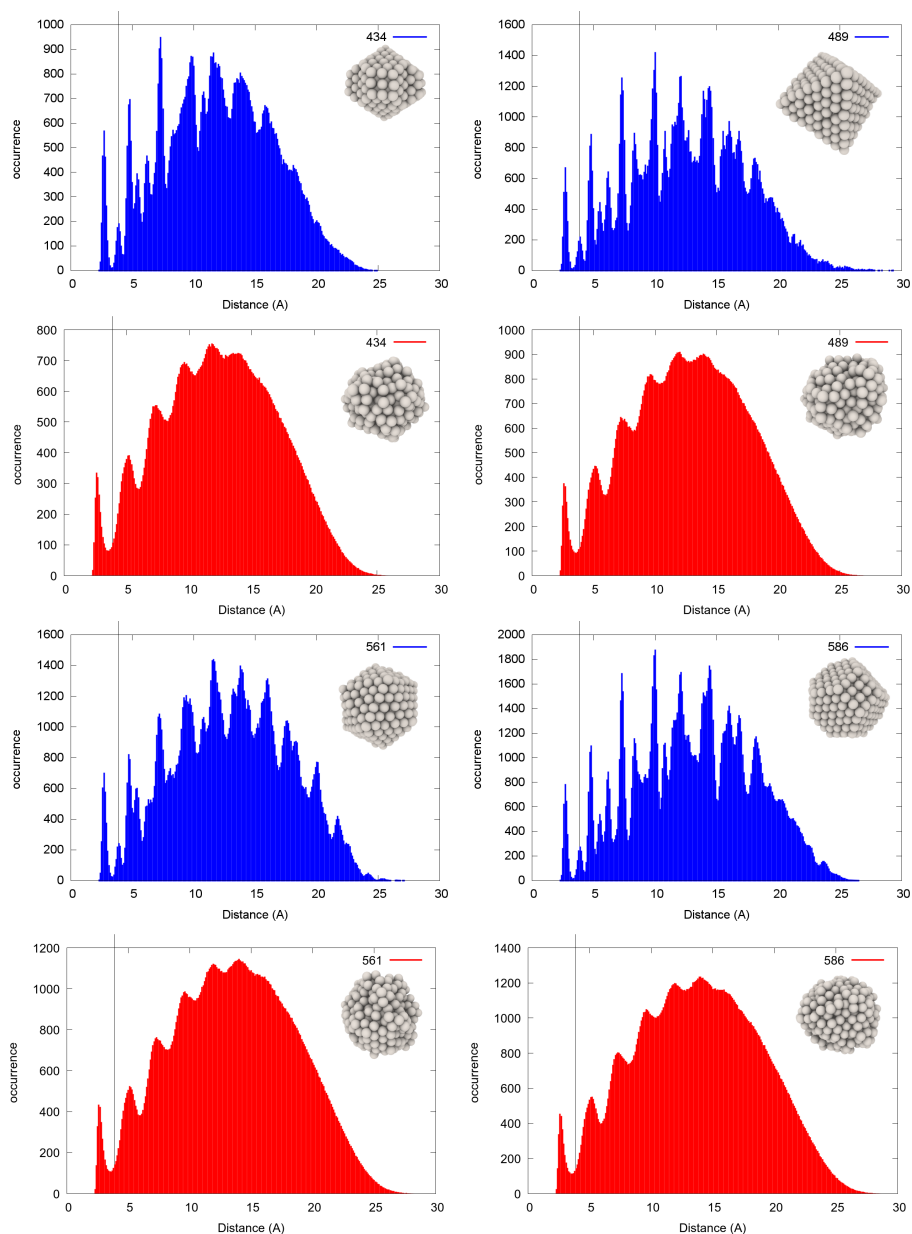


Figure 5.6 Average pair distance distribution function of Pt nanoparticles of different shapes and sizes (434 - 489 - 561 - 586) at 900 K and 1500 K. The top right corner of each subfigure shows the solid structure and an example snapshot of structures observed at 1500 K in the same system.

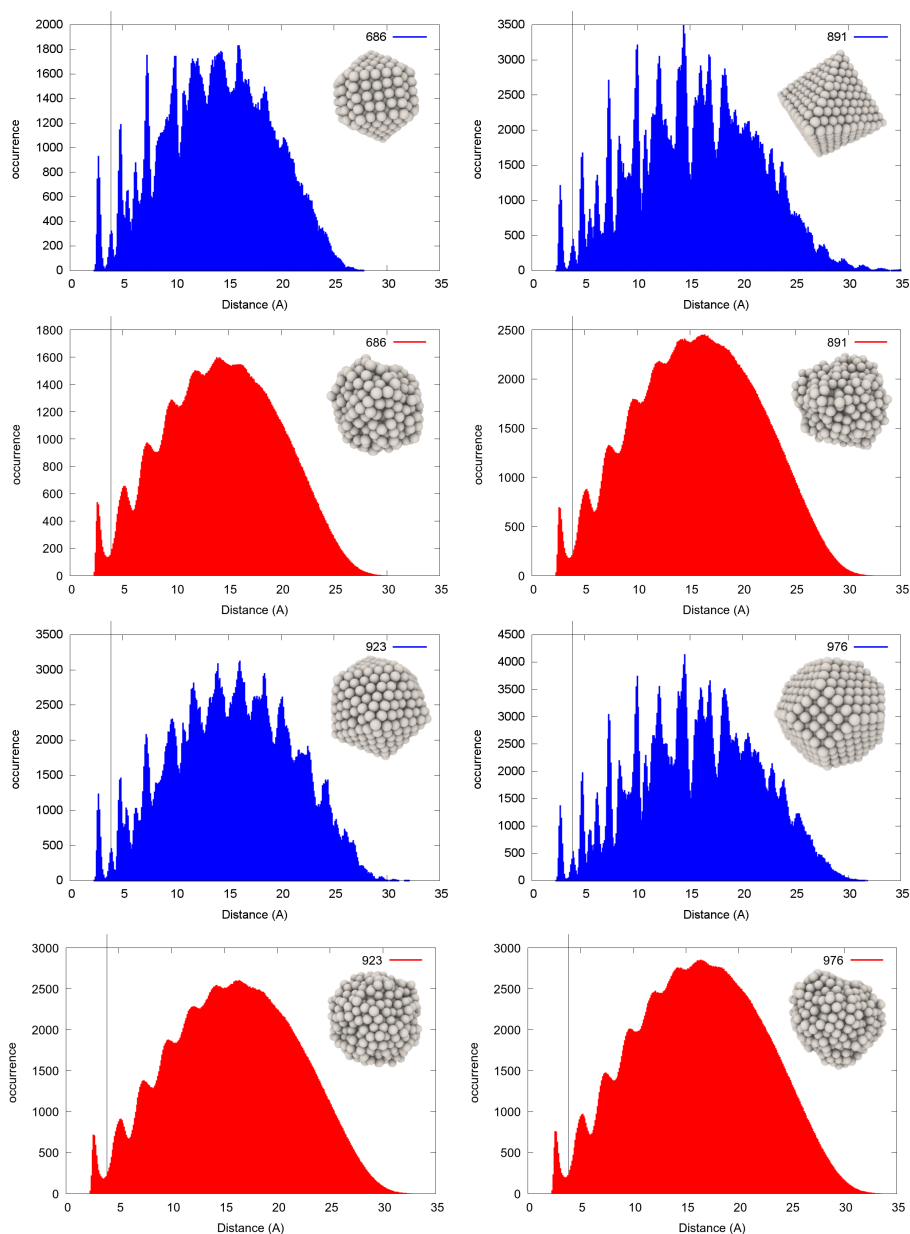


Figure 5.7 Average pair distance distribution function of Pt nanoparticles of different shapes and sizes (686 - 891 - 923 - 976) at 900 K and 1500 K. The top right corner of each subfigure shows the solid structure and an example snapshot of structures observed at 1500 K in the same system.

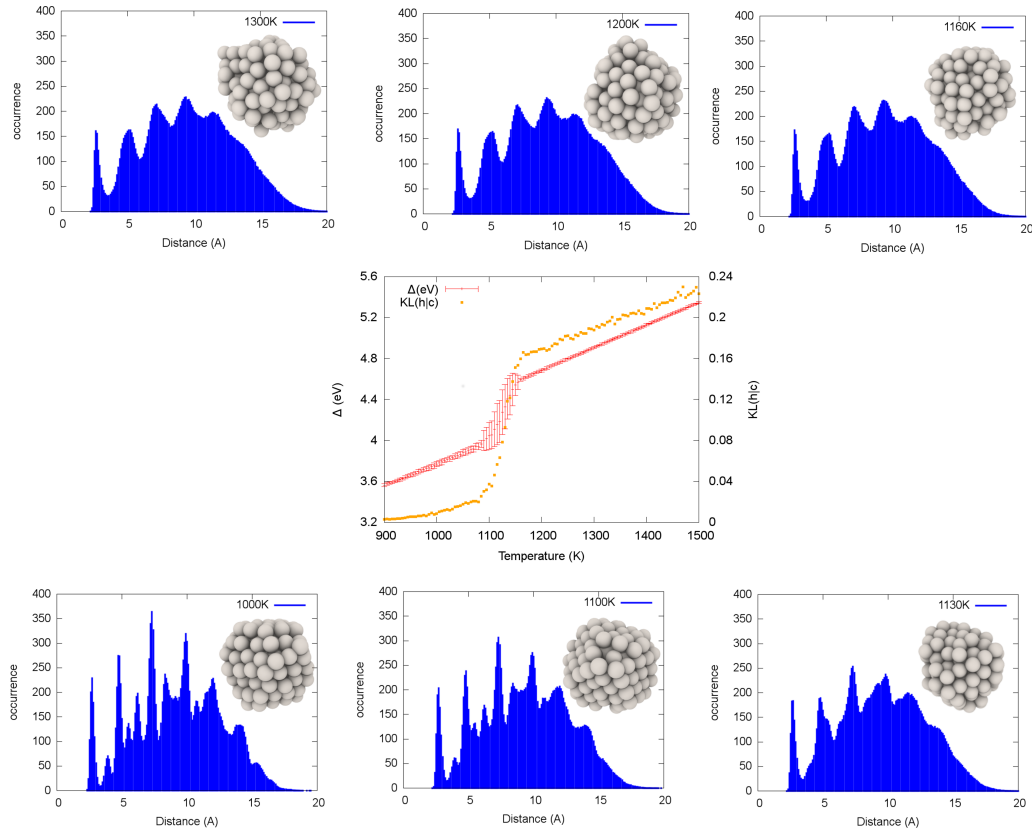


Figure 5.8 Temperature dependent average pair distance distribution function of a Pt_{201} nanoparticle. The second neighbour peak of the PDF is absent for temperatures above 1160 K while a shoulder persists at 1130 K.

To ease the PDF characterization at different temperatures we monitor the Kullback-Leibler divergence ($\text{KL}(h|c)$) between the PDF, up to the second neighbours distance, of a structure at a given temperature (now on denominated as "cold", c) and of ones at higher (now on mentioned as "hot", h). Because of the temperature-driven profile changes in the PDF, the one of an "hot" structure displays an information rich profile, difficult to be captured by the one of a "cold" structure displaying localized nearest neighbour shells (and *viceversa*, but to a lesser extent). In Figure 5.8 we thus report the temperature dependent $\text{KL}(h|c)$ evolution in a Pt_{201} nanoparticle undergoing a phase change. A quasi-discontinuity in the Δ and in the $\text{KL}(h|c)$ is evident at the phase change temperature, $T_{\text{melt}} = 1120 \text{ K} \pm 5 \text{ K}$. The correlation between the caloric and the $\text{KL}(h|c)$ temperature dependent curves is not limited to the phase coexistence region, but also to the solid and liquid phases. This is observed in all the systems under consideration, as demonstrated in Figure 5.9 and 5.10. For a detailed discussion on the robustness of the $\text{KL}(h|c)$ PDF analysis towards the identification of solid and liquid structures the interested reader is referred to Appendix Section B.

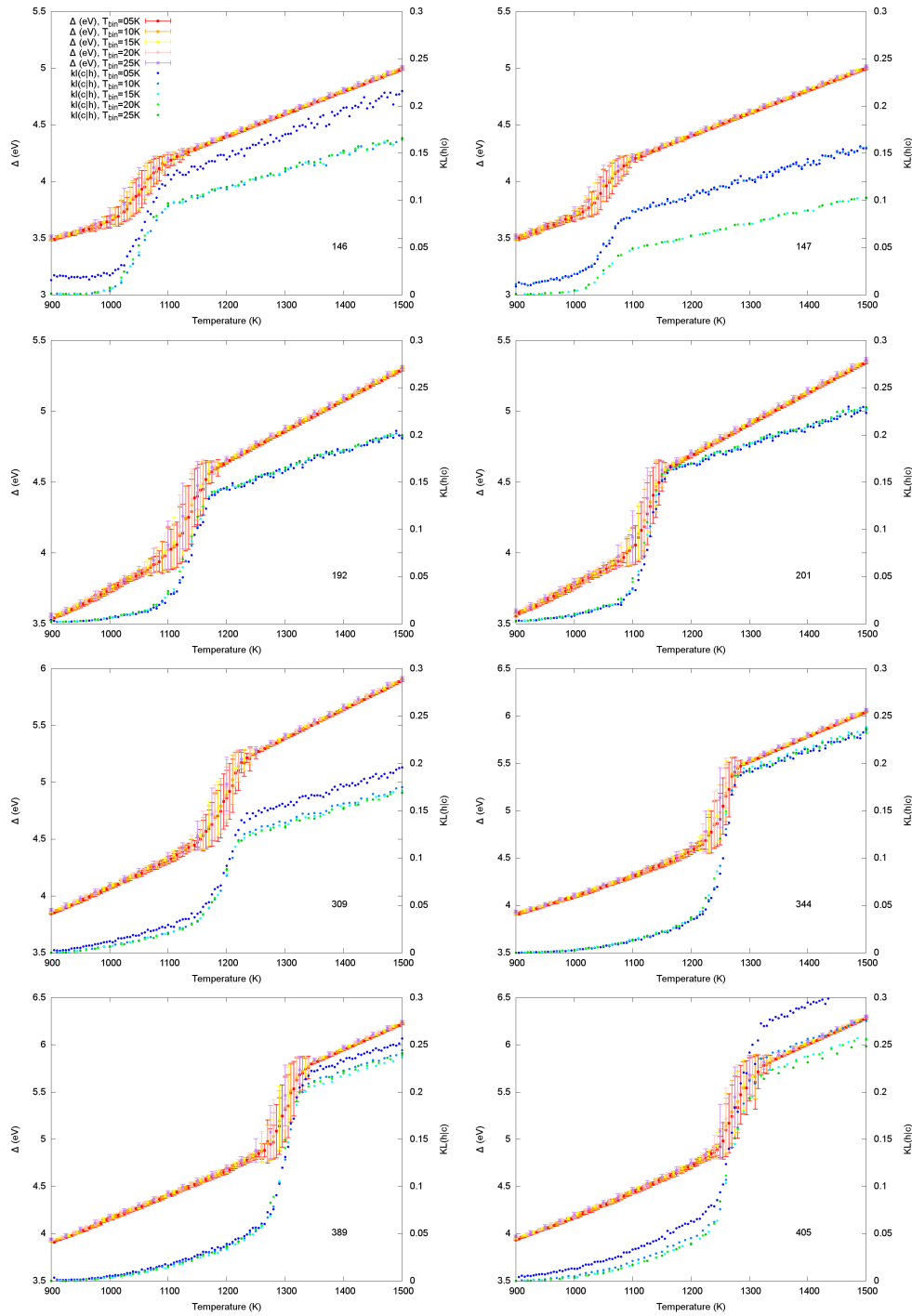


Figure 5.9 Excess energy and KL(h|c) temperature dependence in Pt nanoparticles of different sizes (see label on bottom right corner). A quasi first order transition, simultaneous in both order parameters, signals nanoparticle melting. Results for different temperature bins averaging are in quantitative agreement.

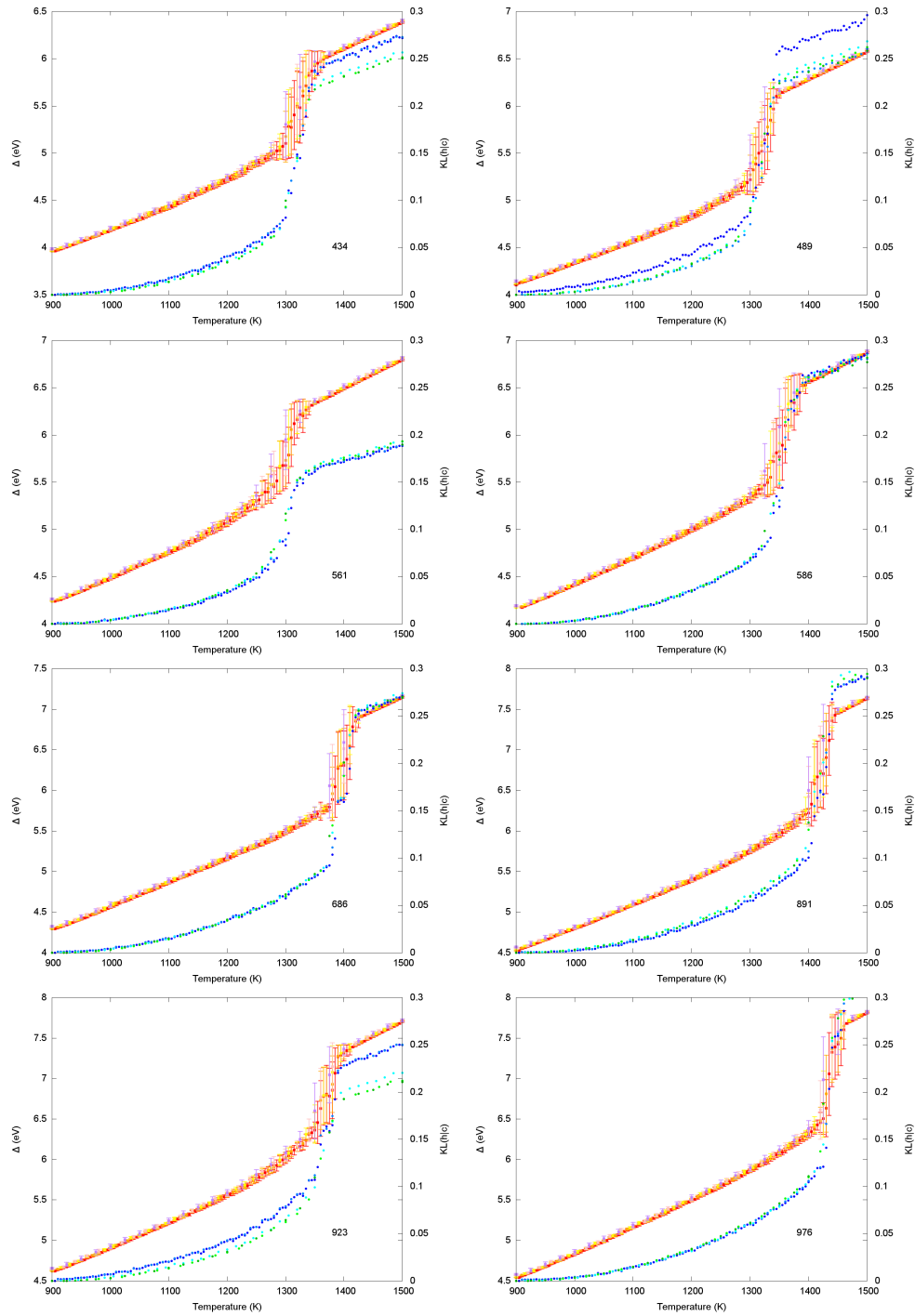


Figure 5.10 Excess energy and KL(h|c) temperature dependence in Pt nanoparticles of different sizes (see label on bottom right corner). A quasi first order transition, simultaneous in both order parameters, signals nanoparticle melting. Results for different temperature bins averaging are in quantitative agreement.

5.2.3 Size-dependent melting phase change temperatures

The data gathered offer a platform to infer relationships between the number of atoms in the system, and the melting point of Cu, Ag, Au, Pt nanoparticles. An inverse relation between size and temperature, regardless of system composition, is inferred from Figure 5.11 where the T_{melt} of each system is reported against their size. We thus fit against the numerical data the following two parameters Gibbs-Thomson like equation by the least square method: $T_{melt} = b + a/N^3$. A quite accurate fitting is observed, especially for Au, Ag, and Pt. Interestingly, the infinite number of atoms limit melting temperature (i.e. the b parameter) resulting from this model does not correspond to the bulk one. As recapped in Table 5.2, melting temperatures smaller by at least 200 K are in fact predicted. The potentials employed in this study are fit to thermodynamical properties of bulk materials. Hence they provide quite accurate estimates of the bulk melting point.[74] Their possible low accuracy thus should not be invoked to rationalize the observed trends.

Table 5.2 Infinite size limit temperature predicted for nanoparticles of Pt, Cu, Ag, Au, and their corresponding bulk melting temperature.

	Pt	Cu	Ag	Au
b	1843	1055	1028	962
T_m^{bulk} [118]	2041	1357	1234	1337

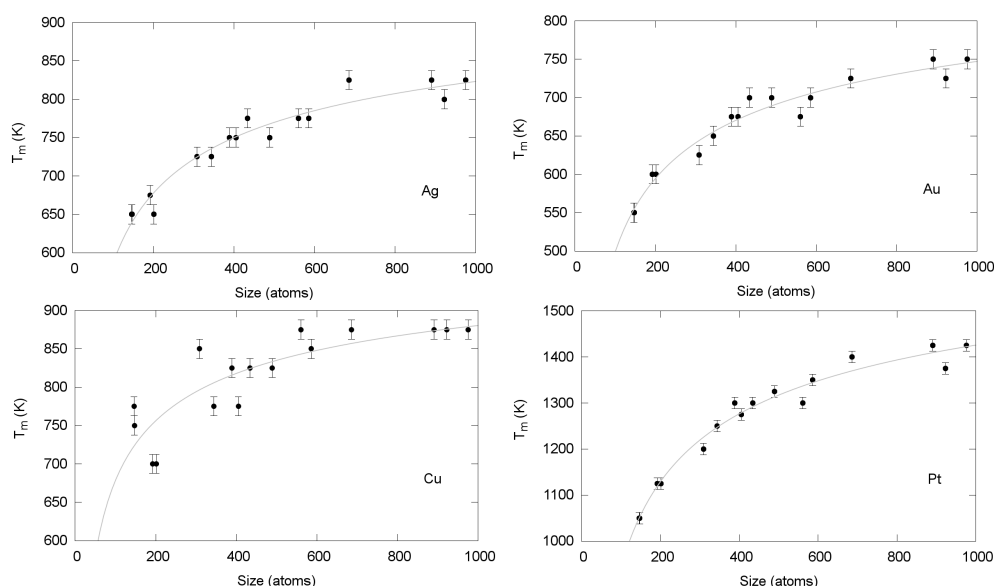


Figure 5.11 Size-dependent melting temperatures of Ag (top-left), Au (top-right), Pt (bottom-left), and Cu (bottom-right) nanoparticles. Fitted curves follow the equation $T_{melt} = b + a/N^3$.

5.2.4 Environment effects on nanoparticle melting

As a preliminary and yet significant case study, let us finally demonstrate the application of the PDF KL analysis for characterizing the solid-liquid transition of a Pt_{201} nanoparticle in a strongly interacting environment modelled according to Equation 2.13 ($\rho=2$, $\varepsilon=0.04\text{eV}$). Figure 5.12 shows the KL(h|c) and excess energy versus temperature curves of 4 independent melting simulations for an initial To structure. Melting at $\sim 950\text{ K}$ is clear from the KL PDF analysis, corroborating the strength and applicability of the here described characterization method. The caloric curves do not present a clear first order transition at this temperature.

It is interesting to note that the observed melting temperature is much lower with respect to the gas phase case. Indeed a strongly interacting environment favours low-symmetry structures which results energetically comparable with closed-shell high symmetry morphology.[55] Conversely, it is likely that entropic and energetic contributions allow for the melting of the nanoparticle at lower temperatures. By the same token, the caloric curve may not present a clear quasi-first order transition at the melting phase change temperature for the same reason. Preliminary calculations validate this conjecture and future works are aimed towards assessing its validity also in other systems, for different ρ and ε parametrizations.

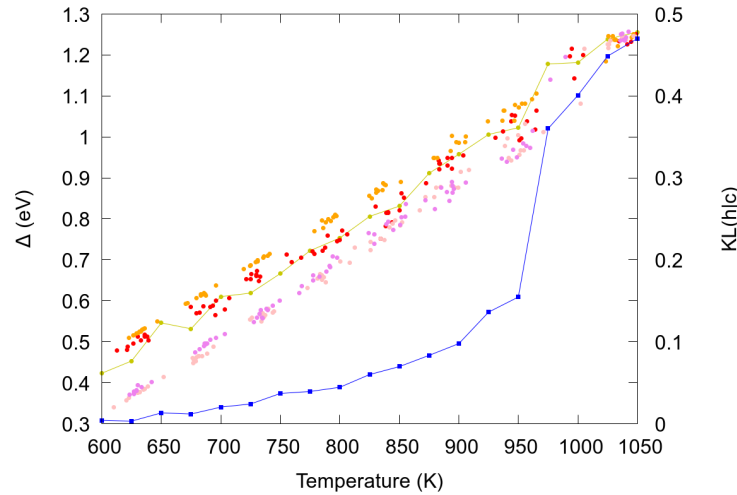


Figure 5.12 Excess energy and KL(h|c) temperature dependence in a Pt nanoparticle of 201 atoms immersed in an implicit strongly interacting environment modelled according to Equation 2.13 ($\rho=2$, $\varepsilon=0.04\text{eV}$). A quasi first order transition in the KL(h|c) signals the nanoparticle melting, yet this is less evident from the caloric curves. Pink, red, purple, and violet data points report the excess energy per temperature observed in each independent run, dark yellow points show their average according to what discussed in subsection 5.2.1. The KL(h|c) data are reported in blue.

5.3 Summary

Through the systematic investigation of solid-liquid and liquid-solid phase changes in $\text{Cu}_{162}\text{Pt}_{147}$ by means of two synergic sampling techniques, itMD and NS, we show that the putative hysteresis between melting and the freezing caloric curves gradually narrows for increasingly slower heating/cooling rates ($T_m - T_f \sim 0$ for $\lambda < 10^8$ K/s in the case of $\text{Cu}_{162}\text{Pt}_{147}$). The phase change temperature, $T_{pc} = 970 \text{ K} \pm 25 \text{ K}$, was estimated from the inflection point of the caloric curves. This result provides an indirect demonstration that employing itMD to model nanoparticles phase changes can reproduce results in agreement with the quasi-thermodynamic behaviour, estimated to be $965 \pm 10 \text{ K}$ by NS calculations for $\text{Cu}_{162}\text{Pt}_{147}$. The closure of the hysteresis is rationalized in terms of the phase change mechanism through which the nanoparticle solidifies or liquefies, with no evidence of surface pre-melting or inner core initial nucleation observed.

Following the systematic investigation of the melting phase change of 64 metallic nanoparticles (Cu, Ag, Au, Pt), of different sizes (146 to 976 atoms), exhibiting four initial configuration (Ih, To, MDh, Oh), we identify the disappearance of a peak at the second nearest neighbours in their pair distance distribution function as a universal signature of melting. We support this claim comparing the melting temperature obtained from the caloric curve, and the change in the pair-distribution function. This allows to state that the relative cross-entropy of the PDF of “cold” and “hot” configurations is an order parameter helpful towards the estimate of the melting transitions in monometallic nanoparticles. Having established a clear dependence of the PDF peak broadness on the system temperature further paves the way towards the experimental measurements of phase changes (solid/liquid and liquid/solid) temperature alternative to calorimetric tools.

Chapter 6

On the ideal shape and size of Pt nanoparticles for oxygen reduction

We here demonstrate how to tackle the rational design of nanoparticles, in relation to the ensemble of non equivalent adsorption sites they present, through the methodological framework presented in sections 2.6 and 2.7. In particular, we discuss the application of the nanogenomics based CHE model towards the rational design of Pt nanoparticles for oxygen Reduction Reaction (ORR). The optimization of the Pt load in catalysing electrochemical oxygen reduction in fuel cells may be ground-breaking in the economically-viable large-scale deployment of these polluting-free power sources. This work has been conducted in collaboration with Dr. Gian Giacomo Asara (King's College London).

6.1 Nanogenomics CHE model for ORR

The nanogenomics CHE model can be readily employed to predict the specific activity of Pt nanoparticles of different sizes and shapes towards ORR. Indeed, it has been demonstrated that the reaction free energy of OH^* , ΔG_0^{OH} (i.e. the rate limiting step for oxygen reduction reaction at the cathode in fuel cells), on any site of a monometallic Pt system can be written as a function of the GCN of the site itself[66, 67]:

$$\begin{cases} \Delta G_0^{\text{OH}} = -0.715 + 0.192 \text{ GCN} & \text{if } \text{GCN} \leq 8.33, \\ \Delta G = 2.345 - 0.178 \text{ GCN} & \text{if } \text{GCN} > 8.33, \end{cases} \quad (6.1)$$

For the case of ORR, the coefficient $\mathcal{C}_\alpha(GD)$ in Equation 2.42 matches the active site limiting specific current, experimentally measured as 96 mA/cm^{-2} and 83 mA/cm^{-2} for (111) and (100) surfaces respectively.[91] Because NEAS in a nanoparticle may not have an infinite

surface counterpart, we fit through these values a linear relationship between the GCN and the corresponding limiting specific current, resulting in $\mathcal{C}_\alpha(GD) = 12.56 \text{ GCN mAcm}^{-2}$.

6.2 Static ideal nanoparticles

To test the effectiveness of sequencing the nanoparticle geometrical genome to predict Pt nanoparticles catalytic activity towards oxygen reduction we consider a structurally varied ensemble of morphologies commonly observed in experiments - Cubes (Cb), Octahedra (Oh), Truncated Octahedra (To), Cuboctahedra (Co), Icosahedra (Ih), InoDecahedra (IDh, $m=n$, $p=1$), Marks Decahedra (MDh, $m=n$, $p=2$) - at four different sizes 1.5 nm, 3.5 nm, 5.5 nm, 7.5 nm. Figure 6.1 collects the GCN-genome sequence of each individual nanoarchitecture, and corresponding specific current versus voltage (I-V) curve.

Following the GCN genome sequencing, one can predict that the catalytic properties of (111)- and (211)-like NEAS in a Pt nanoparticle with, e.g., a cuboctahedral morphology and a nuclearity of at least 309 atoms, will resemble their extended surface counterparts for the adsorption of atomic O. This prediction is in good agreement with electronic structure calculations recently reported by Nørskov and coworkers.[119]

The size dependent trends in the GCN genome further allow to rationalize the drop in the ORR mass activity of Pt nanoparticles of size below 1.5 nm: active sites characterised by high GCN, between 7.33-8.5, are indeed not present or scarce in small nanoparticles. By the same token, the specific activity is known to approach the one of extended low-Miller index surfaces in nanoparticles of increasing size: indeed the occurrence of NEAS with GCN equal to the one of Low-Miller index sites grows quadratically, while the other NEAS occurrence increases linearly (edge and quasi-edge sites), or stays constant with size.

To move forward counting-sites arguments, let us compare the catalytic activity of the considered nanoparticles towards ORR. As a measure of their activity we here compare the size-and-shape dependent minimum theoretical overpotential, η_1 , needed to produce a density current, j_{NP} , of 1 mAcm^{-2} , where the Pt(111) value of 0.38 V serves as a reference. The theoretical overpotential corresponds to 1.23 V minus the applied potential, 1.23 V being the maximum applied potential to make the ORR happen. Each morphology shows no difference in η_1 , when its diameter - defined as the maximum atomic pair distance - enlarges from 5.5 to 7.5 nm, with an average value of $0.41 \pm 0.02 \text{ V}$, excluding the two extreme and opposite cases of Cu and MDh which have a large size limit of 0.56 V and 0.37 V, respectively. For Cu, MDh and To, we register small changes of about 0.05 V in η_1 when the nanoparticle's diameter is enlarged from 1.5 to 5.5 nm. On the other hand, in the same size range, Oh and Ih

decrease their η_1 of 0.10-0.15V, while for Co and IDh the drop is even larger, 0.20 V. These changes match exactly the ones observed in recent experimental investigations.[120]

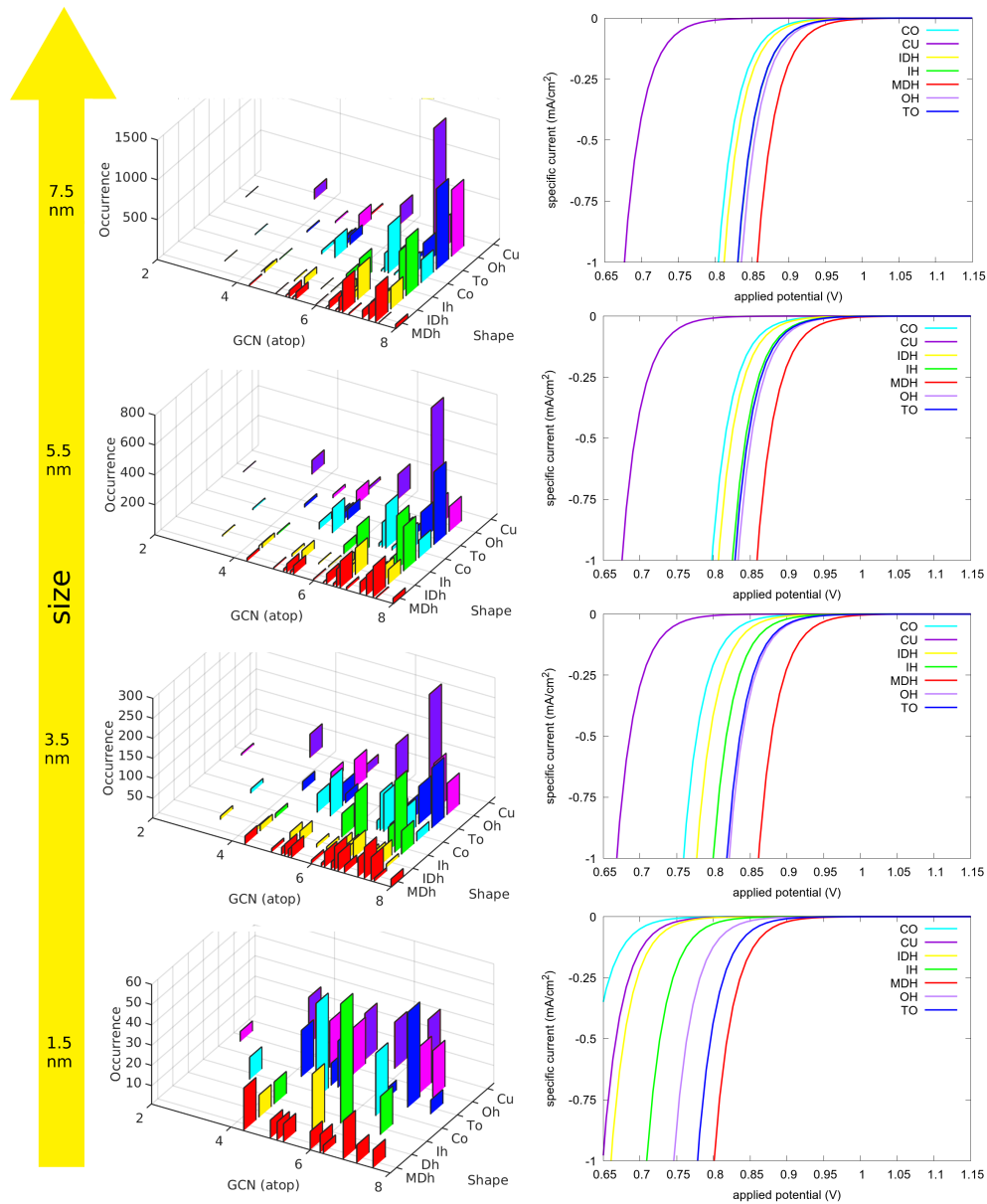


Figure 6.1 Left panel: GCN-genomes for seven Pt-geometries (listed in the y-axis labels), at 1.5, 3.5, 5.5 and 7.5 nm diameter. A complete GCN fingerprint appears above 3.5 nm, while the occurrence of (111) and (100) sites become predominant only above 5.5 nm. Right panel: Corresponding theoretical I-V curves calculated at room temperature.

Our single nanoparticle analysis forecasts the Marks decahedron as the most promising shape among the closed-shell geometries here considered, and over the whole size range here studied. Indeed, just by looking at the large size limit, its specific activity calculated at 0.9 V, the applied potential at which fuel cell performance are generally compared in the literature, is much larger than the one of the other closed-shell structures. Further, MDh η_1 positively compare against the pure and infinite Pt(111) one. As concave active sites are identified as ideal to efficiently catalyse ORR, we investigate the cuts of a pentagonal bi-pyramid which present the maximal mass activity, defined as the specific activity of the nanoparticle times its active area and normalized by its mass. We here discuss the available truncations of a Dh in terms of three integers m, n and p identifying respectively the number of atoms along the five-fold axis, along the (100) edge perpendicular to it, and along the twin planes. By systematically exploring the m, n, p parameters space, we observe that the largest mass activity is observed for the 1-x-3 family, with the 1-2-3 structure displaying the maximum one, as shown in Figure 6.2. Further, the η_1 of structures in the 1-x-3 family is, on average, close to 0.33 V, hence 0.05 V lower with respect to the η_1 of infinite Pt(111) surfaces.

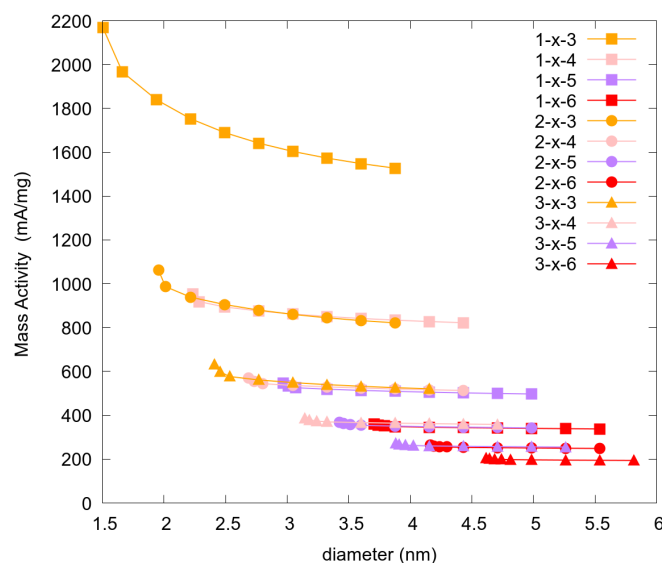


Figure 6.2 Size-dependent mass activity in several re-entrant decahedra, presenting m in the 1-3 range, p between 2 to 6 atoms, and n in the 2-11 range. Sets of pentagonal bypyramids cuts are colour coded according to their p and labelled by different symbols according to their m . Conversely 10 points, corresponding to the 2-11 n values, are reported per each set. The diameter label corresponds to the longest axis in the nanoparticle, calculated according to Equation 1.4.

Through this systematic analysis we thus demonstrated how the newly formalized nanogenomics CHE model can drive the computational *in silico* design of optimal nanoparticle structures for ORR and, in turn, promote their experimental synthesis. Let us here mention that 5-fold twinned re-entrant nanostructures have been already demonstrated to be extremely active [121], however their high activity was attributed to the high surface area and not understood also in terms of the presence of optimally coordinated active sites.

Parallel to the identification of ideal nanoparticles' architectures, the here discussed Nanogenomics CHE model can also help in shedding light on the controversies in the literature regarding the putative size-dependent peak in the mass activity of Pt nanoparticles. Although several experiments reported the maximum mass activity at sizes around 2 nm,[62] the consensus on this measurement is not universal. Towards offering a possible solution to this puzzle we analyze the size-dependent mass activity of the seven archetypical architectures so far considered, Figure 6.3 The nanoparticles' sizes at which a peak in the mass activity is witnessed vary depending on their morphology. The optimal size for cubic Pt nanoparticles is roughly 3.5 nm, yet the mass activity corresponding to such architecture is more than ten-fold lower with respect to the one of the other structures. For the case of the Icosahedron, a peak is observed at 6 nm. The Co and IDh structures find their mass activity peak in architectures with a diameter of ~ 7 nm. For the case of the To and the Oh, the peak is instead at 3.5 nm and 5 nm respectively. In all of the non re-entrant structures, terminated with (111) facets, a sharp increase in the mass activity is always witnessed for architectures larger than 2.5 nm. When looking at the MDh, this increase is even more steep and takes place just above diameters of 2 nm. The mass activity then peaks shortly after, for sizes of ~ 3 nm.

The heterogeneous set of behaviours here observed offers a clear end towards the rationalization of the controversies about the size-dependent mass activity peak for Pt nanoparticles towards ORR. Indeed the synthesis of diverse structural samples can lead to the identification of size-dependent mass activity peaks which are however inconsistent one with respect to another. As discussed in the previous chapters, morphological polydispersity is commonly observed *in vitro*, hence further challenging the comparison of the activity in nanoparticles which are size-selected but not fully characterized from the structural point of view.

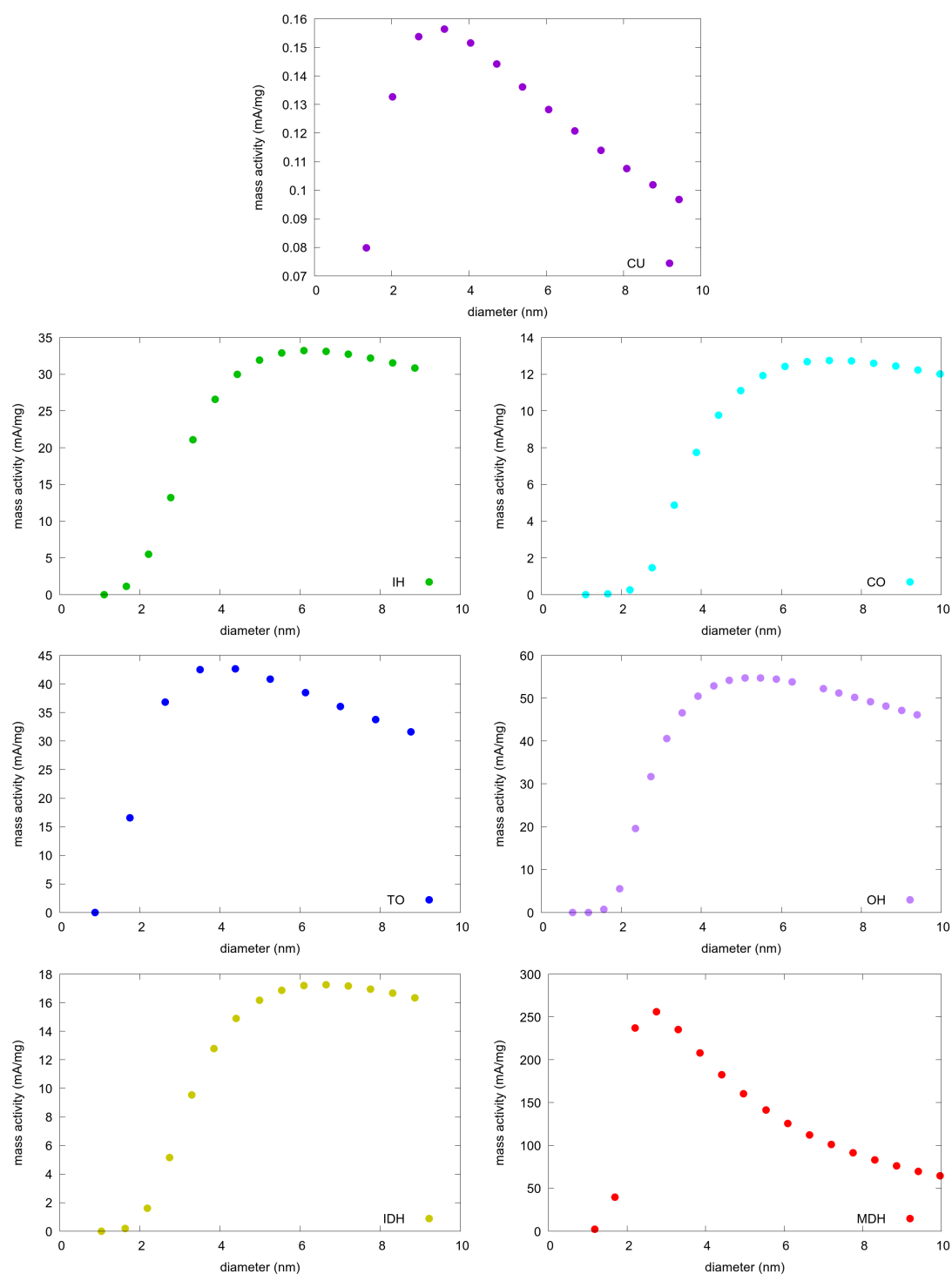


Figure 6.3 Size dependent mass activity of seven different Pt nanoparticles morphologies (labelled in the bottom right corner of each subfigure).

6.3 Structurally rearranging nanoparticles

The numerous reports on catalyst reconstruction and degradation when in operando highlight the need to move beyond the static catalytic lattice assumption and synergistically combine counting-site methods to simulations probing NEAS temporal and spatial evolution.

6.3.1 Oxide supported nanoparticles subject to heating

As a preliminary case study, towards the application in the case of in operando structural rearrangements, we analyse the evolution of the catalytic properties of a perfect icosahedron of 561 atoms (~ 2.5 nm) soft-landed onto a pristine-MgO substrate. The system temperature is increased from 300 K to 1500 K, to sample thermally activated structural rearrangements at different temperatures. An in depth discussion of the solid-solid rearrangements sampled was presented in Chapter 3, Section 3.2.2. The morphological transitions are here taken as proxy of what might happen for the case of catalyst reconstructions when in-operando. Conversely, the I-V curves are calculated at room temperature. Figure 6.4 shows the evolution of the nanoparticle GCN genome and of its catalytic activity, measured in terms of η_1 .

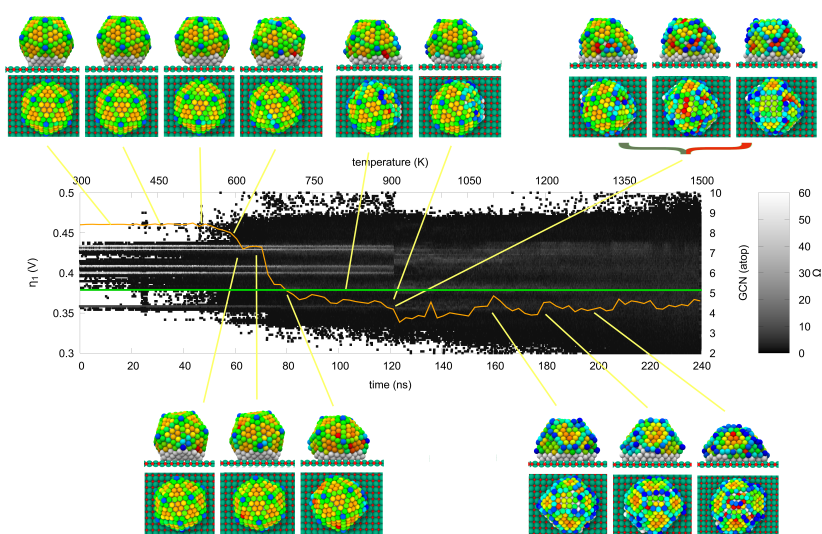


Figure 6.4 Example genome (greyscale) and η_1 (orange) evolution for an Ih_{561} soft-landed upon a pristine MgO undergoing thermally driven structural rearrangement. Reference η_1 value for Pt(111) extended surface is reported in green. Snapshot to depict the structural evolution of the nanoparticle are also reported. Mg atoms are in green, O atoms are in red, Pt nanoparticle atoms are in grey if not counted in the genome, or colour coded according to their generalized coordination (aqua (hot) tones for low (high) coordinated atoms).

The reconstruction of the icosahedron into a more energetically favourable defected crystalline motif corresponds to an increase in the catalytic activity of the Pt nanoparticle towards ORR. The initial structural changes induced by the support, resulting in fewer atomic pairs belonging to twinning planes, drive a consistent drop of η_1 to 0.42 V. The minimum of η_1 at 0.34 V observed for the structures sampled afterwards that drop instead parallels the formation of a fcc motif where the two first layers at the oxide substrate are less numerous than the third one. During the final stages of the simulation, in the 1100-1300 K temperature range, we observe the formation of several surface defects which significantly affect the nanoparticle genome, and the subsequent oscillation of η_1 around 0.35 V. We remark that this η_1 value is still positively comparable against the one of a Pt(111) infinite surface.

6.3.2 Implementing structural disorder via fast annealing

Thermally driven structural disordering of the surface of a nanoparticle promotes the formation of concave sites which are active towards ORR. We thus simulate the fast thermal annealing of a liquid droplet to demonstrate how this synthesis method enables to engineer highly active site for ORR in a nanoparticle. As a paradigmatic example, let us discuss the predicted catalytic activity of Pt₅₆₁ nanoparticles resulting from the fast freezing ($\Delta T/\Delta\tau=50$ K / 1 ns) of a liquid droplet.

In Figure 6.5 we report the changes in the nanoparticle GCN genome with temperature and in the nanoparticle η_1 . The latter, for the melted structures (in cyan), is already lower than the reference one of a closed-shell Ih morphology (in blue) as well as than the one of a Pt(111) infinite surface (in green). Anyway, after freezing - evident in Figure 6.5 from the sharp change in the GCN genomes of the nanoparticles after the phase change - η_1 further diminishes of ~ 0.04 V. Interestingly, this is observed in all the independent simulations, notwithstanding the structural differences between the observed architectures. Indeed, regardless of whether they are 5-fold twinned (top structures in the right panel of Figure 6.5) or crystalline (bottom structure in the right panel of Figure 6.5), η_1 gets close to an average value of 0.33 V.

Preliminary results show that a similar behaviour is observed in larger systems where $\eta_1^{close-shell} < \eta_1^{melted} < \eta_1^{solid-defected}$. This is however not necessarily the case for nanoparticles of size smaller than 561 atoms.

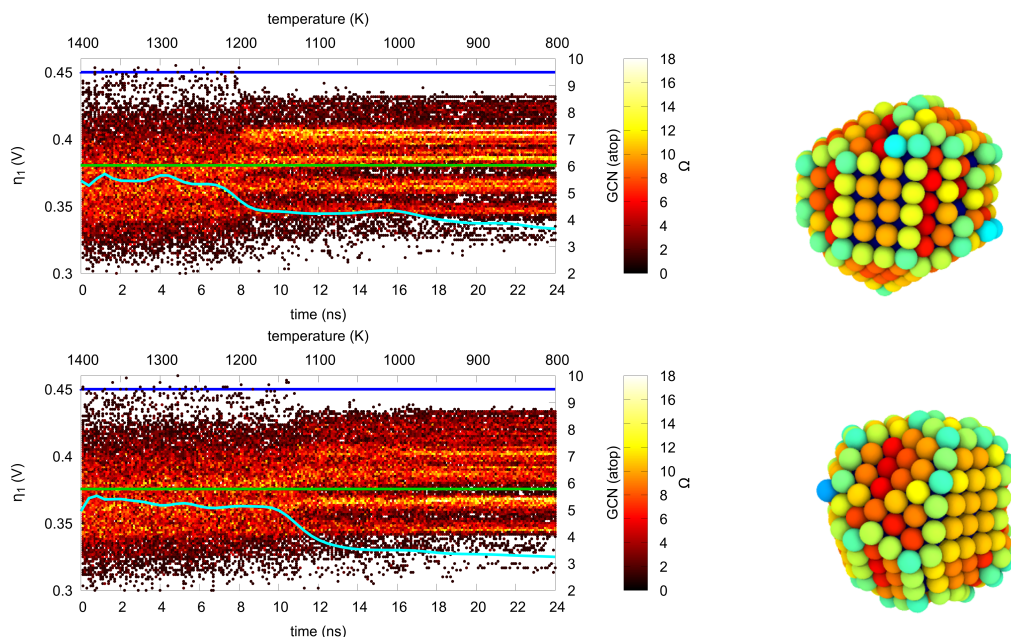


Figure 6.5 Left panel: Example genomes and η_1 evolutions for a Pt_{561} nanoparticle undergoing a liquid-to-solid transition. Notwithstanding the two different structures observed, a similar η_1 is predicted. Right panel: Pt nanoparticles resulting from the freezing of a liquid droplets, atoms are colour coded according to their generalized coordination (aqua tones for low coordinated atoms, hot tones for highly coordinated ones).

6.4 Summary

Beyond the challenges of a first-principles description of extrinsic effects on the nanoparticles and adsorbates interactions, we demonstrate that characterising the nature and distribution of adsorption sites in a nanoparticle using a geometrical descriptor is a pragmatic and robust way to estimate the activity of a nanocatalyst. Indeed practical guidelines for the rational design of Pt nanoparticle for ORR can be extracted by sequencing a geometrical genome based on the GCN of adsorption sites. Through this approach we in fact identified two possible routes for the formation of nanoparticles with attractive catalytic properties: (i) the controlled synthesis of concave decahedral shapes presenting specific structural features; (ii) a fast annealing of size selected nanodroplets to implement structural disorder but also the formation of concave active sites on their surface.

We believe that this elegant and effective approach provides new directions to deliver practical guidelines for the rational design of more active and selective nanocatalysts. Further it allows to address the impact of thermal activated processes on the structure and, in turn, on the catalytic properties of a nanoparticle.

Chapter 7

Conclusion

The aim of this thesis was to promote advances in the understanding of how size, shape, and composition determine the interplay between kinetic, thermodynamic, and energetic contributions to the stability of nanoparticles of 100-1000 atoms against melting and pre-melting transitions. This was achieved through the application of state-of-the-art sampling techniques and systematic investigations.

In Chapter III the (meta)stability of 5-fold twinned or crystalline nanoparticles against transitions towards an Icosahedral morphology was thoroughly assessed by means of Metadynamics and iterative temperature Molecular Dynamics. Concerted rearrangements connecting the morphological basins of interest were witnessed only for the case of nuclearities smaller than a composition-dependent critical size. The latter can be rationalized from the stiffness of the potential ruling interatomic interaction. Surface diffusion driven mechanisms are instead detected for the case of nanoparticle morphological rearrangements within the same structural basin.

In Chapter IV we discuss the extension of this work for the case of nanoalloys. Fully concerted mechanisms are observed to connect Ih to Co and Dh morphologies in energetically favourable small mismatch core-shell and in Janus nanoalloys. For mismatch larger than the 10% (e.g. Cu@Ag) only core-concerted transitions are detected. In unfavourable ordering core-shell nanoalloys (e.g. Ag@Au instead of Au@Ag) a combination surface diffusion driven and locally concerted rearrangement is instead found to connect the three morphological basins of interest.

Our results thus detail paradigms in the synthesis of (meta)stable structure with bespoke barriers in their energetic landscape. The ability to predict, if not control, the metastability of a nanoparticle at finite temperature and in realistic conditions is in turn paramount towards their application in groundbreaking technological devices, such as, e.g. economically viable fuel cells.

In Chapter V we demonstrated how liquid and solid nanoparticle can be univocally identified from the absence or presence of a peak at distances corresponding to second nearest neighbours in the pair distribution function. Although, intuitively, liquid and solid structures are known to vary greatly, no order parameter was previously identified to discriminate these two phases regardless of their size and composition. The systematic assessment of melting phase change in systems of different composition, size, and initial shape further provided a playground to test analytical models to predict nanoparticles melting temperature as a function of their size. Intriguingly, the bulk melting temperature is not recovered in the infinite size limit when fitting a Gibbs-Thompson like equation of the form $T_m = b + a/N^3$.

Beyond the accurate identification of melting and liquid structures, kinetic effects are known to affect the estimate of the phase change temperature of a nanoparticle. Via the synergic combination of iterative temperature Molecular Dynamics simulations and Nested Sampling calculations we rationalize the presence of an hysteresis between the melting and freezing curve of $\text{Cu}_{162}\text{Pt}_{147}$ in terms of kinetic effects. Indeed by tuning the temperature change rate the hysteresis between the two curve changes, with the two essentially coinciding for the case of a temperature change rate of 0.1 K/ns or lower.

To provide guidance in the fast and accurate prediction of catalytic properties of nanoparticles we adapted the computational hydrogen model of Norskov and coworkers to exploit explicitly the geometric structure - catalytic property relationship inherent to Pt nanoparticles catalysing oxygen reduction reaction. In Chapter VI, we first perform the highthroughput analysis of close-shell ideal morphologies catalytic properties to identify concave cuts of 5-fold twinned decahedra as highly active structures. Then, we demonstrate how the implementation of structural disorder via temperature driven kinetic rearrangements might be also beneficial towards enhancing the catalytic properties of Pt nanoparticles. This possibly counter-intuitive result paves the way towards practical and facile engineering of nanoparticles structure, so that they present ideally active site.

As a by-product of the main investigations discussed in this thesis the blossoming of a diverse set of research strands has been witnessed. The development of interaction potentials and force-field encoding realistic complexity for an accessible computational cost has been performed. The systematic analysis of how strongly interacting environment and support can affect the metastability of a nanoparticle is thus now accessible (Subsection 2.2.3). By the same token, the newly established framework of nanoparticles genomes for catalysis facilitates rational design tasks and presents natural extensions towards the study of systems beyond the gas phase case, e.g. on a support or coated by ligands (Subsections 2.6 and 2.7).

Bibliography

- [1] Richard P Feynman. There's plenty of room at the bottom. California Institute of Technology, Alumni Association].
- [2] George Wulff. XXV. Zur Frage der Geschwindigkeit des Wachstums und der Auflösung der Krystallflächen. *Zeitschrift für Kristallographie - Crystalline Materials*, 34(1-6), 1901.
- [3] Francesca Baletto, Riccardo Ferrando, Alessandro Fortunelli, Francesco Montalenti, and Christine Mottet. Crossover among structural motifs in transition and noble-metal clusters. *Journal of Chemical Physics*, 116(9):3856–3863, 2002.
- [4] Lawrence D Marks. Experimental studies of small particle structures. *Reports on Progress in Physics*, 57(6):603–649, 1994.
- [5] Riccardo Ferrando, Julius Jellinek, and Roy L. Johnston. Nanoalloys: From Theory to Applications of Alloy Clusters and Nanoparticles. *Chemical Reviews*, 108(3):845–910, 2008.
- [6] Riccardo Ferrando. Symmetry breaking and morphological instabilities in core-shell metallic nanoparticles. *Journal of Physics: Condensed Matter*, 27(1):013003, 2015.
- [7] Tianyou Chen and Valentin O. Rodionov. Controllable Catalysis with Nanoparticles: Bimetallic Alloy Systems and Surface Adsorbates. *ACS Catalysis*, 6(6):4025–4033, 2016.
- [8] Chun-Jiang Jia and Ferdi Schüth. Colloidal metal nanoparticles as a component of designed catalyst. *Physical Chemistry Chemical Physics*, 13:2457–2487, 2011.
- [9] Gian Giacomo Asara, Lauro Oliver Paz-borbon, and Francesca Baletto. “Get in Touch and Keep in Contact”: interface effect on the ORR activity for supported PtNi nanoparticles. *ACS Catalysis*, 6(7):4388–4393, 2016.
- [10] Sophie Carenco. Describing inorganic nanoparticles in the context of surface reactivity and catalysis. *Chemical Communications*, 54(50):6719–6727, 2018.
- [11] Matteo Salvalaglio. Chapter 3 - on the mechanistic studies of the growth of anisotropic particles (theory and simulation). In Ning Wu, Daeyeon Lee, and Alberto Striolo, editors, *Anisotropic Particle Assemblies*, pages 55 – 103. Elsevier, Amsterdam, 2018.
- [12] Kristen A. Fichthorn. Atomic-Scale Theory and Simulations for Colloidal Metal Nanocrystal Growth. *Journal of Chemical & Engineering Data*, 59(10):3113–3119, oct 2014.

- [13] Santosh Kumar Meena and Marialore Sulpizi. From Gold Nanoseeds to Nanorods: The Microscopic Origin of the Anisotropic Growth. *Angewandte Chemie*, 128(39):12139–12143, sep 2016.
- [14] Yves Huttel. *Gas-phase synthesis of nanoparticles*. Wiley, 2017.
- [15] Guillermo González-Rubio, Andrés Guerrero-Martínez, and Luis M. Liz-Marzán. Reshaping, Fragmentation, and Assembly of Gold Nanoparticles Assisted by Pulse Lasers. *Accounts of Chemical Research*, 49(4):678–686, apr 2016.
- [16] Richard E. Palmer, Lu Cao, and Fan Yin. Note: Proof of principle of a new type of cluster beam source with potential for scale-up. *Review of Scientific Instruments*, 87(4):046103, 2016.
- [17] Peter R. Ellis, Christopher M. Brown, Peter T. Bishop, Jinlong Yin, Kevin Cooke, William D. Terry, Jian Liu, Feng Yin, and Richard E. Palmer. The cluster beam route to model catalysts and beyond. *Faraday Discuss.*, 188(0):39–56, 2016.
- [18] Isabelle Braud, Sebastian Zamith, and Jean-Marc L’Hermite. A gas aggregation source for the production of heterogeneous molecular clusters. *Review of Scientific Instruments*, 88(4):043102, 2017.
- [19] Francesca Baletto, Christine Mottet, and Riccard Ferrando. Freezing of silver nanodroplets. *Chemical Physics Letters*, 354(1-2):82–87, 2002.
- [20] Francesca Baletto, Christine Mottet, and Riccardo Ferrando. Growth of three-shell onionlike bimetallic nanoparticles. *Physical review letters*, 90(13):135504, 2003.
- [21] Francesca Baletto, Arnaldo Rapallo, Giulia Rossi, and Riccardo Ferrando. Dynamical effects in the formation of magic cluster structures. *Physical Review B*, 69(23):235421, 2004.
- [22] Yitao Wang, Ziyou Y. Li, Sung J. Park, Ahmed Abdela, David Tang, and Richard E. Palmer. Quantitative Z-contrast imaging in the scanning transmission electron microscope with size-selected clusters. *Physical Review B*, 84(7):073408, 2011.
- [23] Bridget Ingham. X-ray scattering characterisation of nanoparticles. *Crystallography Reviews*, 21(4):229–303, 2015.
- [24] Janis Timoshenko, Deyu Lu, Yuewei Lin, and Anatoly I. Frenkel. Supervised Machine-Learning-Based Determination of Three-Dimensional Structure of Metallic Nanoparticles. *The Journal of Physical Chemistry Letters*, 8(20):5091–5098, 2017.
- [25] Francesca Baletto and Riccardo Ferrando. Structural properties of nanoclusters: Energetic, thermodynamic, and kinetic effects. *Reviews of Modern Physics*, 77(1):371–423, 2005.
- [26] Lawrence D. Marks and Lintao Peng. Nanoparticle shape, thermodynamics and kinetics. *Journal of Physics Condensed Matter*, 28(5), 2016.
- [27] David J. Wales. *Energy landscapes*. Cambridge University Press, 2003.

- [28] David J. Wales. Exploring Energy Landscapes. *Annual Review of Physical Chemistry*, 69(1):401–425, apr 2018.
- [29] V. Rosato, M. Guillope, and B. Legrand. Thermodynamical and structural properties of f.c.c. transition metals using a simple tight-binding model. *Philosophical Magazine A*, 59(2):321–336, 1989.
- [30] Jhonathan P. Doye and Florent Calvo. Entropic effects on the size dependence of cluster structure. *Physical review letters*, 86(16):3570–3, 2001.
- [31] Martin J. Rahm and Paul Erhart. Beyond magic numbers: Atomic scale equilibrium nanoparticle shapes for any size. *Nano Letters*, 17(9):5775–5781, 2017.
- [32] Anna L. Garden, Abild Pedersen, and Hannes Jónsson. Reassignment of ‘magic numbers’ for au clusters of decahedral and fcc structural motifs. *Nanoscale*, 10(11):5124–5132, 2018.
- [33] Simon R. Plant, Lu Cao, and Richard E. Palmer. Atomic Structure Control of Size-Selected Gold Nanoclusters during Formation. *Journal of the American Chemical Society*, 136(21):7559–7562, 2014.
- [34] Zheng W. Wang and Richard E. Palmer. Experimental Evidence for Fluctuating, Chiral-Type Au 55 Clusters by Direct Atomic Imaging. *Nano Letters*, 12(11):5510–5514, 2012.
- [35] Kenji Koga, Tamio Ikeshoji, and Ko-ichi Sugawara. Size- and temperature-dependent structural transitions in gold nanoparticles. *Physical Review Letters*, 92(11):115507, 2004.
- [36] Dawn M. Foster, Riccardo Ferrando, and Richard E. Palmer. Experimental determination of the energy difference between competing isomers of deposited, size-selected gold nanoclusters. *Nature Communications*, 9(1):1323, 2018.
- [37] Tomoaki Niiyama, Shinichi Sawada, Kensuke S. Ikeda, and Yasushi Shimizu. A numerical study upon the atomistic mechanisms of rapid diffusion in nanoclusters. *Chemical Physics Letters*, 503(4-6):252–255, 2011.
- [38] Florent Calvo, Alessandro Fortunelli, Fabio Negreiros, and David J. Wales. Communication: Kinetics of chemical ordering in Ag-Au and Ag-Ni nanoalloys. *The Journal of chemical physics*, 139(11):111102, 2013.
- [39] William N. Lipscomb. Framework rearrangement in boranes and carboranes. *Science (New York, N.Y.)*, 153(3734):373–8, 1966.
- [40] Julia Uppenbrink and David J. Wales. Packing schemes for Lennard-Jones clusters of 13 to 150 atoms: minima, transition states and rearrangement mechanisms. *Faraday Transactions*, 87(2):215, 1991.
- [41] Bingqing Cheng and Alfonso H W Ngan. Thermally induced solid-solid structural transition of copper nanoparticles through direct geometrical conversion. *The Journal of chemical physics*, 138(16):164314, 2013.

- [42] Terrell L. Hill. Thermodynamics of Small Systems. *The Journal of Chemical Physics*, 36(12):3182, 1962.
- [43] Constantino Tsallis. Possible generalization of Boltzmann-Gibbs statistics. *Journal of Statistical Physics*, 52(1-2):479–487, 1988.
- [44] P. N. Pawlow. On the dependency of the melting point on the surface energy of a solid body. *Zeitschrift fur physikalische Chemie*, 65(1-35):545–548, 1909.
- [45] Paul R. Couchman and Walter A. Jesser. Thermodynamic theory of size dependence of melting temperature in metals. *Nature*, 269(5628):481–483, oct 1977.
- [46] David J. Wales and R. Stephen Berry. Coexistence in Finite Systems. *Physical Review Letters*, 73(21):2875–2878, 1994.
- [47] S. J. Zhao, S. Q. Wang, D. Y. Cheng, and H. Q. Ye. Three distinctive melting mechanisms in isolated nanoparticles. *The Journal of Physical Chemistry B*, 105(51):12857–12860, 2001.
- [48] Zhen Hua Li and Donald G. Truhlar. Nanosolids, slushes, and nanoliquids: Characterization of nanophases in metal clusters and nanoparticles. *Journal of American Chemistry Society*, 130:1269812711, 2008.
- [49] Zhen Hua Li and Donald G. Truhlar. Nanothermodynamics of metal nanoparticles. *Chemical Science*, 5(7):2605, 2014.
- [50] Weihong Qi. Nanoscopic thermodynamics. *Accounts of Chemical Research*, 49:1587–1595, 2016.
- [51] Florent Calvo. Thermodynamics of nanoalloys. *Physical chemistry chemical physics*, 17(42):27922–39, 2015.
- [52] Mark Hou. Solid–liquid and liquid–solid transitions in metal nanoparticles. *Physical Chemistry Chemical Physics*, 19(8):5994–6005, 2017.
- [53] Luca Pavan, Francesca Baletto, and Rada Novakovic. Multiscale approach for studying melting transitions in CuPt nanoparticles. *Physical Chemistry Chemical Physics*, 17(42):28364–28371, 2015.
- [54] Kevin Rossi, Livia Bartok-Pártay, Gabor Csányi, and Francesca Baletto. Thermodynamics of cupt nanoalloys. *Scientific Reports*, 8(1), 2018.
- [55] Robinson Cortes-Huerto, Jacek Goniakowski, and Claudine Noguera. An efficient many-body potential for the interaction of transition and noble metal nano-objects with an environment. *The Journal of chemical physics*, 138(24):244706, 2013.
- [56] J. Dana. Honeycutt and Hans C. Andersen. Molecular dynamics study of melting and freezing of small Lennard-Jones clusters. *Journal of Physical Chemistry*, 91(19):4950–4963, 1987.
- [57] Paul Steinhardt, David Nelson, and Marco Ronchetti. Bond-orientational order in liquids and glasses. *Physical Review B*, 28(2):784–805, 1983.

- [58] Jeffrey Greeley. Active Site of an Industrial Catalyst. *Science*, 336(6083):810–811, 2014.
- [59] A. Stephen K. Hashmi and Graham J. Hutchings. Gold Catalysis. *Angewandte Chemie International Edition*, 45(47):7896–7936, 2006.
- [60] Ambarish Kulkarni, Samira Siahrostami, Anjali Patel, and Jens K. Nørskov. Understanding catalytic activity trends in the oxygen reduction reaction. *Chemical Reviews*, 118:2302–2312, 2018.
- [61] Andrew J. Medford, Aleksandra Vojvodic, Jens S. Hummelshøj, Johannes Voss, Frank Abild-Pedersen, Felix Studt, Thomas Bligaard, Anders Nilsson, and Jens K. Nørskov. From the sabatier principle to a predictive theory of transition-metal heterogeneous catalysis. *Journal of Catalysis*, 328:36 – 42, 2015.
- [62] Minhua Shao, Amra Peles, and Krista Shoemaker. Electrocatalysis on Platinum Nanoparticles: Particle Size Effect on Oxygen Reduction Reaction Activity. *Nano Letters*, 11(9):3714–3719, 2011.
- [63] Anna Loiudice, Peter Lobaccaro, Esmail A. Kamali, Timothy Thao, Brandon H. Huang, Joel W. Ager, and Raffaella Buonsanti. Tailoring Copper Nanocrystals towards C2 Products in Electrochemical CO2 Reduction. *Angewandte Chemie International Edition*, 55(19):5789–5792, 2016.
- [64] Federico Calle-Vallejo, José I. Martínez, Juan M. García-Lastra, Philippe Sautet, and David Loffreda. Fast Prediction of Adsorption Properties for Platinum Nanocatalysts with Generalized Coordination Numbers. *Angewandte Chemie International Edition*, 53(32):8316–8319, 2014.
- [65] Federico Calle-Vallejo, David Loffreda, Marc T. M. Koper, and Philippe Sautet. Introducing structural sensitivity into adsorption–energy scaling relations by means of coordination numbers. *Nature Chemistry*, 7(5):403–410, 2015.
- [66] Federico Calle-Vallejo, Jakub Tymoczko, Viktor Colic, Quang Huy Vu, Marcus D Pohl, Karina Morgenstern, David Loffreda, Philippe Sautet, Wolfgang Schuhmann, and Aliaksandr S. Bandarenka. Finding optimal surface sites on heterogeneous catalysts by counting nearest neighbors. *Science*, 350(6257):185–189, 2015.
- [67] Federico Calle-Vallejo, Marcus D. Pohl, David Reinisch, David Loffreda, Philippe Sautet, and Aliaksandr S. Bandarenka. Why conclusions from platinum model surfaces do not necessarily lead to enhanced nanoparticle catalysts for the oxygen reduction reaction. *Chemical Science*, 8(3):2283–2289, 2017.
- [68] Lauro Paz-Borbón, Francesca Baletto, Lauro Oliver Paz-Borbón, and Francesca Baletto. A DFT Study on the O2 Adsorption Properties of Supported PtNi Clusters. *Inorganics*, 5(3):43, 2017.
- [69] Zhonglong Zhao, Zhengzheng Chen, Xu Zhang, and Gang Lu. Generalized Surface Coordination Number as an Activity Descriptor for CO2 Reduction on Cu Surfaces. *The Journal of Physical Chemistry C*, 120(49):28125–28130, 2016.

- [70] David J. Wales and Peter Salamon. Observation time scale, free-energy landscapes, and molecular symmetry. *Proceedings of the National Academy of Sciences*, 111(2):617, 2014.
- [71] Loup Verlet. Computer "Experiments" on Classical Fluids. I. Thermodynamical Properties of Lennard-Jones Molecules. *Physical Review*, 159(1):98–103, 1967.
- [72] Hans C. Andersen. Molecular dynamics simulations at constant pressure and/or temperature. *The Journal of Chemical Physics*, 72(4):2384, 1980.
- [73] Vittorio Rosato, Maurice Guillope, and Bernard Legrand. Thermodynamical and structural properties of f.c.c. transition metals using a simple tight-binding model. *Philosophical Magazine A*, 59(2):321–336, 1989.
- [74] Fabrizio Cleri and Vittorio Rosato. Tight-binding potentials for transition metals and alloys. *Physical Review B*, 48(1):22–33, 1993.
- [75] Anna L. Gould, Andrew J. Logsdail, and C. Richard A. Catlow. Influence of Composition and Chemical Arrangement on the Kinetic Stability of 147-Atom Au-Ag Bimetallic Nanoclusters. *Journal of Physical Chemistry C*, 119(41):23685–23697, 2015.
- [76] Roy L. Johnston, Lauro Oliver Paz-Borbón, Giovanni Barcaro, and Alessandro Fortunelli. Structural motifs, mixing, and segregation effects in 38-atom binary clusters. *Journal of Chemical Physics*, 128(13):134517, 2008.
- [77] Davide Bochicchio and Riccardo Ferrando. Structure and thermal stability of AgCu chiral nanoparticles. *The European Physical Journal D*, 66(5):115, 2012.
- [78] Matthias Rupp, O. Anatole von Lilienfeld, and Kieron Burke. Guest Editorial: Special Topic on Data-Enabled Theoretical Chemistry. *The Journal of Chemical Physics*, 148(24):241401, 2018.
- [79] Claudio Zeni, Kevin Rossi, Aldo Glielmo, Ádám Fekete, Nicola Gaston, Francesca Baletto, and Alessandro De Vita. Building machine learning force fields for nanoclusters. *The Journal of Chemical Physics*, 148(24):241739, 2018.
- [80] Aldo Glielmo, Claudio Zeni, and Alessandro De Vita. Efficient non-parametric n-body force fields from machine learning. *Physics Review B*, 97:184307, 2018.
- [81] Wilfried Vervisch, Christine Mottet, and Jacek Goniakowski. Theoretical study of the atomic structure of Pd nanoclusters deposited on a MgO(100) surface. *Physical Review B*, 65(24):245411, 2002.
- [82] Ivalo Atanasov, Giovanni Barcaro, Fabio R. Negreiros, Alessandro Fortunelli, and Roy L. Johnston. Modelling the metal-on-top effect for pd clusters on the mgo(100) substrate. 2013.
- [83] Kevin Rossi, Luca Pavan, YeeYeen Soon, and Francesca Baletto. The effect of size and composition on structural transitions in monometallic nanoparticles. *The European Physical Journal B*, 91(2):33, 2018.

- [84] Krista Grace Steenberg and Nicola. Gaston. Two worlds collide: Image analysis methods for quantifying structural variation in cluster molecular dynamics. *Journal of Chemical Physics*, 140:064102, 2014.
- [85] Artem R Oganov and Mario Valle. How to quantify energy landscapes of solids. *The Journal of chemical physics*, 130(10):104504, 2009.
- [86] Gareth A Tribello, Jérôme Cuny, Hagai Eshet, and Michele Parrinello. Exploring the free energy surfaces of clusters using reconnaissance metadynamics. *The Journal of chemical physics*, 135(11):114109, 2011.
- [87] Jonathan Higham and Richard H. Henchman. Locally adaptive method to define coordination shell. *The Journal of Chemical Physics*, 145(8):084108, 2016.
- [88] Maurício J. Piotrowski, Paulo Piquini, and Juarez L. F. Da Silva. Density functional theory investigation of 3 d , 4 d , and 5 d 13-atom metal clusters. *Physical Review B*, 81(15):155446, 2010.
- [89] Florent Calvo. Solid-solution precursor to melting in onion-ring Pd–Pt nanoclusters: a case of second-order-like phase change? *Faraday Discussion*, 138(0):75–88, 2008.
- [90] Chadwick A. Tolman. Steric effects of phosphorus ligands in organometallic chemistry and homogeneous catalysis. *Chemical Reviews*, 77(3):313–348, jun 1977.
- [91] Nørskov, J.K. Rossmeisl, J. Logadottir, A. Lindqvist, L. Kitchin, T. J.R. Bligaard, and H. Jónsson. Origin of the overpotential for oxygen reduction at a fuel-cell cathode. *Journal of Physical Chemistry B*, 108(46):17886–17892, 2004.
- [92] Francesca Baletto, Christine Mottet, and Riccardo Ferrando. Freezing of silver nanodroplets. *Chemical Physics Letters*, 354(1-2):82–87, 2002.
- [93] Alessandro Laio and Michele Parrinello. Escaping free-energy minima. *Proceedings of the National Academy of Sciences of the United States of America*, 99(20):12562–6, 2002.
- [94] Alessandro Laio and Francesco L Gervasio. Metadynamics: a method to simulate rare events and reconstruct the free energy in biophysics, chemistry and material science. *Reports on Progress in Physics*, 71(12):126601, 2008.
- [95] James F. Dama, Michele Parrinello, and Gregory A. Voth. Well-Tempered Metadynamics Converges Asymptotically. *Physical Review Letters*, 112(24):240602, 2014.
- [96] Kevin Rossi and Francesca Baletto. The effect of chemical ordering and lattice mismatch on structural transitions in phase segregating nanoalloys. *Physical Chemistry Chemical Physics*, 19(18):11057–11063, 2017.
- [97] Luca Pavan, Kevin Rossi, and Francesca Baletto. Metallic nanoparticles meet metadynamics. *The Journal of Chemical Physics*, 143:184304, 2015.
- [98] John Skilling. Bayesian inference and maximum entropy methods in science and engineering. In *AIP Conference Proceedings*, volume 735, page 395, 2004.

- [99] Lívía B. Pártay, Albert P. Bartók, and Gábor Csányi. Efficient sampling of atomic configurational spaces. *Journal of Physical Chemistry B*, 114(32):10502–10512, 2010.
- [100] David J. Wales and Lindsey J. Munro. Changes of Morphology and Capping of Model Transition Metal Clusters. *Journal of Physical Chemistry*, 100(6):2053–2061, 1996.
- [101] Anna L. Gould, Kevin Rossi, C. Richard A. Catlow, Francesca Baletto, and Andrew J. Logsdail. Controlling Structural Transitions in AuAg Nanoparticles through Precise Compositional Design. *The Journal of Physical Chemistry Letters*, 7(21):4414–4419, 2016.
- [102] Edoardo Aprà, Francesca Baletto, Riccardo Ferrando, and Alessandro Fortunelli. Amorphization Mechanism of Icosahedral Metal Nanoclusters. *Physical Review Letters*, 93(6):65502, 2004.
- [103] Sung Youb Kim, In-Ho Lee, and Sukky Jun. Transition-pathway models of atomic diffusion on fcc metal surfaces. I. Flat surfaces. *Physical Review B*, 76(24):245407, 2007.
- [104] Yi Kang Lan, Chiu Hun Su, Wen Hsien Sun, and An Chung Su. Nucleation of decahedral Ag nanocrystals. *RSC Advances*, 4(27):13768, 2014.
- [105] Francesca Baletto and Riccardo Ferrando. Island adsorption and adatom diffusion on 3D non-crystalline silver nanoclusters. *Surface Science*, 490(3):361–375, 2001.
- [106] Tom Ellaby. *MSc Thesis*. King’s College Londond, 2014.
- [107] Hui Li, Peide D. Han, X. B. Zhang, and Ming Li. Size-dependent melting point of nanoparticles based on bond number calculation. *Materials Chemistry and Physics*, 137:1007–1011, 2013.
- [108] Georg Rollmann, Markus E. Gruner, Alfred Hucht, Ralf Meyer, Peter Entel, Murilo L. Tiago, and James R. Chelikowsky. Shellwise Mackay Transformation in Iron Nanoclusters. *Physical Review Letters*, 99(8):083402, 2007.
- [109] Kevin Rossi, Luca Pavan, YeeYeen Soon, and Francesca Baletto. The effect of size and composition on structural transitions in monometallic nanoparticles. *The European Physical Journal B*, 91(2):33, 2018.
- [110] Hongcheng Peng, Weihong Qi, Siqi Li, and Wenhai Ji. Modeling the phase stability of janus, core-shell, and alloyed ag-cu and ag-au nanoparticles. *J. Phys. Chem. C*, 119:2186, 2015.
- [111] William N. Lipscomb. Framework rearrangement in boranes and carboranes. *Science*, 153(3734):373–8, 1966.
- [112] Ivan Saika-Voivod, Louis Poon, and Richard K. Bowles. The role of fcc tetrahedral subunits in the phase behavior of medium sized Lennard-Jones clusters. *Journal of Chemical Physics*, 133(7):074503, 2010.
- [113] Cletus C. Asuquo and Richard K. Bowles. Molecular dynamics simulations of competitive freezing in gold nanoclusters. *Journal of Physical Chemistry C*, 116(27):14619–14626, 2012.

- [114] Kenji Koga. Novel Bidecahedral Morphology in Gold Nanoparticles Frozen from Liquid. *Physical Review Letters*, 96(11):115501, 2006.
- [115] Giulia Rossi and Riccardo Ferrando. Freezing of gold nanoclusters into poly-decahedral structures. *Nanotechnology*, 18(22):225706, 2007.
- [116] Hao Zhang, Pranav Kalvapalle, and Jack F Douglas. String-like collective atomic motion in the melting and freezing of nanoparticles. *The journal of physical chemistry. B*, 115(48):14068–76, 2011.
- [117] Hani A. Alarifi, Murat Atiş, Cem Özdoğan, Anming Hu, Mustafa Yavuz, and Norman Y. Zhou. Determination of complete melting and surface premelting points of silver nanoparticles by molecular dynamics simulation. *The Journal of Physical Chemistry C*, 117(23):12289–12298, 2013.
- [118] Royal Society of Chemistry. <http://www.rsc.org/periodic-table>. 2018.
- [119] Georgios Tritsarlis, Jeffrey Philip Greeley, Jan Rossmeisl, and Jens Kehlet Nørskov. Atomic-scale modeling of particle size effects for the oxygen reduction reaction of pt. *Catalysis Letters*, 141(7):909–913, 2011.
- [120] Alexandros Anastasopoulos, Jhonathan C. Davies, L. Hannah, Bryan E. Hayden, Cai E. Lee, Cleila Milhano, Claire Mormiche, and Laura Offin. The particle size dependence of the oxygen reduction reaction for carbon-supported platinum and palladium. *ChemSusChem*, 6:1973–1982, 2013.
- [121] Hui Liu, Feng Ye, Qiaofeng Yao, Hongbin Cao, Jianping Xie, Jim Yang Lee, and Jun Yang. Stellated Ag-Pt bimetallic nanoparticles: An effective platform for catalytic activity tuning. *Scientific Reports*, 4(1):3969, 2015.
- [122] Pablo M. Piaggi and Michele Parrinello. Entropy based fingerprint for local crystalline order. *The Journal of Chemical Physics*, 147(11):114112, 2017.
- [123] Gianpaolo Gobbo, Michael A. Bellucci, Gareth A. Tribello, Giovanni Ciccotti, and Bernhardt L. Trout. Nucleation of molecular crystals driven by relative information entropy. *Journal of Chemical Theory and Computation*, 14:959–972, 2018.

Appendix A

Building Machine Learning Force fields for nanoclusters

The following appendix section reports the publication of our work on the development of machine learning force-fields for nanoparticles. In particular, it discusses the transferability of a machine learning potential for nanoparticles generated from different training sets that encoded diverse degrees of structural heterogeneity. //

Because of copyright protection, the public version of this thesis does not contain the publication manuscript but suggests the interested reader to the online page where the article can be found:

<https://doi.org/10.1063/1.5024588>

Appendix B

PDF KL analysis robustness

This appendix section is dedicated to discuss the results observed for KL PDF analysis of melted and solid structures depending on the numerical parameters used towards its calculation.

KL PDF Analysis - reference cold structure choice The choice of the initial cold reference structure prior to the melting transition may affect the presence of a quasi first order transition in the $KL(h|c)$ vs temperature plot. In Figure B.1 we report the comparison between $KL(h|c)$ temperature evolutions for different choices of the reference cold structure, for the case of Pt nanoparticles of 201 atoms with an initial truncated octahedral morphology. Note the decrease in the values observed for $KL(h|c)$ when the cold reference is taken at higher temperatures and the absence of a quasi first order transition for the case of cold reference configurations taken after the melting.

KL PDF Analysis - PDF bin width choice The $KL(h|c)$ analysis is robust with respect to the choice of the distance bins by which the nanoparticle PDF is discretized, as long as the distance bin width is smaller than half of the distance between the first and second neighbours. In Figure B.2 we report the comparison between $KL(h|c)$ temperature evolutions for different choices of the bin width through which the pair distance distribution function of the nanoparticle is discretized. Data for a Pt nanoparticles of 201 atoms are reported. A distance bin width larger than 0.5\AA yields less easy to interpret and reliable results.

We further note that the $KL(h|c)$ calculus can lead to a divergence for a null occurrence of distances in a distance bin of the cold reference structure but not for the hot one. When comparing the PDF of an hot and a cold structure, a non-integer small ($0.01/N$ where N is the number of atoms, with other small value yielding similar results to the one presented here) occurrence is artificially accounted for in each distance bin which would be otherwise empty,

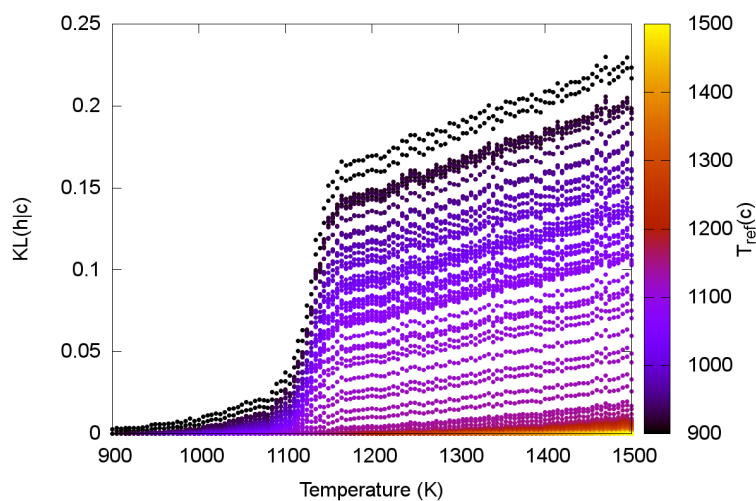


Figure B.1 Pt 201 nanoparticle $KL(h|c)$ temperature dependent evolution for the choice of different cold reference structures. When choosing cold structures after the melting point, no jump in the $KL(h|c)$ versus Temperature curve is observed.

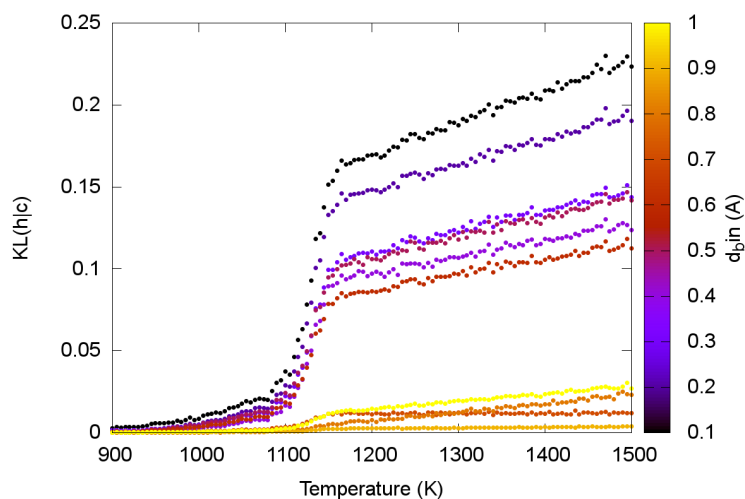


Figure B.2 Pt 201 nanoparticle $KL(h|c)$ temperature dependent evolution for the choice of 10 PDF binning width, from 0.1 Å to 1 Å. The choice of a distance bin larger than more than half of the distance between first and second nearest neighbours peaks yields a profile in the $KL(h|C)$ versus temperature plot not presenting a clear jump at the phase change. An increase in the bin width corresponds to a decrease in the $KL(h|c)$ values observed.

to avoid divisions by zero in $KL(h|c)$ calculus. This precaution is however not necessary if large enough distance bins are considered and/or the cold reference structure is taken at an high enough temperature, as for the case of the data here reported.

KL PDF Analysis - second neighbours versus full Preliminary results on the KL(h|c) robustness against the occurrence of structural rearrangements show that the choice of limiting the cross-entropy calculation to the 2nd nearest neighbours is beneficial, with KL(h|c) calculated for the full PDF being instead less resilient. Indeed the use of the KL(h|c) or other cross-entropy measures as a collective variable in enhanced sampling was earlier discussed in the case of the nucleation of molecular crystals by [122, 123], and our results suggest its likely positive application also to probe solid-solid transitions and solid-liquid phase changes in nanoparticles. Let us discuss the paradigmatic case of a Cu nanoparticle of 146 atoms with an initial Oh structure, undergoing a structural rearrangement towards an Ih morphology, Figure B.3 upper panel. In this figure we report in green the two different trends for the KL(h|c) if it is calculated for the full (left) pair distribution function of the nanoparticle, or up to the second nearest neighbour distance (right). In blue tones we report the evolution of three CNA signatures during each one of the eight independent simulations considered: (4,2,1) corresponding to pairs in a face centred cubic environment, (5,5,5) for atoms along a 5-fold symmetry, and (4,2,2) for the ones along a grain boundary.

At a temperature between 500 K and 600 K we observe a sharp increase in the number of (5,5,5) and (4,2,2) signatures, paralleled by a decrease in the number of atoms in fcc arrangement (i.e. (4,2,1) signature). This change in the CNA distribution corresponds to the structural rearrangement of the initially Octahedral nanoparticle, undergoing a solid-solid transition towards an Icosahedron. If the full PDF is taken in account during the KL(h|c) analysis a peak is observed preceding the full transition towards the icosahedron. This is not the case for the case of a KL(h|c) PDF analysis limited to the bulk lattice parameter. The melting transition is signalled by a second strong change in the CNA signatures, around 775 K. Indeed, the KL(h|c) PDF analysis limited to the bulk lattice parameter displays a sharp increase at this temperature.

For solid-solid rearrangements which are diffusion driven both KL(h|c) PDF analysis display a sharp increase only at the melting transition, as shown in figure B.3 bottom panel for the case of a Cu nanoparticle with an initial Oh morphology and with a size of 344 atoms. Here we observe a decrease, almost linear with temperature, of the (4,2,1) signature occurrence with temperature. Before the melting no five-fold symmetry axis or extended grain boundaries are however formed as witnessed by the almost null number of (5,5,5) and quite small occurrence of (4,2,2) signature. This structural characterization hence corroborates the visual observation of the transition from an Oh to a more To like structure by surface peeling.

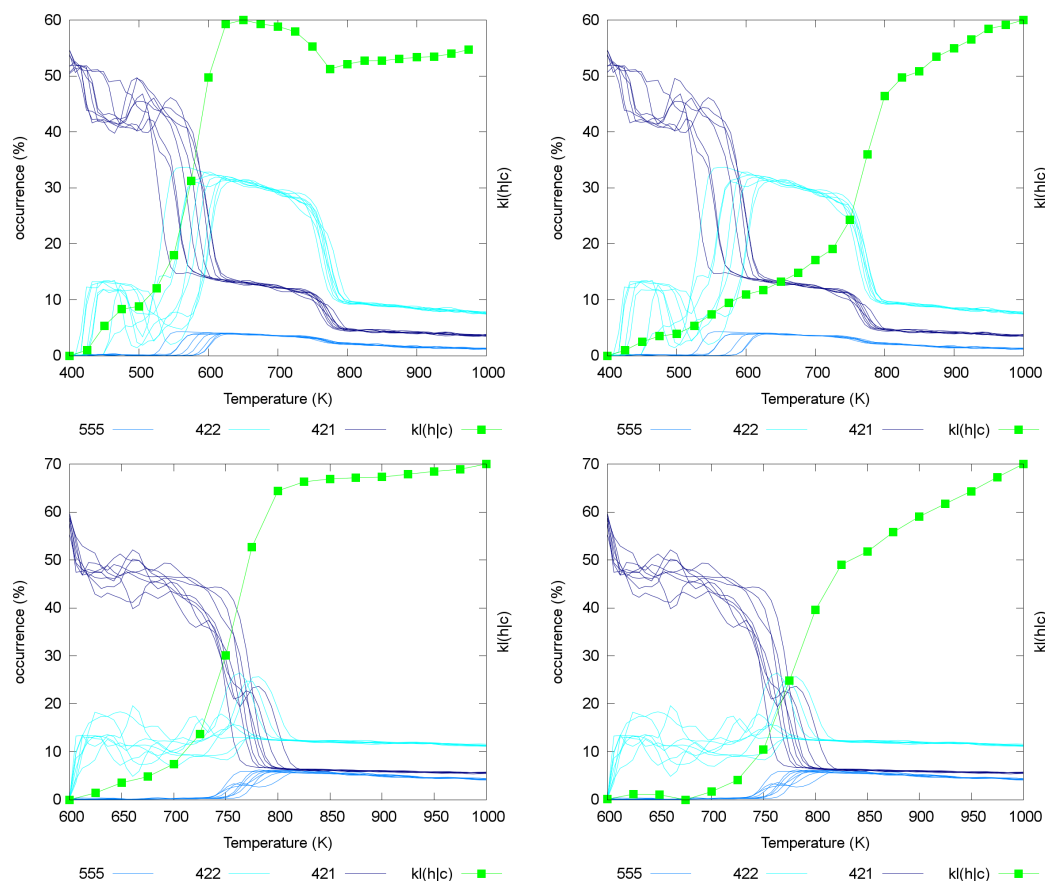


Figure B.3 The temperature evolution of the KL(h|c) of the whole (left) or limited to the bulk lattice parameter distance (right) PDF of a 146 (top) and 344 (bottom) atoms Cu nanoparticles with an initial Oh morphology is shown by green points linked by a line which acts a guide to the eye. CNA signatures relative occurrence is reported in shades of blue (navy = (5,5,5), blue = (4,2,2), cyan = (4,2,1)).